

·ALMA MATER STUDIORUM ·  
·UNIVERSITÀ DI BOLOGNA ·

---

---

SCHOOL OF ENGINEERING  
-Forlì Campus-

SECOND CYCLE MASTER'S DEGREE in  
AEROSPACE ENGINEERING  
Class LM-20

Graduation Thesis in:  
*Spacecraft Orbital Dynamics and Control*

**Radio Occultation experiments  
of Venus and Mars:  
similarities and differences**

Candidate:

*Edoardo Gramigna*

Supervisors:

*Prof. Marco Zannoni*

*Dr. Kamal Oudrhiri*

*Dr. Marzia Parisi*

*Dr. Dustin Buccino*

Examiner:

*Prof. Paolo Tortora*

Academic Year 2018/2019

# Acknowledgements

I want to thank my supervisor Professor *Marco Zannoni* and Professor *Paolo Tortora* for guiding me throughout these years, and for the opportunity they gave me to work on my Master's thesis at JPL.

Dr. *Kamal Oudrhiri*, Dr. *Marzia Parisi*, Dr. *Dustin Buccino* and all the Planetary Radar and Radio Sciences Group of Jet Propulsion Laboratory, for their support, their inspiration, and everything they taught me.

My parents *Lamberto*, *Daniela*, my sister *Annagiulia*, my grandparents and my whole family, for always believing in me, my friends *Virginia*, *Gabriele*, *Gioele* and *Luis*, who shared with me everything about this wonderful journey, *Maddalena* and all my friends.

# Abstract

In the last decades Venus has not been explored as in the early days of interplanetary missions, yet today the interest has increased and different space agencies are preparing proposals for future missions. Venus provides a laboratory next door to our planet to study how rocky planets can form and evolve differently from Earth, even when they start out very similar. Our neighboring planet is the perfect example of what happens in a runaway greenhouse effect, and the state of its atmosphere is interesting in its own right, as it is directly linked to the story of water on the planet and ultimately to the big question of whether life could have arisen beyond Earth. The main purpose of this thesis is the study of the atmosphere of Venus through the radio occultation experiments performed by the Venus Express Mission (VEX), sent by the European Space Agency in 2005. In the frame of this investigation comparisons between the Venus atmosphere and Mars atmosphere are shown, in order to highlight the similarities and differences between the two planets. The conclusions derived from this work can potentially improve our knowledge and highlight new scientific results about the Venus atmosphere.

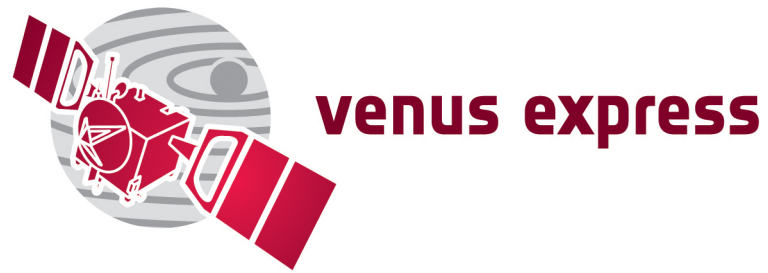


**Figure 1:** Venus Express mission logo. Credit: ESA



**Figure 2:** Mars Global Surveyor mission logo. Credit: NASA-JPL

# Contents

<b>List of Figures</b>	vi
<b>List of Tables</b>	xii
<b>Introduction</b>	xvii
<b>1 Venus and Mars</b>	1
<b>2 Venus Express mission</b>	7
2.1 Scientific objectives	8
2.2 Mission Operations	9
2.3 The spacecraft	14
2.4 The payload	15
2.5 Radio science experiments	18
2.5.1 Space segment	19
2.5.2 Ground segment	20
2.5.2.1 The Deep Space Network	21
<b>3 Radio Occultations</b>	25
3.1 Theoretical background	25
3.2 Observables	32
3.2.1 One-way range	32
3.2.2 One-way range rate	33
3.3 Signal Processing	34
3.3.1 Data information	35
3.3.2 Signal (time domain)	37
3.3.3 Fourier transform	38
3.3.4 Signal (frequency domain)	40

3.3.5	Predicted frequency residuals	44
3.3.6	Doppler effect	46
3.3.7	Reconstructed frequency residuals	50
3.4	Processing of radio occultation data	53
3.4.1	Frame of reference definition	54
3.4.2	Relativistic and non-relativistic equations for frequency residuals	56
3.4.3	Geometric definitions	57
3.4.4	Abel transform	60
3.4.5	Atmospheric parameters	61
3.4.6	Limitations	64
3.5	Noise characterization	65
3.5.1	Electronic instrumentation noise	65
3.5.2	Plasma noise	66
3.5.3	Earth's troposphere and ionosphere	68
<b>4</b>	<b>Venus and Mars atmosphere algorithm</b>	<b>73</b>
4.1	Algorithm's structure overview	74
4.2	Validation of the algorithm	78
4.2.1	MGS 8361M48A ingress occultation	78
4.2.2	VEX ESA DOY 234-2006 egress occultation	83
4.2.3	VEX ESA DOY 200-2006 ingress occultation	85
4.3	Integration time selection	87
4.4	Calibration of the reconstructed frequency residuals	90
4.4.1	Plasma noise	90
4.4.2	Earth's troposphere and ionosphere	90
4.4.3	Thermal noise, spacecraft clock and trajectory estimation	98
4.5	Relativistic vs non-relativistic solution	103
<b>5</b>	<b>Radio Occultation results</b>	<b>107</b>
5.1	Venus and Mars: Atmospheres comparison	107
5.2	Venus and Mars: temperature and pressure results	122
5.3	Venus scientific results	132
<b>6</b>	<b>Conclusions and Discussion</b>	<b>141</b>
	<b>Bibliography</b>	<b>144</b>

# List of Figures

1	Venus Express mission logo. Credit: ESA	iv
2	Mars Global Surveyour mission logo. Credit: NASA-JPL	iv
1.1	Venus - Earth - Mars. Credit: NASA	2
2.1	Artist concept of Venus Express. Credit: ESA	8
2.2	Interplanetary transfer orbit of Venus Express. Credit: European Space Agency (ESA)	10
2.3	Schematic of launch and transfer orbit. Credit: European Space Agency (ESA)	12
2.4	(a), (b) Artist's impressions of Venus Express journey to Venus. Credit: ESA	13
2.5	Venus Express spacecraft. Credit: ESA	15
2.6	Scientific Instruments carried by Venus Express. Credit: European Space Agency (ESA)	18
2.7	RF communications block diagram. Credit: European Space Agency (ESA)	20
2.8	NASA Deep Space Network Goldstone Complex, California. Credit: NASA	22
2.9	NASA Deep Space Network. Credit: NASA	23
3.1	Ray bending in the atmosphere. $r_0$ = ray path closest approach distance; $\alpha$ = deflection angle; $a$ = impact parameter; $n$ =index of refraction. [8]	26
3.2	Ingress (left) and Egress (right). In this case a star occulted by Venus is represented, but the geometry of the occultation is the same for the spacecrafts, too. Credits: <a href="https://www.skyandtelescope.com/observing/venus-occults-a-star/">https://www.skyandtelescope.com/observing/venus-occults-a-star/</a>	28

3.3	Grazing occultation of Aldebaran star by the Moon. As can be seen, the star (or spacecraft) never disappear, it travels slightly above (or under) the planet, so that the signal is always recordable, but weaker due to atmospheric losses. Credits: <a href="http://astroguyz.com/2017/03/31/astro-vid-of-the-week-an-amazing-grazing-occultation/">http://astroguyz.com/2017/03/31/astro-vid-of-the-week-an-amazing-grazing-occultation/</a> . . . . .	28
3.4	Ingress/egress typical processed signal of the occultation occurred the 17 <sup>th</sup> February 2014, recorded by JPL. <b>a)</b> Second past midnight (spm) vs residual frequency: in the middle region the residuals are high and the signal is dominated by noise because the spacecraft was occulted by Venus. <b>b)</b> spm vs Signal to Noise Ratio (SNR), in the middle the noise is dominant, so the SNR decreases. . . . .	29
3.5	Grazing processed signal of the occultation occurred the 19 <sup>th</sup> March 2014, recorded by JPL. <b>a)</b> Second past midnight (spm) vs residual frequency. <b>b)</b> spm vs SNR: note that with respect to the ingress/egress occultation (Figure 3.4a) the SNR does not decrease as in the previous case, because the spacecraft is not occulted by the planet. The decrease of the SNR is caused by the atmosphere of the planet. . . . .	31
3.6	Range definition and reference coordinate systems for the spacecraft and ground station. Credit: NASA . . . . .	34
3.7	Information about the occultation data 248V <sub>EOE</sub> 2014044 <sub>0325</sub> NNNX43RD.1B1 occurred on the 13 <sup>th</sup> February 2014. . . . .	35
3.8	Signal sampling representation. The continuous signal (green colored line) is replaced by the discrete samples (blue vertical lines). Credit: <a href="https://en.m.wikipedia.org">https://en.m.wikipedia.org</a> . . . . .	36
3.9	Outline of the Signal Processing. . . . .	36
3.10	Sine wave. Credit: <a href="https://www.investopedia.com/terms/s/sinewave.asp">https://www.investopedia.com/terms/s/sinewave.asp</a> . . . . .	37
3.11	Box function (time domain). Credit: <a href="http://www.thefouriertransform.com">http://www.thefouriertransform.com</a> . . . . .	38
3.12	Spectrum of the box function. Credit: <a href="http://www.thefouriertransform.com">http://www.thefouriertransform.com</a> . . . . .	39
3.13	Spectrogram of the VEX radio signal recorded by the DSN on the ingress/egress occultation of the 7 <sup>th</sup> March 2014. . . . .	41
3.14	Spectrum and main component frequency of the VEX radio signal at the xxxx of the 7 <sup>th</sup> March 2014. . . . .	41
3.15	Noise present in the signal when VEX was occulted by the planet. The FFT algorithm is not able to evaluate the main component frequency because there was no signal coming from the S/C, since it was occulted by Venus. . . . .	42

3.16 Signal to Noise Ratio (SNR) of the occultation of VEX on the 13th February 2014.	43
3.17 a) Predicted frequency residuals of the egress occultation of 13th February 2014. b) closer look on a).	45
3.18 Examples of Doppler effect. Credit: NASA Science	47
3.19 Examples of SPICE computations. Credit: NAIF, NASA-JPL	48
3.20 Kernels of SPICE. Credit: NAIF, NASA-JPL	49
3.21 Meta-kernel created to analyze the Venus Express data of JPL.	50
3.22 a) Reconstructed frequency residuals of the VEX egress occultation occurred the 13th of February 2014; b) closer look on the baseline.	52
3.23 Frame of reference adopted and geometry for a radio occultation experiment involving transmitter A, receiver B, and target P at the origin of the reference system.	54
3.24 SEP angle definition. [15]	69
3.25 Trend of the power spectral density of plasma noise and troposphere noise with respect to the SEP angle. [1]	69
3.26 Elevation angle. [15]	70
3.27 Earth's atmosphere layers. Credit: <a href="https://en.wikipedia.org/wiki/Ionosphere">https://en.wikipedia.org/wiki/Ionosphere</a>	71
4.1 MATLAB algorithm structure overview.	75
4.2 MGS 8361M48A Ingress occultation geometry.	79
4.3 Comparison of bending angles vs impact parameters between MATLAB algorithm (left) and Withers (2014) (right), for the MGS 8361M48A occultation.	80
4.4 Comparison of the electron density between MATLAB algorithm (left) and Withers (2014) (right), for the MGS 8361M48A occultation.	80
4.5 Comparison of the neutral number density between MATLAB algorithm (left) and Withers (2014) (right), for the MGS 8361M48A occultation.	81
4.6 Comparison of the refractivity between MATLAB algorithm (left) and Withers (2014) (right), for the MGS 8361M48A occultation.	81
4.7 Comparison of the pressure profile between MATLAB algorithm (left) and Withers (2014) (right), for the MGS 8361M48A occultation.	82
4.8 Comparison of the temperature profile between MATLAB algorithm (left) and Withers (2014) (right), for the MGS 8361M48A occultation.	82

4.9	Comparison of temperature profiles between MATLAB algorithm (left, with different boundary condition methods) and Pätzold (2007) result (right), for the VEX 234-2006 occultation.	83
4.10	Comparison of temperature profiles between MATLAB algorithm (left, with three different starting B.C) and Pätzold (2007) result (right), for the VEX 234-2006 occultation.	84
4.11	Temperature-pressure profile obtained for the VEX 234-2006 occultation.	84
4.12	Comparison of temperature profiles between MATLAB algorithm (left) and Pätzold (2007) (right) for the VEX DOY 200-2006 occultation <b>a)</b> Different B.C methods; <b>b)</b> Three different B.C, Tellmann [21] method.	86
4.13	Temperature-pressure profile obtained for the VEX DOY 200-2006 occultation.	87
4.14	<b>a)</b> Temperature profiles for different integration times ; <b>b)</b> closer look	89
4.15	Trend of the power spectral density of plasma noise and troposphere noise with respect to the SEP angle. [1]	91
4.16	Troposphere seasonal model for calibration.	93
4.17	Earth's troposphere dry seasonal constant term, which adjusts for the particular DSS used.	93
4.18	Earth's troposphere daily model.	93
4.19	Earth's troposphere daily model for calibration.	94
4.20	Earth's troposphere and ionosphere calibrations for one VEX-JPL occultation.	95
4.21	Earth's troposphere and ionosphere frequency shifts [Hz] for the VEX-JPL DOY 066 Ingress occultation.	97
4.22	Baseline of the VEX-JPL DOY 070-2014 Ingress occultation.	100
4.23	Baseline calibrated of VEX-JPL DOY 070-2014 Ingress occultation.	101
4.24	Baseline not calibrated of MGS DOY 015-2002 Ingress occultation.	102
4.25	Baseline calibrated of MGS DOY 015-2002 Ingress occultation.	102
4.26	<b>a)</b> Comparison of temperature profiles between relativistic solution (black line) and non-relativistic solution (red line) for Venus, from VEX JPL data. <b>b)</b> temperature difference between the two solutions.	104
4.27	<b>a)</b> Comparison of temperature profiles between relativistic solution (black line) and non-relativistic solution (red line) for Mars, from one MGS occultation. <b>b)</b> temperature difference between the two solutions.	105

5.1	Orbits of the two missions. <b>a)</b> Orbit of VEX around Venus, characterized by an apocenter altitude of 66000 km and pericenter altitude of 250 km;	
	<b>b)</b> Orbit of MGS around Mars with an apocenter altitude of 436.5 km and a pericenter altitude of 372.8 km. . . . .	108
5.2	Frequency residuals of the occultations. <b>a)</b> VEX Egress DOY 028 2014 ;	
	<b>b)</b> MGS Ingress DOY 361 1998. . . . .	110
5.3	Closer look of Figure 5.2 on the VEX ionosphere and its baseline. <b>a)</b> Ionosphere of VEX Egress DOY 028 2014 ; <b>b)</b> Baseline VEX Egress DOY 028 2014. . . . .	111
5.4	Baseline MGS Ingress DOY 361 1998. . . . .	112
5.5	Electron density profiles. <b>a)</b> VEX Egress DOY 028 2014; <b>b)</b> MGS DOY 361 1998. . . . .	114
5.6	Neutral number density profiles. <b>a)</b> VEX Egress DOY 028 2014; <b>b)</b> MGS DOY 361 1998. . . . .	115
5.7	Mass density of neutral atmosphere profiles. <b>a)</b> VEX Egress DOY 028 2014; <b>b)</b> MGS DOY 361 1998. . . . .	115
5.8	Refractivity profiles. <b>a)</b> VEX Egress DOY 028 2014; <b>b)</b> MGS DOY 361 1998. . . . .	116
5.9	Closer look on the refractivity profiles. <b>a)</b> VEX Egress DOY 028 2014; <b>b)</b> MGS DOY 361 1998. . . . .	117
5.10	Bending angle profiles. <b>a)</b> VEX Egress DOY 028 2014; <b>b)</b> MGS DOY 361 1998. . . . .	118
5.11	Temperature profiles . <b>a)</b> VEX Egress DOY 028 2014; <b>b)</b> MGS DOY 361 1998. . . . .	119
5.12	Pressure profiles. <b>a)</b> VEX Egress DOY 028 2014; <b>b)</b> MGS DOY 361 1998. . . . .	119
5.13	Spatial distribution of occultations data as a function of latitude and longitude. Points are related to the occultation point at 50 km and 25 km altitude for Venus and Mars, respectively. . . . .	125
5.14	Temperature profiles of the <b>MGS</b> occultations. . . . .	125
5.15	Pressure profiles of the <b>MGS</b> occultations. . . . .	126
5.16	Temperature-pressure profiles of the <b>MGS</b> occultations. . . . .	126
5.17	Temperature profiles for the <b>VEX</b> ingress occultations. . . . .	127
5.18	Pressure profiles of the <b>VEX</b> ingress occultations. . . . .	127
5.19	Temperature profiles of the <b>VEX</b> egress occultations. . . . .	128
5.20	Pressure profiles of the <b>VEX</b> egress occultations. . . . .	128
5.21	Closer look on Figure 5.20. . . . .	129

5.22 Temperature-pressure profiles of the <b>VEX</b> ingress occultations.	129
5.23 Temperature-pressure profiles of the <b>VEX</b> egress occultations.	130
5.24 Tropopause of Venus (example to detect it graphically).	133
5.25 Venus' tropopause temperature vs latitude.	134
5.26 Venus' tropopause altitude vs latitude.	134
5.27 Electron density vs altitude, latitude and local solar time (LST).	135
5.28 Variation of the 1 bar altitude with respect to: <b>a) Latitude ; b) Subsolar</b>	
<b>angle.</b>	136

# List of Tables

- 1.1 Venus, Mars, Earth fact sheet. Credit: NASA, ESA . . . . . 5
- 2.1 Venus, Mars, Earth fact sheet. Credit: NASA, ESA . . . . . 11
- 2.2 Venus, Mars, Earth fact sheet. Credit: NASA, ESA . . . . . 16
- 5.1 Venus & Mars algorithm's parameters. . . . . 122
- 5.2 Venus egress occultations, NASA-JPL data. . . . . 123
- 5.3 Venus Express ingress occultations 2014, NASA-JPL data. . . . . 124
- 5.4 Mars Global Surveyour occultations, NASA-JPL data. . . . . 124



# Introduction

Venus is one of the planets visible with the unaided eye so is impossible to say who discovered it first. Venus is the third brightest object in the sky, after the Sun and the Moon, so it is very likely that ancient peoples thousands of years ago knew about this planet. Since it is the planet with the closest approach to Earth, Venus has been the prime target in the early interplanetary exploration. In fact, it is the first planet visited by a robotic spacecraft (Mariner 2 from NASA in 1962), the first planet to be successfully landed on (Venera 7 from the Soviet Union in 1970) and the first planet beyond Earth to be photographed from its surface, made by the lander of Venera 9 mission of the Union Soviet in 1975. Between the 1960s and the 1980s intensive space mission campaigns have been carried out by the Soviet Union and the United States, which sent more than 30 spacecraft, all these missions with the same objective: studying the so-called “Earth’s sister”. In fact, Venus revealed similarities in size, density, mass, volume, orbital radius and bulk composition to Earth. However, the similarities ended here, due to the fact that these two planets had evolved in a very different way: Venus is characterized by extremely high temperatures, pressures, and an atmosphere composition which makes it uninhabitable. Coming back to the space missions, a great contributor in the understanding of the planet was made by the mission Magellan in the early 1990s from NASA, which mapped the gravity but also the entire surface of the planet [12]. Since then, Venus was largely a forgotten planet for more than a decade as the priority for investigations of the terrestrial planets shifted toward Mars. There were, however, still a large number of fundamental questions to be answered about the past, present and future of our neighboring planet. That is why in 2005, the European Space Agency sent a new mission, the Venus Express Mission (VEX). VEX’s primary objectives were to unveil the unsolved mysteries regarding its atmosphere, the plasma environment and its surface temperatures [20]. Before the mission ended in 2016, the VEX spacecraft sent back a large amount of new scientific data (around 2 Tbit) to Earth

from the onboard instruments and greatly increased the comprehension of the planet. After Venus Express, the Japanese Space Agency (JAXA), sent a new mission called Akatsuki to Venus, in order to continue the understanding of the planet and the mission is currently underway. Regarding future space exploration, Venus still represents one of the main targets, since there are still unanswered questions. Interesting proposals from NASA for future space missions at Venus are showing new interests focusing on in-situ missions, since the thick and dense atmosphere of Venus, as well as its temperatures in the middle atmosphere ( $\sim 75^{\circ}\text{C}$  at 50 km altitude), makes it a good environment for this kind of studies, which can enlighten more scientific properties of the planet.

The other Earth's neighbor is Mars. The Red Planet is the fourth planet from the Sun and the second smallest planet in the Solar System after Mercury. It is usually referred as the Red Planet, due to the effect of the iron oxide which characterize Mars' surface. This gives it a reddish appearance, which makes it unique among the astronomical bodies. The exploration on Mars started in October 1960, with the first Mars probes launched by the former Soviet Union. Unfortunately, both failed. The Americans made the first successful fly-by of Mars with Mariner 4 in July 1965. In particular Mariner 4 captured the first images of another planet ever returned from deep space. After this mission, dozens of robotic spacecrafts as orbiters, landers, and rovers have been sent to the Red Planet by the Soviet Union, United States, European Union and India, to study the planet's surface, climate and geology. Mars, in fact, has been explored more with respect to Venus. One of the reasons is that the Red Planet is characterized by a thin atmosphere, as well as temperatures and pressures which are not as high as on Venus, so that it has been explored more and in an easier way. In particular not only by orbiters, but by rovers too (which can survive only few minutes on Venus due to the extreme environment). The four rovers sent and landed successfully on Mars until now have been: Sojourner, Opportunity, Spirit and Curiosity. In the summer 2020 two more rovers will be launched to the Red Planet: Mars 2020 by NASA and ExoMars 2020 by the ESA-Roscosmos.

Regarding the history of the radio occultation experiments, the first theories have been presented to the scientific community between the 60's and 70's, in particular by Fjeldbo, Eshleman, Phinney, Anderson and Kliore [6]-[7]-[18]-[11]. Then, the first successful experiment has been the one made by the Mariner IV mission, which studied for the first time the atmosphere of another planet, Mars, through a radio occultation investigation. Previous knowledge of the atmospheric properties was poorly defined and

the vertical profiles have not been accessible to direct Earth-based measurement. After the first successful experiment this kind of studies have been used in several missions to study the atmosphere of other planets (Mariner missions, Cassini, VEX, New Horizons etc).

When the spacecraft is occulted by the planet, the radio signal between the spacecraft and the Earth is refracted (or bent) by the planet's atmosphere, causing a Doppler shift which is detected by the ground stations on Earth. From this Doppler shift is possible to obtain the refractivity index of the atmosphere as well as the vertical profiles of temperature, pressure, electron density and other science characteristics of the planet.

This research is focused on the study of the atmosphere of Venus and Mars through radio occultations experiments, in order to highlight similarities, differences and the challenges, both from the engineering and scientific point of view, in performing radio occultation experiments on these planets. In addition, one of the main goals of this work is to obtain new atmospheric results from JPL VEX data never studied before, in order to increase the comprehension and knowledge of Venus' atmosphere.

This work will cover all the steps needed to investigate radio science data, from the signal processing and its calibration, to the development of an Abel Transform algorithm, to the analysis of the vertical profiles of the atmosphere obtained. Regarding the radio science data analyzed within this research: for Venus, the radio occultations data are from the Venus Express mission of 2014, recorded at the Deep Space Network of NASA; regarding Mars, the radio science data are from Mars Global Surveyor (MGS) recorded at the DSN and managed by Jet Propulsion Laboratory.

To conclude, the work is organized as follows: Chapter 1 is dedicated to an overview of the two planets, Venus and Mars, and their atmospheres; Chapter 2 is focused on the Venus Express Mission; Chapter 3 introduces the theoretical background of the radio occultation experiments, the theory behind the Signal Processing and how it has been performed, as well as how to process the radio occultation data: all aspects needed in this research for the scientific comprehension and the engineering formulation of the problems; Chapter 4 shows the development of the atmosphere algorithms for Venus and Mars, its validation, and the differences and challenges due to the calibration of the data; Chapter 5 contains the results obtained for the atmosphere of Venus and Mars, in particular the temperature-pressure profiles will be showed and compared, as well as a Section will be dedicated to the new scientific results obtained for Venus; Chapter 6 is dedicated to conclusions and discussion.



# Chapter 1

## Venus and Mars

Venus is the second planet from the Sun and the closest Earth's planetary neighbor; from the mythological point of view Venus played a role in many ancient peoples and it owes its name to the Roman goddess of love and beauty. It is similar in structure and size to Earth but Venus spins slowly in the opposite direction from most planets. In addition, it is characterized by a thick atmosphere, which traps heat in a runaway greenhouse effect, making it the hottest planet in our solar system with surface temperatures hot enough to melt lead. From the radio occultation experiment point of view, its thick atmosphere makes the experiments extremely challenging, leading to a strong refraction of the radio signal which travels into it. Glimpses below the clouds reveal volcanoes and deformed mountains.

On the other side, Mars, which is the fourth planet from the Sun and owes its name to the Roman god of war. Mars is a dusty, cold and desert world characterized by a very thin atmosphere. The Red Planet is one of the most explored bodies in our solar system, thanks to its vicinity to Earth and its favorable conditions. Its thin atmosphere permits to perform in an easier way with respect to Venus the radio occultation experiments.

### Size and Distance

Venus has a radius of 6052 km and it has almost the same size as Earth. The distance with respect to the Sun is on average 108 million km (0.7 AU).

Mars has a radius of 3390 km and in terms of size, is about half of Earth. Its distance to the Sun is on average 228 million km (1.5 AU).



**Figure 1.1:** Venus - Earth - Mars. Credit: NASA

### **Formation**

Venus and Mars, as its fellow terrestrial planets, have a central core, a rocky mantle and a solid crust, and formed when gravity pulled gas and dust together about 4.5 billion years ago when the solar system settled in its current layout.

### **Orbit and Rotation**

The rotation and the orbit of Venus are unusual. Venus and Uranus are the only ones that rotate from east to west. One full rotation is equivalent to 243 Earth days — the longest day of any planet in our solar system, even longer than a whole year on Venus (225 days). In addition, the Sun doesn't rise and set each "day" on Venus like on most other planets. In fact, on Venus one day-night cycle takes 117 Earth days because Venus rotates in the direction opposite of its orbital revolution around the Sun. Its orbit around the Sun is the most circular of any planet (which are more elliptical or oval shaped). To conclude, Venus' axis of rotation is tilted of 3 degrees, and so the planet does not experience noticeable seasons.

Mars, on the other hand, completes one rotation every 24.6 hours. One year on Mars is made by 669.6 sols (Martian days are called sols) which is equivalent to 687 Earth days. Mars' axis of rotation is tilted 25 degrees, so it experiences seasons as Earth but longer and different in length due to its elliptical orbit around the Sun.

## Surface

Venus, as seen from space, is bright white because it is covered with clouds that reflect and scatter sunlight. On the other hand, an observer standing at Venus's surface would see rocks which are different shades of grey, like the ones on Earth, but the thick atmosphere filters the sunlight so that everything would look orange. Venus has mountains, valleys, and is plenty of volcanoes. The landscape is dusty, and surface temperatures reach 471 degrees Celsius. It is thought that Venus was completely resurfaced by volcanic activity 300 to 500 million years ago.

Mars at the surface is made by brown, gold and tan colors, with temperatures which can range between 20 degrees to -153 degrees Celsius. It appears reddish because of oxidization of the iron present in the rocks, the regolith and the dust. In particular, the dust raises up in the atmosphere, so that from distance makes the planet appear mostly red. Its surface is characterized by volcanoes, impact craters, and extremely big canyons. Mars surface seems to have had a watery past with rivers, deltas and lakebeds. In addition are present rock and minerals that could only have been generated in liquid water. Regarding the water, Mars' atmosphere is too thin to permit the existence of liquid water on surface. However, water on Mars as water-ice form is present under the surface in the polar regions.

## Atmosphere

Venus' atmosphere consists mainly of carbon dioxide, with clouds of sulfuric acid droplets. This thick atmosphere traps the Sun's heat, which is the reason why the surface temperatures are so high. The atmosphere has many layers, each one characterized by different temperatures. A similar Earth's surface temperature can be found about 48km up from Venus' surface. This is the region where future in-situ missions are planning to set permanent laboratories to study better Venus. The dense atmosphere and the good temperature and pressure at these altitudes, are the best environment for airships, which can increase the knowledge of this planet and its science. Venus is also characterized by extremely fast top-level clouds, driven by hurricane-force winds traveling at about 360 kilometers per hour. Speeds within the clouds decrease with cloud height, and at the surface are estimated to be just a few km per hour. On the ground, the atmosphere is so heavy it would feel like 1.6 kilometers deep underwater.

Mars is characterized by a thin atmosphere, mainly made by carbon dioxide, nitrogen and argon gases, which cannot protect the planet from meteorites, asteroids and comets impacts. In addition, the atmosphere is so thin that the heat from the Sun easily escapes the planet. Radio occultation experiments performed on Mars are easier with respect to Venus due to the Venus' thick atmosphere which has a stronger refraction and bending on the radio signal sent by the spacecraft.

### **Life**

No human has visited Venus and the spacecraft that have been sent to the surface of Venus did not last very long. Venus' high surface temperatures overheat electronics in spacecraft in a short time, so it seems unlikely that a person could survive for long on the Venusian surface. The only habitable region it seems to be the one at 50km altitude, characterized by pressure and temperatures not far from the one on Earth.

Regarding Mars, the scientists are not expecting to find living beings but they are looking for signs of life that existed long time ago, when the planet was covered with water, warmer and with a thicker atmosphere, which is one of the main scientific objectives of the *Mars2020* NASA mission.

### **Magnetosphere**

Venus' magnetic field is much weaker than the Earth's due to Venus' slow rotation, while Mars has no global magnetic field.

### **Moons and rings**

To conclude these main aspects, Venus has no moons, neither rings. Mars has two small moons, Phobos and Deimos but no rings.

Information credit: (<https://solarsystem.nasa.gov/planets/venus/in-depth/>).

Parameter	Venus	Mars	Earth
Average Orbit Distance (km)	108,209,475	227,943,824	149,598,262
Mean orbit velocity (km/s)	35.02	24.07	29.78
Equatorial radius (km)	6,051.8	3,389.5	6,371.00
Equatorial circumference (km)	38,024.6	21,296.9	40,030.2
Volume ( $km^3$ )	928,415,345,893	163,115,609,799	1,083,206,916,846
Mass (kg)	$4.869 \times 10^{24}$	$6.417 \times 10^{24}$	$5.972 \times 10^{24}$
Density ( $g/cm^{-3}$ )	5.24	3.934	5.52
Day duration	243 Earth days	24h 37m	23h 56m
Year duration	224.7 Earth days	687 Earth days	365.25 days
Atmosphere	96% $CO_2$ 3.5% $N_2$	95.32% $CO_2$ 2.7% $N_2$ 1.6% Ar	78% $N_2$ 21% $O_2$
Escape Velocity (km/s)	10.36	5.03	11.19
Surface Gravity ( $m/s^{-2}$ )	8.87	3.71	9.81
Axial Tilt (deg)	177.36	25.2	23.4393
Orbit Inclination (deg)	3.39	1.850	0.00
Eccentricity of orbit	0.00677672	0.093394	0.01671123

**Table 1.1:** Venus, Mars, Earth fact sheet. Credit: NASA, ESA



## Chapter 2

# Venus Express mission

Venus Express was the first Venus space exploration mission of the European Space Agency (ESA), which between different mission proposal choose the one of the group led by Dr. D. Titov [22]. Launched on the 9th November 2005 from the Baikonur Cosmodrom, Kazakhstan, it arrived at Venus in April 2006 with the main objective of long-term studies of Venus atmosphere. There were still a large number of fundamental questions to be answered about the past, present and future of Venus, and in addition, it was clear that an improved knowledge of Venus was essential to understand the general evolution of the terrestrial planets in the Solar System. It was with this in mind that ESA and the European scientific community decided to proceed with this new space mission. The mission was proposed in 2001 to reuse the design of the Mars Express mission, with some modifications needed to survive at the extreme thermal environment around Venus, leading to a very cost-effective mission in a very short time [20]. Furthermore, the real innovation with respect to previous missions was a long time period observation, together with a near-polar orbit which was specifically chosen to ensure the maximum scientific return, in particular to study the atmospheric dynamics. Many of the spacecraft's observations have focused on the structure, dynamics, composition and chemistry of the dense atmosphere and the overlying clouds, but also fascinating and new discoveries have been made, as for example the swirling vortex at the planet's South Pole, a surprisingly cold region in the high planet's atmosphere, as well as a high altitude ozone layer and a mysterious layer of sulfur dioxide far above the main cloud layer. In addition, this was the first time that ESA conducted an aerobraking campaign to gain experience for future missions. To

conclude this overview on the mission, thanks to the VEX data, scientists are moving closer toward understanding this enigmatic world, however lot of mysteries are still there. The Akatsuki spacecraft, from JAXA, is currently studying Venus but different space agencies, as NASA for example, which last Venus space mission was Magellan in 1990, are planning to come back to Venus in the near future.

This chapter will give an overview of the scientific objectives of VEX, its mission operations, the spacecraft, the payload, and the planet Venus, with a particular attention on the description of the onboard radio science experiments.



**Figure 2.1:** Artist concept of Venus Express. Credit: ESA

## 2.1 Scientific objectives

The aim of the Venus Express mission was to carry out a comprehensive study of the atmosphere of Venus and to study the planet's plasma environment and its interaction with the solar wind in some detail. In addition, dedicated surface studies were also performed. The scientific objectives of the Venus Express mission have been concisely expressed within seven scientific themes, which are [20]:

- Atmospheric structure;
- Atmospheric dynamics;
- Atmospheric composition and chemistry;

- Cloud layer and hazes;
- Energy balance and greenhouse effect;
- Plasma environment and escape processes;
- Surface properties and geology.

In particular, the first three themes are divided into sub-themes, which refer to the upper (110 km), middle (60 km) and lower parts of the atmosphere (below 60 km).

## 2.2 Mission Operations

Venus Express was launched by a Soyuz-Fregat launcher from the Baikonur Cosmodrome, Kazakhstan, at 03:33:34 UT on 9 November 2005. First of all, the Soyuz rocket placed the Fregat/spacecraft combination in a suborbital trajectory. Then, a first burn of the Fregat moved the combination into a Low Earth Orbit and, after one orbit around the Earth, the Fregat was fired again, placing the combination in a heliocentric orbit for its interplanetary trajectory. Furthermore, immediately after the second burn, the spacecraft separated from the Fregat and the first automatic activities were carried out, as for example establishing of radio contact with the ground stations, acquisition of the sun-pointing attitude, deployment of the solar arrays. This, followed by commanded activities to prepare the spacecraft for the near-Earth commissioning phase (NECP). The operations described above are also called Launch and early orbit phase (LEOP). The next phase was called NECP, which started after the LEOP, and was dedicated to activate and verify the subsystems as well as the payload. Then, after finishing the NECP, the spacecraft was started its interplanetary cruise phase (about 150 days), as can be seen with more details in Figure [2.2](#), which ended before the Venus Orbit Insertion (VOI).

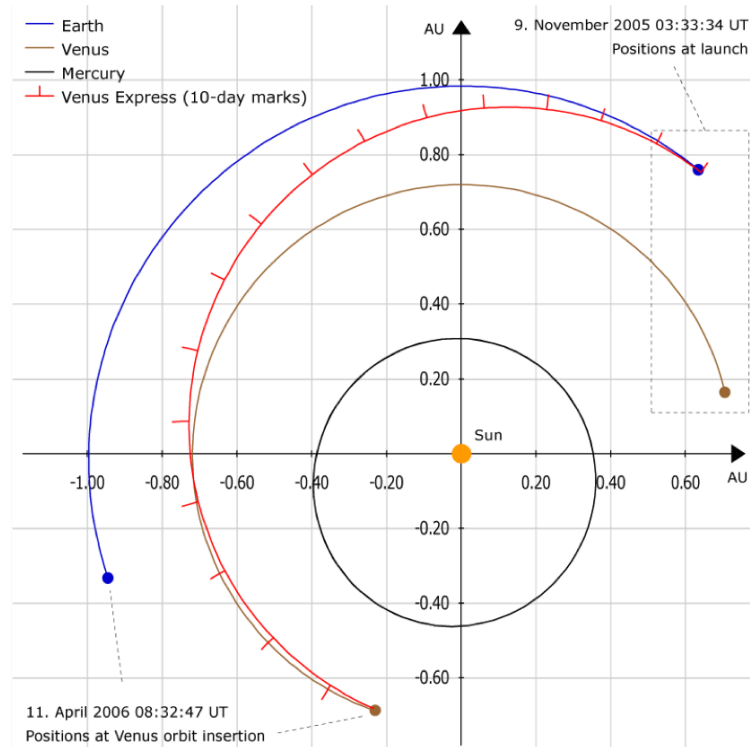


**Figure 2.2:** Interplanetary transfer orbit of Venus Express.  
Credit: ESA

In this cruise the spacecraft was kept in a three-axes stabilized attitude with the solar arrays facing the Sun and the high gain antenna pointing to the Earth, for daily health checks and navigation. Then, finally, there was the orbit insertion, which started one month before the Venus orbit capture manoeuvre. and ended as soon as the spacecraft reached its operational orbit around Venus. After completing several commanded actions, in order to capture the final orbit, Venus Express started its nominal mission on 4 June 2006. Furthermore, the operational orbit was mainly composed by two activities: the first one with the orbital time (OT, time counted from each pericenter pass) between 2 and 11h for the telecommunications with the Earth; the second one, characterized by the 15h remaining, was used for science operations [20]. The selected orbit was inertially fixed, so that was able to cover all the planetocentric longitudes in one Venus sidereal day (equivalent to 243 Earth days). Regarding the mission lifetime, initially was set for two Venus sidereal days but several mission extensions have pushed back the mission end date to 16 December 2014 (ten Venus sidereal days) when the mission control

lost contact with Venus Express, likely due to exhaustion of propellant. In order to achieve the science goals, a high inclination elliptical orbit was selected, which provided complete latitudinal coverage and gave the best compromise for allowing high-resolution observations near pericenter, global observations at apocenter, and measurements of the Venusian plasma environment and its interaction with the solar wind. In the Table [2.2](#) are reported the parameters of the operational orbit, while in the Figure [2.3](#) can be seen a summary of the mission operations performed by VEX.

<b>Orbital Parameter</b>	<b>Nominal value</b>
Pericenter altitude (km)	250
Apocenter altitude (km)	66000
Period (h)	24
Inclination (deg)	$\sim 90$
Pericenter latitude (deg)	80

**Table 2.1:** Venus, Mars, Earth fact sheet. Credit: NASA, ESA

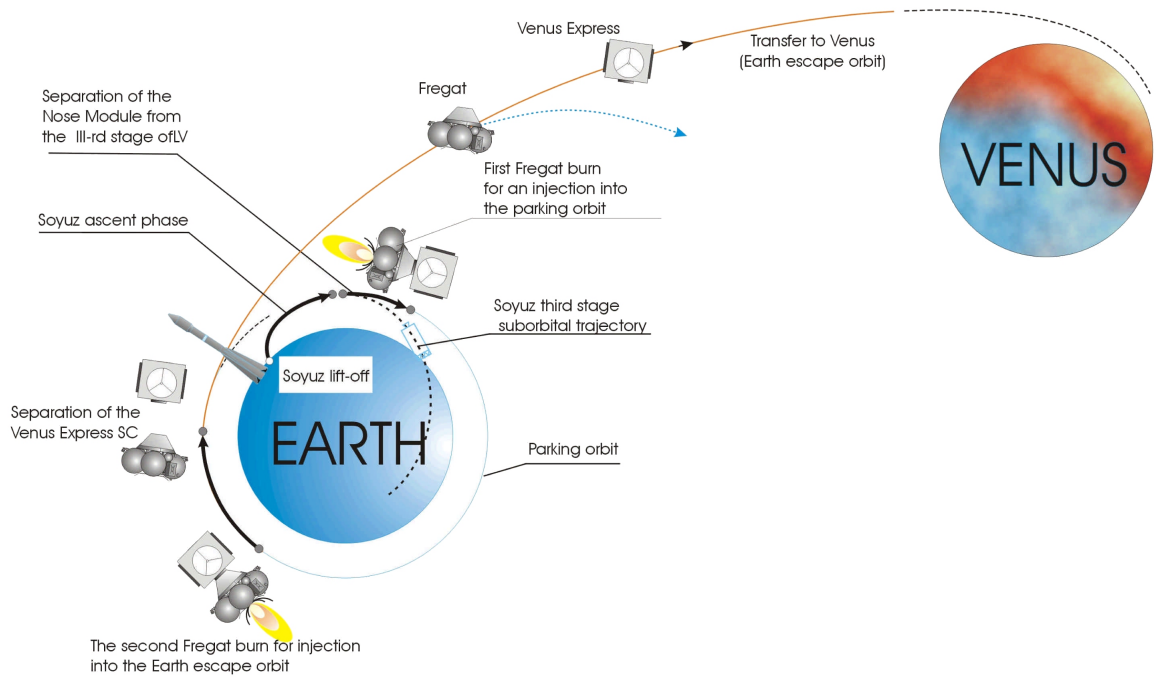
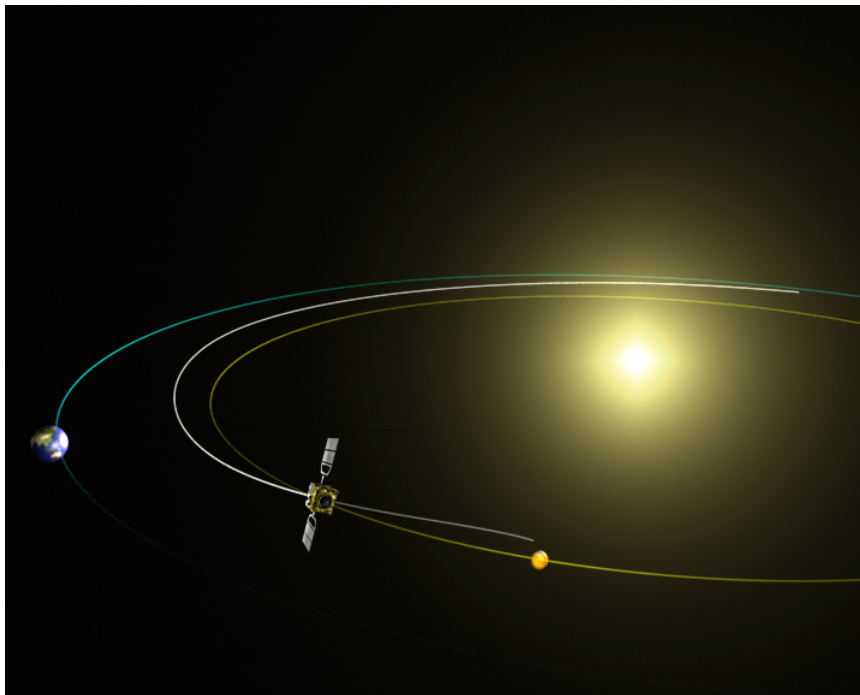
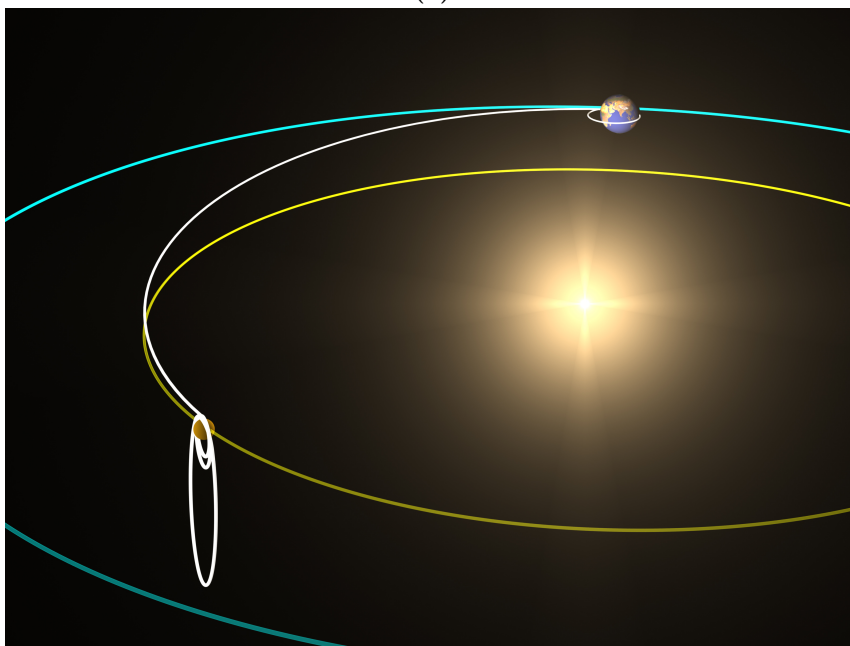


**Figure 2.3:** Schematic of launch and transfer orbit.  
Credit: ESA

To conclude this section, the Venus Express ground segment used a system of ground stations and a communication network that performed telecommand up-link, telemetry acquisition, and spacecraft tracking operations at S- and X-band frequencies, and coordinated from the Venus Express Mission Operations Center at ESOC. The main ground station for telecommunications with the spacecraft was the ESA 35m antenna in Cebreros, Spain. In addition, others have been used, as the ESA antenna in New Norcia, the Kourou 15m station and the NASA Deep Space Network.



(a)



(b)

**Figure 2.4:** (a), (b) Artist's impressions of Venus Express journey to Venus.  
Credit: ESA

## 2.3 The spacecraft

Venus Express was based on the Mars Express spacecraft design and so, a very cost-effective and reduced risk mission has been realized in short time. Obviously, the design was characterized by some modifications, mainly needed to cope with the thermal environment around Venus (the solar flux at Venus is four times higher compared to Mars), and consequently the need to accommodate the modified set of instruments [20]. Venus Express is a 1.7x1.7x1.5m, 1200 kg 3-axis stabilized spacecraft (see Figure 2.5), mainly composed by the following systems [20]:

### Communication

Includes a transponder which transmitted and received in both S- and X-band, and four different antennas: Two low gain antennas (LGA) (S-band only), one dual band 1.3m diameter high gain antenna (HGA1), and one 0.3m diameter single band offset antenna (HGA2) (X-band only).

### Propulsion

Single 400N main engine for orbit capture and eight small 10N thrusters for attitude control and orbit maintenance manoeuvres. Total fuel load = 570kg (higher than for Mars Express due to a higher  $\Delta v$  requirement).

### ADCS

The reaction wheels, provided flexibility and accuracy, and were used for almost all attitude manoeuvres. The wheels off-loading (to remove the accumulated angular momentum) was performed by using firing thrusters. In addition, were installed star trackers, gyros and a sun sensor.

### Electrical

Electricity was generated by two symmetrical solar array wings of two panels each, equipped with triple junction Gallium Arsenide cells, with a total area of  $5.7m^2$ . In the vicinity of the Earth the solar arrays were sized to generate at

least 800W, which resulted in 1400W at Venus. During eclipse or when spacecraft power demand exceeded solar array capacity, power was supplied by three 24 Ah lithium-ion batteries.

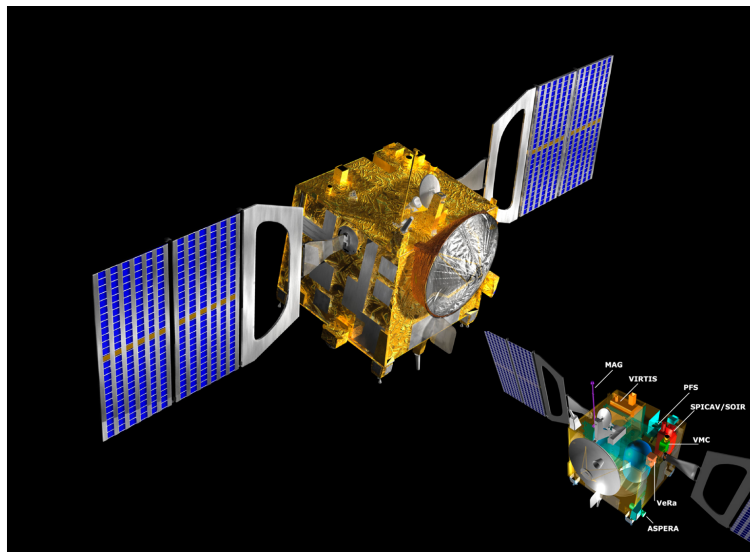


**Figure 2.5:** Venus Express spacecraft. Credit: ESA

## 2.4 The payload

The payload was characterized by a combination of spectrometers, spectro-imagers and imagers working on a wavelength range from ultraviolet to thermal infrared, a magnetometer and a plasma analyzer, see Table 1.2. Thanks to these instruments, VEX was able to study the atmosphere, plasma environment and surface of Venus in great detail. As explained before, most of the instruments are re-using designs from either Mars Express or Rosetta missions, see Figure [2.6](#).

<b>Instrument</b>	<b>Objective</b>	<b>Heritage</b>
ASPERA-4	Neutral and ionised plasma analysis	Mars Express (ASPERA-3)
MAG	Magnetic field measurements	Rosetta Lander (ROMAP)
PFS	Atmospheric vertical sounding by infrared Fourier spectroscopy	Mars Express (SPICAM)
VeRa	Radio sounding of atmosphere	Rosetta (RSI)
VIRTIS	Spectrographic mapping of atmosphere and surface	Rosetta (VIRTIS)
VMC	Ultraviolet and visible imaging	Mars Express (HRSC/SRC) Rosetta (OSIRIS))

**Table 2.2:** Venus, Mars, Earth fact sheet. Credit: NASA, ESA

This work is based on the analysis of the experiments and the data from VeRa instrument (see Figure 2.6), so an overview of the scientific objectives and its characteristics is provided below.

Science objectives [8]:

- Determination of neutral atmospheric structure from the cloud deck (approximately 40km altitude) to 100km altitude from vertical profiles of neutral mass density, temperature, and pressure as a function of local time and season. Within the atmospheric structure, search for, and if detected, study of the vertical structure of localized buoyancy waves, and the presence and properties of planetary waves;
- Study of the H<sub>2</sub>SO<sub>4</sub> vapor absorbing layer in the atmosphere by variations in signal intensity and application of this information to tracing atmospheric motions. Scintillation effects caused by radio wave diffraction within the

atmosphere can also provide information on small-scale atmospheric turbulence;

- Investigation of ionospheric structure from approximately 80km to the ionopause (around 600 km), allowing study of the interaction between solar wind plasma and the Venus atmosphere;
- Observation of forward-scattered surface echoes obliquely reflected from selected high-elevation targets with anomalous radar properties (such as Maxwell Montes). More generally, such bistatic radar measurements provide information on the roughness and density of the surface material on scales of centimeters to meters;
- Detection of gravity anomalies, thereby providing insight into the properties of the Venus crust and lithosphere;
- Measurement of the Doppler shift, propagation time, and frequency fluctuations along the interplanetary ray path, especially during periods of superior conjunction, thus enabling investigation of dynamical processes in the solar corona.

In order to achieve these objectives, VeRa worked together with the radio links of the spacecraft communication systems at wavelengths of 3.6 and 13 cm (“X” and “S” -band, respectively). In addition, an Ultra Stable Oscillator (USO) provided a high-quality onboard reference frequency source, a system never used in the previous Venus mission. This simultaneous and coherent dual-frequency downlink, via the High Gain Antenna, was required to separate the effects of the classical Doppler shift due to the motion of the spacecraft relative to the Earth and the effects caused by the propagation of the signals through the various dispersive media in the signal path. From the general point of view, the radio science experiments rely on the observation of the phase, amplitude, polarization and propagation times of radio signals transmitted from the spacecraft and received by ground stations on Earth. In fact, the radio signals are affected by the medium through which the signals propagate (atmospheres, ionospheres, interplanetary medium, solar corona), by the gravitational influence of the planet on the spacecraft as well as the performance of the various systems involved both on the spacecraft and on ground.

Among the different science objectives, this work is focused on the Radio sounding of atmosphere and ionosphere. Basically, the sounding of the neutral and ionized atmosphere is performed just before the spacecraft enters occultation by the planet. The High Gain Antenna is pointed toward the Earth before the approach to occultation so that the radio link passes through a vertical swath of the ionosphere and atmosphere. Then, the instrument on Earth record amplitude, phase, propagation time, and polarization of the received signals, which are then analyzed and converted in vertical profiles of Venus' atmosphere and ionosphere. More information on how a radio science experiment works is given in the next section.

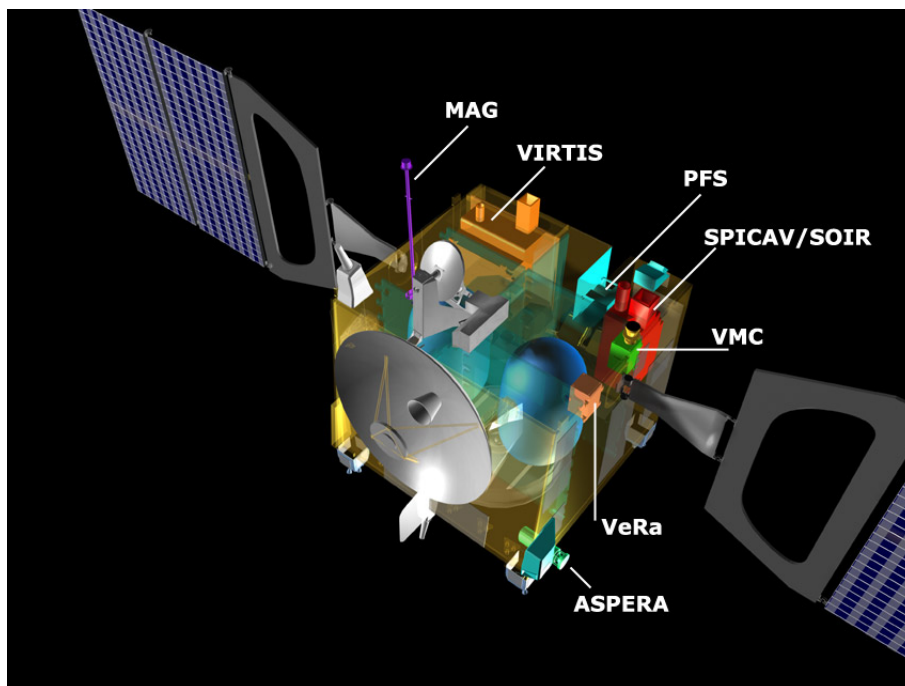


**Figure 2.6:** Scientific Instruments carried by Venus Express.  
Credit: ESA

## 2.5 Radio science experiments

The Radio science experiments take advantage of the radio-frequency link between the spacecraft (space segment) and the stations on the Earth (ground segment), in order to study the physical and scientific critical characteristics of a heavenly body.

Usually, these experiments are carried out in order to determine the gravity field, the atmosphere and the surface of a planetary body. Regarding this work, the study of the Venus' atmosphere required first of all an understanding of the systems, the data and processing methods, from which radiometric observations can be obtained and, in the end, would lead to crucial science results. This section will provide details about the space segment, ground segment and the radio-frequency link used in the Venus Express mission.

### 2.5.1 Space segment

In the radio occultations experiments, usually, the link between the space segment and the ground segment is a one-way link.

Here the two different communication methods are explained:

- One-way link: the data flows from sender to receiver only, thus providing no feedback;
- Two-way link: both parties involved transmit information, usually the ground stations sends a link to the spacecraft which lock into that carrier, multiply the frequency received for a known value (turnaround ratio) and sends back information, guaranteeing a more stable frequency reference.

When considering a radio occultation experiment, in a two-way link the signal sent by the spacecraft passes through the atmosphere two times in two different regions, complicating a lot the data analysis, because it is difficult to disentangle the index of refraction of the uplink and downlink legs. In addition, especially for the egress occultations, the spacecraft's transponder would require more time to lock into the carrier sent by the ground station, leading to loss of crucial data from the ground station. These are the reason why the radio occultation experiments employ the one-way link. So, when considering the one-way link, the transmitted frequency of the spacecraft plays a key role in the whole experiment. In fact, the open-loop receivers adopted by the ground stations rely on frequency predicts to remain tuned to the incoming signal. To this end, the Venus Express Mission is the first one which adopted an Ultra Stable Oscillator at Venus.

In addition, the spacecraft has a Dual Band Transponder (DBT), and the frequencies for the downlink are approximately: 2296 MHz for S-Band and 8419 MHz for

X-Band. The advantage of having a DBT relies on the capability to completely cancel out the plasma noise and interplanetary medium, obtaining in this way better and more reliable measurements/results. Unfortunately, as it will be pointed out later in this work, the radio occultation data studied was single-frequency, so that the plasma noise cannot be canceled out but it has been taken into consideration in the analysis.

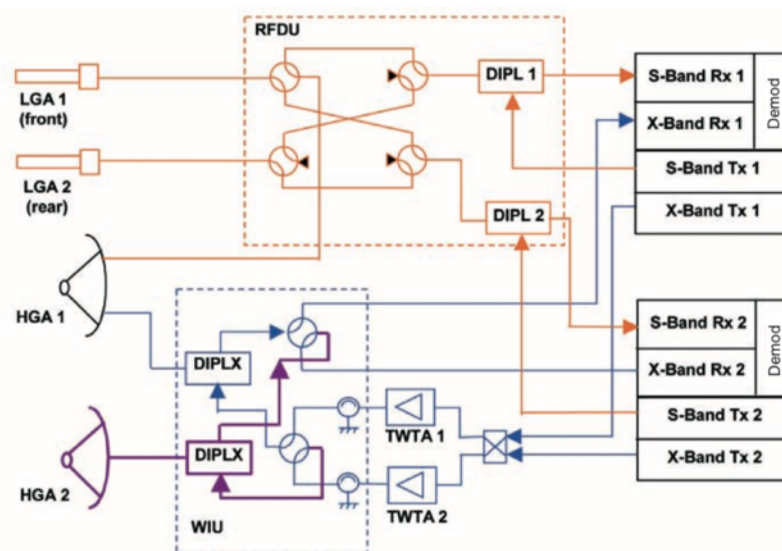


**Figure 2.7:** RF communications block diagram.  
Credit: ESA

### 2.5.2 Ground segment

The communications with the spacecraft have been performed through the ESA 35 m deep space ground station located in Cebreros, near Madrid in Spain (DSA2). The observations carried out with VeRa required additional support which came from the 35m New Norcia ground station (DSA1). In addition, during critical periods, also the NASA Deep Space Network (DSN) participated in the mission. In the frame of this work the data analyzed is the one received from the DSN.

### 2.5.2.1 The Deep Space Network

The DSN consists of three facilities spaced equidistant from each other – approximately 120 degrees apart in longitude – around the world. These sites are at Goldstone, near Barstow, California; near Madrid, Spain; and near Canberra, Australia. The strategic placement of these sites permits constant communication with spacecraft as our planet rotates – before a distant spacecraft sinks below the horizon at one DSN site, another site can pick up the signal and carry on communicating, see Figure [2.9](#). As well known, the Deep Space Network is fundamental for communicating with deep space missions, however this Network is also able to generate accurate radio science data observables. From the general point of view, the parabolic surface of the antenna focuses the radio-frequency energy, coming from the spacecraft, onto a subreflector, which is adjusted in position to optimize the transfer of energy to the other systems within the complex. Firstly, it is interesting in understanding the two methods to keep the antennas pointed at the spacecraft. The first method, is the closed loop “CONSCAN” where the acquired signal is conically scanned by the antenna. Then the feedback from the closed loop receiver provides information comparable to the scan pattern of the received signal, and compensates to point the scan center at the apparent direction of the spacecraft signal. However, in case of high signal dynamics or low received signal levels (what usually happens in occultation experiments) the CONSCAN cannot be used and the antenna is “blind pointed” by using predicted ephemeris from the spacecraft navigators which are transformed into antenna’s coordinates.

Even for the reception of the signal in the Deep Space Network there are two different methods: the first one, and not used in radio occultations experiments, is the closed-loop reception which provides, through the feedback, a rapid acquisition of the signal and the telemetry lockup. However, this method requires some time to lock-up the signal (especially during the egress of occultations when the signal from the spacecraft is lower) and could lead to loss of crucial data. That is the reason why the open-loop reception method is adopted for these experiments and so in this research, which have been conducted through data received in open-loop. The open-loop receivers rely on frequency predicts to remain tuned to the incoming signal. To conclude, the signal is downconverted from RF to IF and then from IF to VF which is in the end the type of data processed for the experiments [2](#).

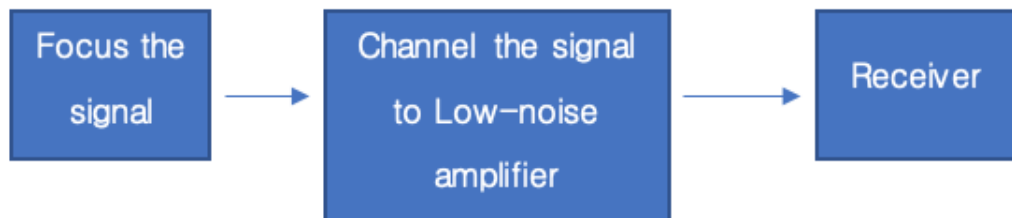


**Figure 2.8:** NASA Deep Space Network Goldstone Complex, California.  
Credit: NASA

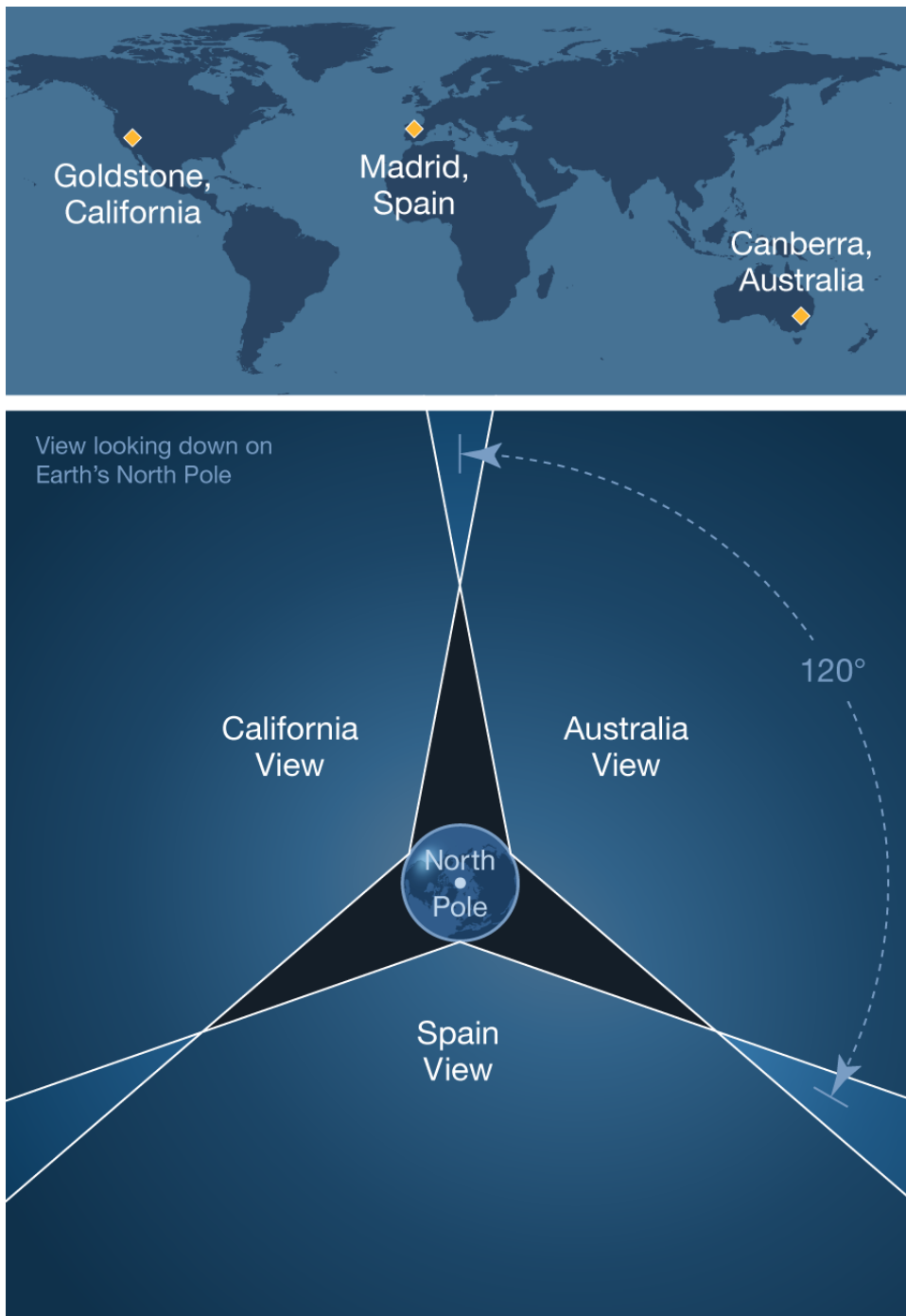


**Figure 2.9:** NASA Deep Space Network. Credit: NASA



## Chapter 3

# Radio Occultations

This chapter will give a description of the main theoretical topics needed, within the frame of this work, for conducting and studying radio science experiments, as well as the mathematical model and the understanding needed to describe the results obtained will be showed. In particular, Section [3.1](#) will cover a general background on the radio science experiments. Section [3.2](#) will be focused on the signal processing, with a description of how to obtain the reconstructed frequency residuals starting from the recorded radio signal in the time domain. To conclude, Section [3.3](#) will go into the details of the mathematical model employed in radio science investigations, to convert the reconstructed frequency residuals into the relevant atmospheric parameters of the target.

### 3.1 Theoretical background

The Radio occultation investigations are remote sensing techniques, which employ a radio signal between a transmitter and a receiver to measure physical properties of a target, as a planetary body. These have been commonplace on planetary science flyby and orbital missions since Mariner 4 reached Mars in 1965 [\[11\]](#), with dozens of spacecrafts performing radio occultations at many planets, satellites, and a comet [\[23\]](#). The first studies and theories, as well as the mathematical models needed for these radio science investigations, dates back in the 60's ( the first radio occultation experiment was done by Mariner IV on the 15th July 1965) when Phinney [\[18\]](#) and Eshleman [\[5\]](#) presented the first studies. Then, lot of research have been done on these theories from Eshleman, Fjeldbo, Kliore, Anderson, Phinney

etc. From the general point of view, the atmospheric radio occultation investigations, which are the focus of this work, rely on the detection of a change in a radio signal as it passes through the atmosphere of a solar system object. This is due to the fact that when an electromagnetic radiation passes through the atmosphere, it is refracted, as can be seen from Figure 3.1 .

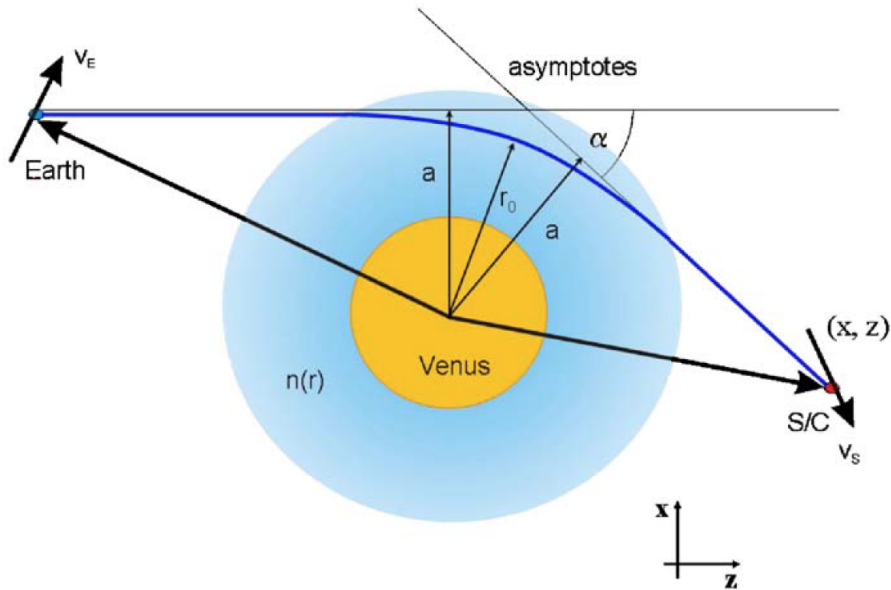


**Figure 3.1:** Ray bending in the atmosphere.  $r_0$  = ray path closest approach distance;  $\alpha$  = deflection angle;  $a$  = impact parameter;  $n$ =index of refraction. [8]

The refraction of the radio signal in the neutral gas and ionospheric plasma around the target object modifies the frequency of the radio signal, which is, in the end, different with respect to what expected by the receiver if no occultation would have occurred. In this way is possible to evaluate the frequency residuals, which represent the difference between the modified frequency during occultation, and the expected direct frequency without refraction and occultation. By analyzing and processing the frequency residuals during a radio occultation investigation, the physical properties of the target object can be obtained. For example, vertical profiles of the electron density of ionospheric plasma, number density of neutral gas, pressure, temperature and mass density of the planetary body can be obtained, starting from the frequency residuals defined before. To do so, a detailed

knowledge of the positions and velocities of the transmitter, receiver and target, as a function of time, is required for the success of the radio occultation investigation. Furthermore, since these positions and velocities are related to times, the knowledge and accuracy of the time evaluation is crucial for the success of the experiments, as well.

From the geometrical point of view, an occultation experiment can be classified as:

- Ingress / egress occultation;
- Grazing occultation.

The ingress/egress experiment is the most common to analyze, easier with respect to the grazing, and is made by two different and separate phases, see Figure [3.2](#). The ingress phase happens when the spacecraft is getting close to the planet, then its signal starts traveling through the planet's atmosphere so that it is refracted. The spacecraft then disappears behind the planet as seen by the ground station, which is not able to receive the signal anymore. On the other hand, the egress phase is defined when the spacecraft reappear from behind the planet, so that the ground station is able to receive its signal, again. Here another refraction takes place as the spacecraft's signal pass through the planet's atmosphere. In the end, in each phase is possible to obtain scientific data getting the atmospheric properties of the target. A plot of the typical signal recorded by the ground station during an ingress/egress occultation experiment is reported in Figure [3.4a](#).

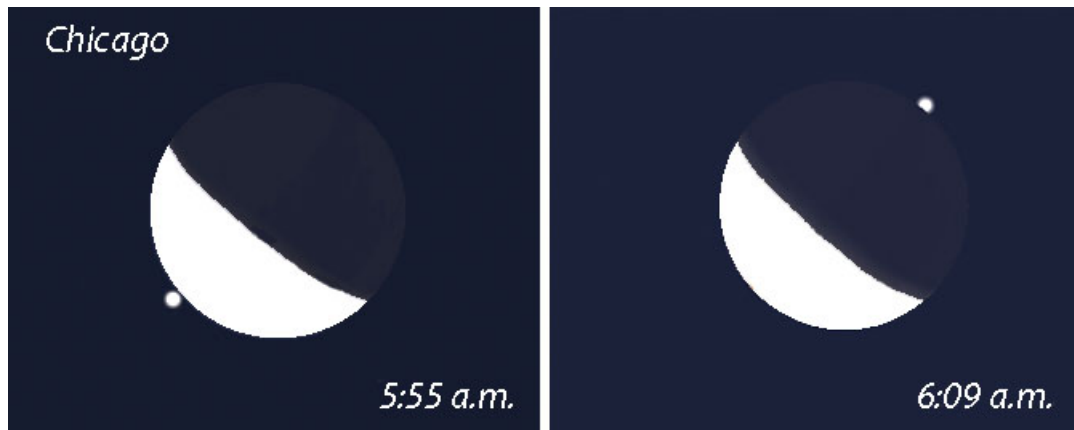


**Figure 3.2:** Ingress (left) and Egress (right). In this case a star occulted by Venus is represented, but the geometry of the occultation is the same for the spacecrafts, too.

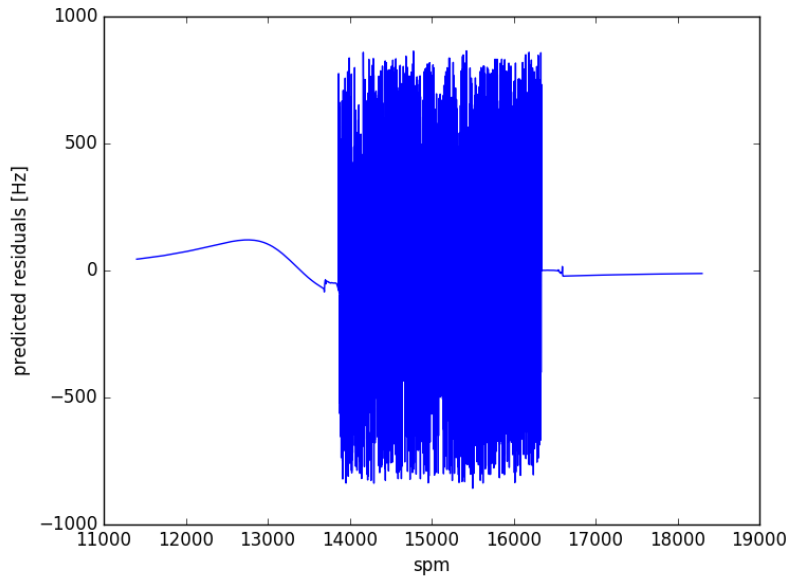
Credits: <https://www.skyandtelescope.com/observing/venus-occults-a-star/>



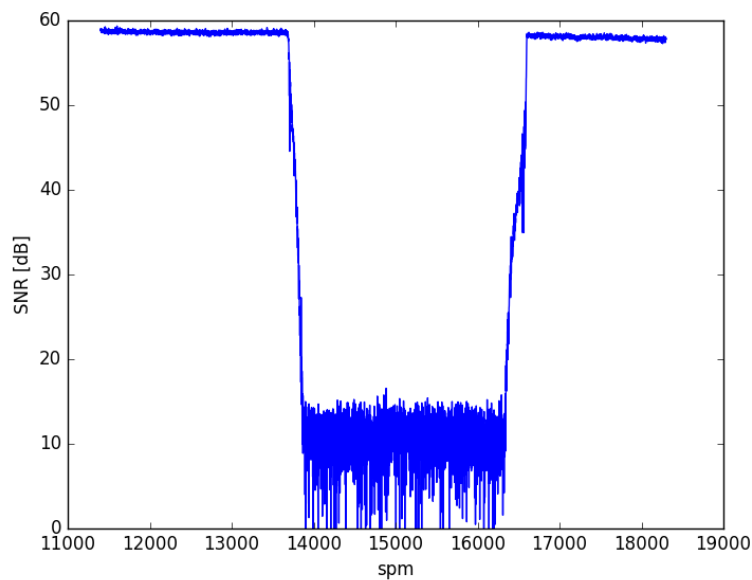
**Figure 3.3:** Grazing occultation of Aldebaran star by the Moon.

As can be seen, the star (or spacecraft) never disappears, it travels slightly above (or under) the planet, so that the signal is always recordable, but weaker due to atmospheric losses.

Credits: <http://astroguyz.com/2017/03/31/astro-vid-of-the-week-an-amazing-grazing-occultation/>



(a)

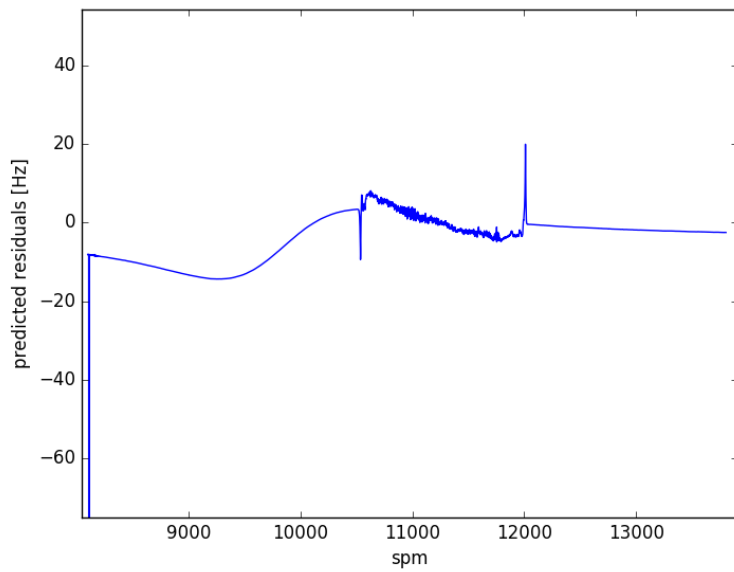


(b)

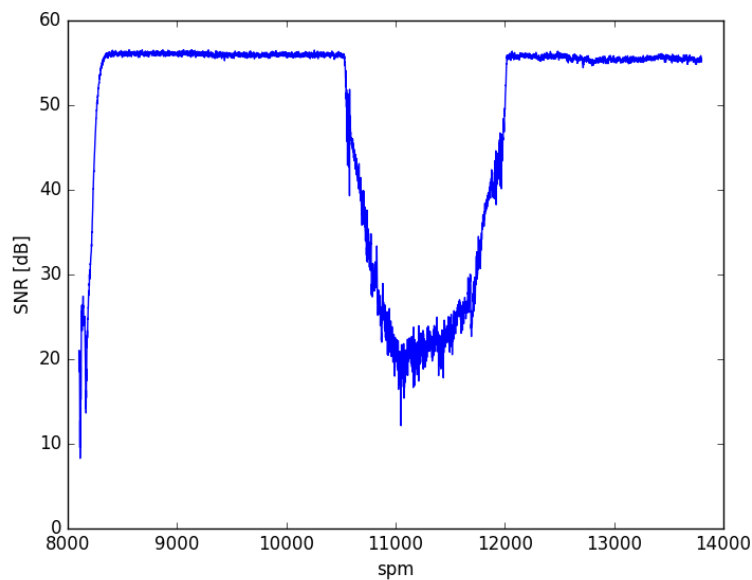
**Figure 3.4:** Ingress/egress typical processed signal of the occultation occurred the 17<sup>th</sup> February 2014, recorded by JPL. **a)** Second past midnight (spm) vs residual frequency: in the middle region the residuals are high and the signal is dominated by noise because the spacecraft was occulted by Venus. **b)** spm vs Signal to Noise Ratio (SNR), in the middle the noise is dominant, so the SNR decreases.

Regarding the Grazing, the spacecraft never disappears behind the planet, so there is not a clear ingress and egress phase, see Figure [3.3](#). Usually, it travels above or under the planet, always visible by the ground stations, but at some point, the signal becomes weaker as it starts passing through the atmosphere of the planet, which cause an amplitude loss. A plot of the typical signal recorded by the ground station during a grazing occultation experiment is reported in Figure [3.22a](#).

The Section [3.3](#) will show the details of the mathematical formulation, presented by Withers (2014) [\[24\]](#), needed to solve the radio occultation problem. In particular, Withers summarize the theories developed in the 60's, optimizing the mathematic formulation of the problem with the goal of developing an algorithm capable to solve the radio occultation problems. The MATLAB algorithm developed in the frame of this investigation follows the guidelines of Withers (2014) [\[24\]](#), as well.



(a)



(b)

**Figure 3.5:** Grazing processed signal of the occultation occurred the 19<sup>th</sup> March 2014, recorded by JPL. **a)** Second past midnight (spm) vs residual frequency. **b)** spm vs SNR: note that with respect to the ingress/egress occultation (Figure 3.4a) the SNR does not decrease as in the previous case, because the spacecraft is not occulted by the planet. The decrease of the SNR is caused by the atmosphere of the planet.

## 3.2 Observables

The state of the spacecraft, or observables, is measured on ground, by collecting the scalar quantities information from the onboard tracking systems. This work has been focused on the two main radiometric measurements: *one-way range* and *one-way range rate*, which have been carried out by the radio science instruments on board the VEX and MGS spacecrafts.

### 3.2.1 One-way range

The range measures the linear distance between the spacecraft and the Earth. The idealized linear distance between the two bodies can be defined as:

$$\rho = \sqrt{[(\mathbf{r} - \mathbf{r}_I) \cdot (\mathbf{r} - \mathbf{r}_I)]} \quad (3.1)$$

where  $\mathbf{r}$  is the position vector of the ground station, while  $\mathbf{r}_I$  is the position vector of the spacecraft, both of them evaluated with respect to the origin of the reference coordinate system (in this case Earth-centered one). The range, is a function of the time, in particular of the specific instant of time at which the observable is measured, so to be precise  $\mathbf{r}_I = \mathbf{r}_I(t - \text{light} - \text{time})$  and  $\mathbf{r} = \mathbf{r}(t - \text{light} - \text{time})$ . In the ideal case, the true range would be the same as the observed range, however due to instrumental limitations, medium propagation, Earth's atmosphere and the dynamics when the spacecraft approaches a planet, the observed range is different with respect to the real and actual radial distance, so that the observed range can be defined as:

$$\rho_{obs} = \rho + \epsilon \quad (3.2)$$

where  $\epsilon$  is the term which considers all the errors.

From the practical point of view, this radiometric measurement can be obtained through the measure of the one-way *time of flight* of a radio signal between the two bodies. In the one-way range, the signal is generated by the spacecraft transponder at time  $t_T$  and received by the ground station at time  $t_R$ , the so called downlink. So the one-way range is [16]:

$$\rho = c(t_R - t_T) + \epsilon \quad (3.3)$$

where  $c$  is the speed of light, and  $\epsilon$  as before takes into account all the errors which are described in the described la

### 3.2.2 One-way range rate

Range-rate measurements are related to the rate of change, with respect to time, of the radial distance between the spacecraft and the ground station. The range-rate, from the mathematical point of view can be obtained by differentiating in time the Equation [3.1](#). Or from the practical point of view could be seen as:

$$\dot{\rho}_{obs} = \dot{\rho} + \epsilon \quad (3.4)$$

where  $\epsilon$  represents the errors as before.

Furthermore, with some mathematical definitions and manipulations (for the details see [\[16\]](#), Section 3.2.2), the range-rate could be related to the recordings of the Doppler shift of a radio signal, which has been the core of this work:

$$f_T - f_R = \Delta f = f_T \frac{\dot{\rho}}{c} \quad (3.5)$$

where  $f_T$  is the transmitted frequency from the spacecraft, while  $f_R$  is the received frequency at the ground station.

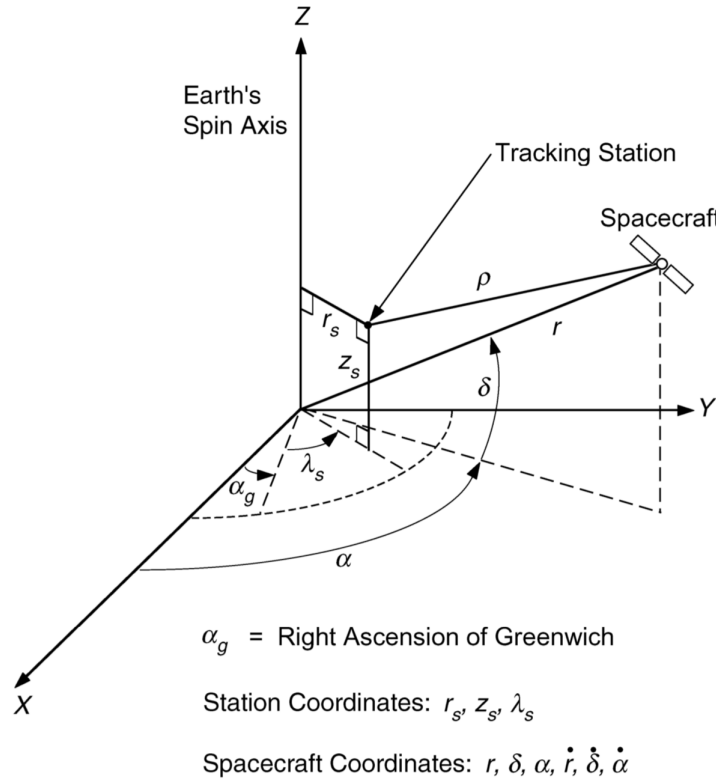


**Figure 3.6:** Range definition and reference coordinate systems for the spacecraft and ground station. Credit: NASA

### 3.3 Signal Processing

The spacecraft's signals used within the framework of this research have been recorded by the NASA Deep Space Network (DSN). As explained in Subsection [2.5.2.1](#), in order to eliminate the loss of data due to closed-loop receiver lock-up time at the occultation egress, an open-loop reception method is the one adopted. The signal recorded from the ground stations, must be processed in order to get the frequency residuals, which are the inputs of the MATLAB algorithm developed. From the general point of view, the signal must be converted from the time domain to the frequency domain, then after some manipulations and evaluations, the frequency residuals can be computed. A detailed explanation of all the steps covered within the Signal Processing is provided in the next subsections.

### 3.3.1 Data information

The Venus occultation data selected comes from Venus Express, which are one-way link, single frequency X-band, from 2014. On the other hand, for Mars, the occultation data is from Mars Global Surveyor, one-way, single frequency X-band. Before discussing the steps of the signal processing, it is interesting to show the information of the data collected, see Figure 3.7.

```

DATE OF GENERATION: Fri Jan 3 22:03:54 2020
REPORT FOR FILE: 248VEOE2014044_0325NNNX43RD.1B1

Start Time: 2014 044 03:25:01
End Time : 2014 044 05:10:00   Elapsed Time : 6299 seconds
Pass No.: 44                   Tracking Mode: 1-Way
Spacecraft No.: 248           DSS No.: 43
RSR ID: 2 Sub 1               Processing Center: 40
Sample Rate: 2000 per second   Sample Resolution: 16 bit
Uplink Band: N/A              Downlink Band: X
First Record Seq. No.: 1      Last Record Seq. No.: 6300

```

**Figure 3.7:** Information about the occultation data  
248VEOE2014044\_0325NNNX43RD.1B1  
occurred on the 13<sup>th</sup> February 2014.

Each datafile is classified with its *Start Time* and *End Time*, in which the *Year* and the *Day of the year* (DOY) are also reported. For example, the DOY 044 is referred to the 13<sup>th</sup> of February 2014. The *Spacecraft No.* 248 stands for the ID number of the spacecraft, in this case Venus Express; the *Sample Rate* is referred to the sampling of the signal, which is the reduction of a continuous-time signal to a discrete-time signal. The sampling frequency or sampling rate,  $f_s$ , is the average number of samples obtained in one second (samples per second), thus  $f_s = 1/T$ , see Figure 3.8.

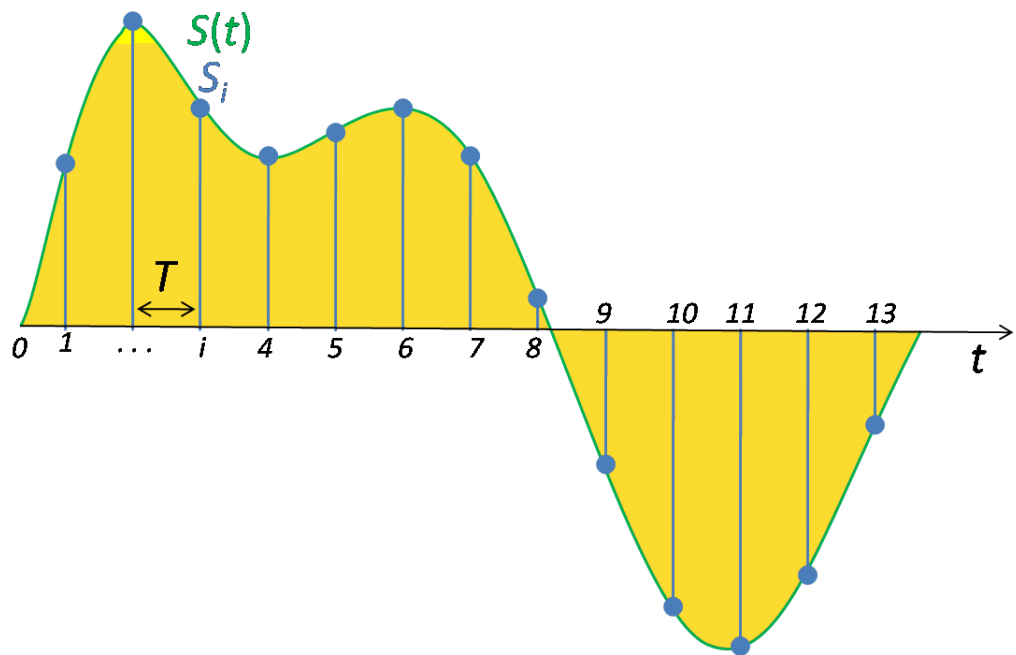


**Figure 3.8:** Signal sampling representation. The continuous signal (green colored line) is replaced by the discrete samples (blue vertical lines).  
Credit: <https://en.m.wikipedia.org>

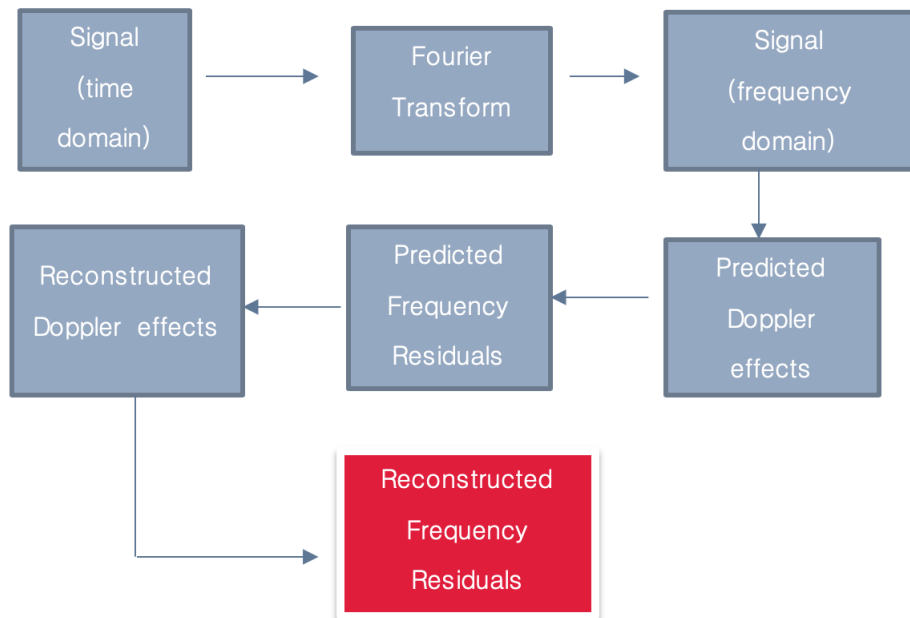


**Figure 3.9:** Outline of the Signal Processing.

Another important information is the *Tracking Mode*, which, as explained in Section 2.5.1, for radio science experiments (especially egress occultations) is usually set as one-way link. This is the reason why in the signal information of Figure 3.7 only the Downlink Band (for this data the X band, which refers to a frequency of 8.4 GHz) is reported. The ground stations, in fact, is not sending any signal to the spacecraft, and the whole experiment relies on the frequency sent by the spacecraft and so by the efficiency of the Ultra Stable Oscillator onboard the spacecraft, which provided a high-quality onboard reference frequency source. The Figure 3.9 shows the outline of the work needed to process the data, which will be explained in details, step by step.

### 3.3.2 Signal (time domain)

The time-domain carrier signal recorded by the DSN can be defined as a sine wave or sinusoid, as Equation 3.6, and a typical plot is reported in Figure 3.10.

$$A(t) = A\sin(2\pi ft) + n(t) \quad (3.6)$$

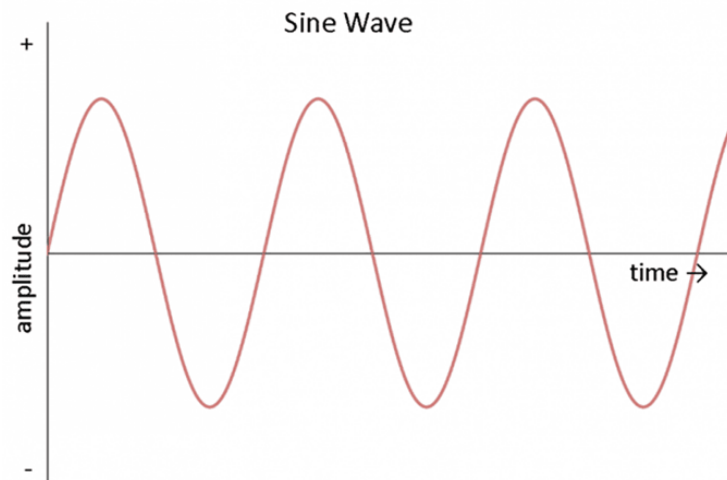


**Figure 3.10:** Sine wave. Credit: <https://www.investopedia.com/terms/s/sinewave.asp>

This signal is typically represented in a plot with the time in the x-axis and the amplitude in the y-axis. However, since the goal of the *Signal Processing* is to obtain the reconstructed frequency residuals of the signal received from the spacecraft, as a first step the signal must be transformed in the frequency domain. Then, after

some manipulations the frequency residuals will be analyzed, through the Abel transform, and will unveil the atmospheric properties of the target. So, the first task of this work has been to process the VEX data, starting from a time-domain signal and converting it into the frequency-domain. The tool which permits to do this conversion is the Fourier Transform, which is addressed in the next subsection.

### 3.3.3 Fourier transform

The Fourier transform decomposes a function of time into its constituent frequencies. The Fourier transform of a function in the time-domain is itself a complex-valued of frequency, whose magnitude (the modulus) represents the amount of that frequency present in the original function, and whose argument is the phase offset of the basic sinusoid in that frequency.

The Fourier transform of a function  $f$  can be expressed as  $F$  by:

$$F\{g(t)\} = G(f) = \int_{-\infty}^{\infty} g(t)e^{-2\pi i f t} dt \quad (3.7)$$

As a result,  $G(f)$  gives how much power  $g(t)$  contains at the frequency  $f$ .  $G(f)$  is often called the spectrum of  $g$ . A simple example to understand how the Fourier transform works is reported here, where the box function of Figure 3.11 is analyzed.

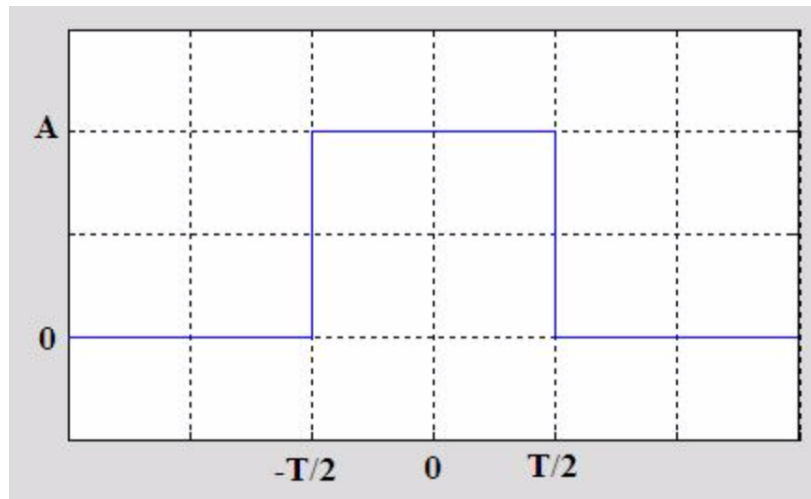


**Figure 3.11:** Box function (time domain).

Credit: <http://www.thefouriertransform.com>

By evaluating the Fourier Transform on the box function, the result is:

$$\begin{aligned}
 F\{g(t)\} = G(f) &= \int_{-\infty}^{\infty} g(t)e^{-2\pi ift} dt \\
 &= \int_{-T/2}^{T/2} Ae^{-2\pi ift} dt = \frac{A}{-2\pi if} \left[ e^{-2\pi ift} \right]_{-T/2}^{T/2} \\
 &= \frac{A}{-2\pi if} [e^{-\pi ifT} - e^{\pi ifT}] = \frac{AT}{\pi fT} \left[ \frac{e^{\pi ifT} - e^{-\pi ifT}}{2i} \right] \\
 &= \frac{AT}{\pi fT} \sin(\pi fT) = AT [\text{sinc}(ft)]
 \end{aligned} \tag{3.8}$$

The plot of the Fourier Transform of the box function, in the frequency-domain, is reported in Figure [3.12](#).

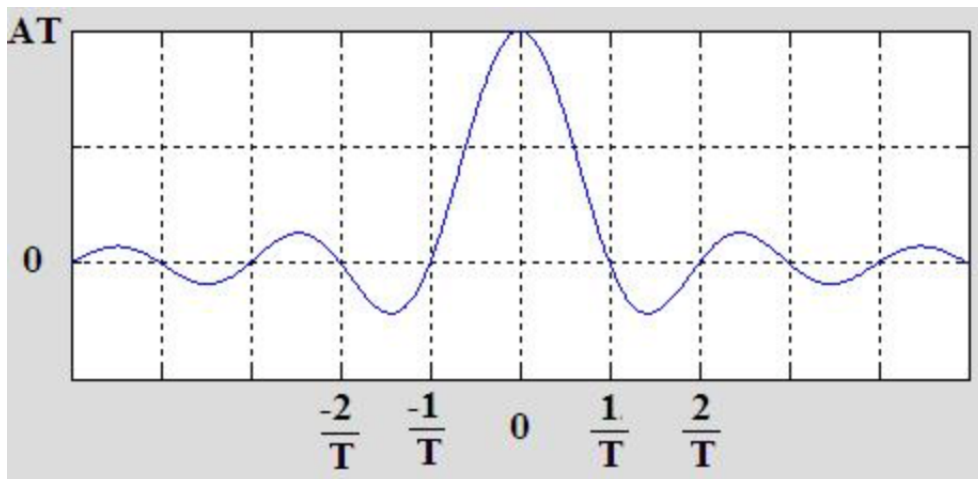


**Figure 3.12:** Spectrum of the box function.

Credit: <http://www.thefouriertransform.com>

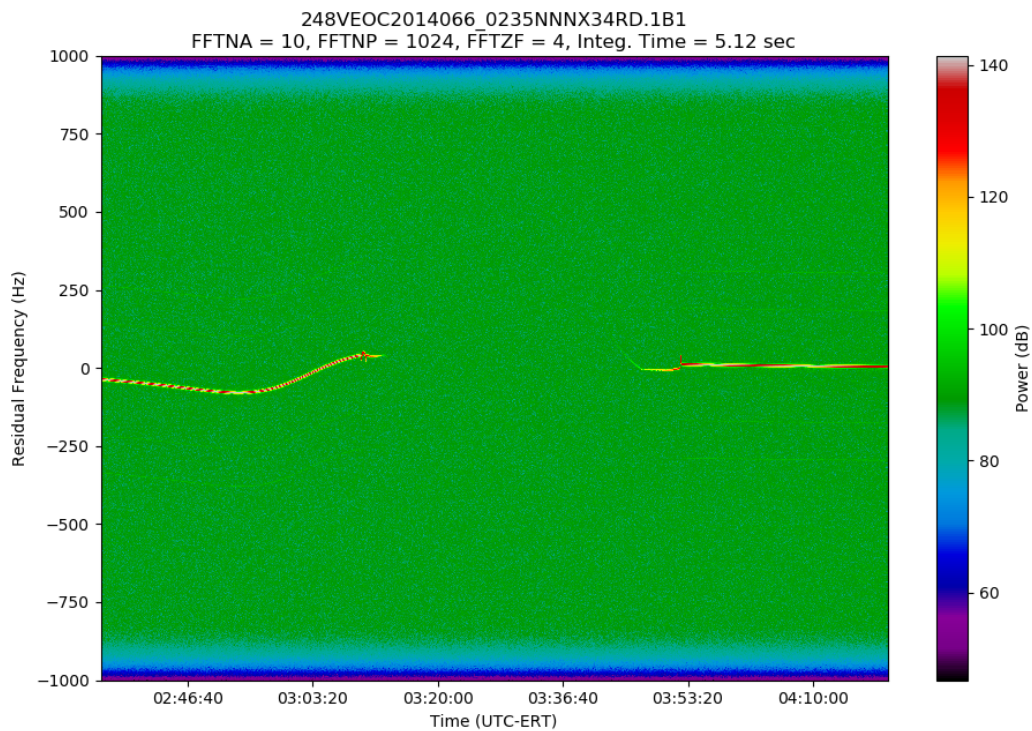
The Fourier Transform permits to convert the signal from the time domain (Figure [3.11](#)), to the frequency domain, as in Figure [3.12](#). Furthermore, the Fourier Transform is extremely useful to highlight the component frequencies of the signal recorded, which is the first step to get the frequency residuals.

### 3.3.4 Signal (frequency domain)

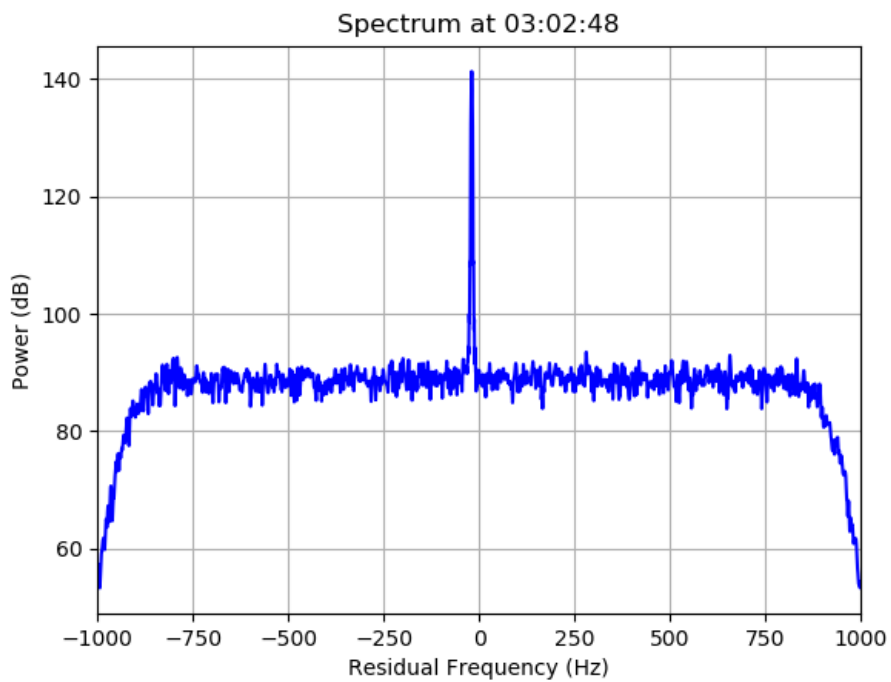
From the practical point of view, this process can be observed by running a JPL spectrogram tool, which first of all highlight the power of the recorded signal during the experiment, see Figure [3.13](#). Then, for each selected point the tool runs a FFT algorithm in order to show the main component frequency of the signal at the instant of time selected, see Figures [3.14](#) ; [3.15](#). By studying the signal in the frequency-domain, as for example the one reported in Figure [3.14](#), which is related to one of the VEX data recorded by the Deep Space Network of NASA and managed by JPL, is possible to understand which is the main frequency, also called component frequency, of the recorded signal at a certain instant of time.

In Figure [3.14](#) a spectrum of the signal recorded at the Deep Space Station 43 has been computed through a Jet Propulsion Laboratory tool, which evaluate the predicted residual frequencies of the recorded signal and its power. To do so, it runs a Fast Fourier Transform algorithm, also called FFT, which computes a Discrete Fourier Transform (DFT) on the signal. The residual frequency, also called predicted frequency residual, showed in the plot are the difference between the observed frequency (skyfrequency) and the predicted frequency. Thanks to this tool is possible to obtain the main frequency (or main component frequency) of the signal at a certain instant of time (in this case at 03:02:48 of the 7<sup>th</sup> March 2014). The component frequency is the one characterized by the highest power and is collected, and used, for the next steps of the signal processing. All the others low-power frequencies showed in the plot represent the noise present in the recorded signal. This process can be done with different accuracies depending on how much samples of the signal are being considered. Within this work the signals are processed with a time-step of 0.25 seconds or 0.5 seconds (so each 0.25 or 0.5 seconds of the time-domain signal a reference frequency will be collected), which represents a good trade-off between the number of points analyzed and the thermal noise. In fact, by decreasing the integration time, the thermal noise introduced by the FFT increases, so the quality of the frequency residuals decreases, leading to a higher uncertainty in the results. A detailed explanation of the selection of the time-step and the noise related to it will be provided in the Section [4.3](#).

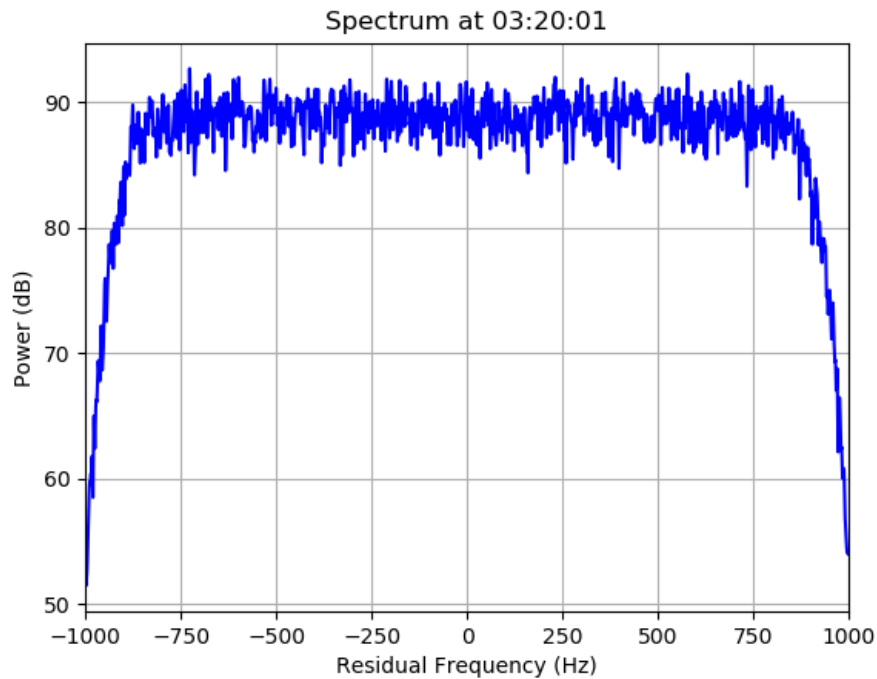
To conclude this subsection, it is interesting to show how the spectrum of the received signal looks like when the spacecraft is occulted by the planet, see Figure



**Figure 3.13:** Spectrogram of the VEX radio signal recorded by the DSN on the ingress/egress occultation of the 7<sup>th</sup> March 2014.



**Figure 3.14:** Spectrum and main component frequency of the VEX radio signal at the 03:02:48 of the 7<sup>th</sup> March 2014.

**3.15.**

**Figure 3.15:** Noise present in the signal when VEX was occulted by the planet. The FFT algorithm is not able to evaluate the main component frequency because there was no signal coming from the S/C, since it was occulted by Venus.

As can be seen from Figure 3.15, the recorded signal is not characterized by a dominant frequency (as in Figure 3.14), this means that the ground station is mainly recording noise, and the spacecraft is not communicating with the receiver. In fact, from the orbital point of view, in this occultation example at the 03:20:01 the spacecraft was occulted by Venus, and the DSS-43 received its signal around the 03:40, again. Another important parameter which is related to the signal processing, is the Signal to Noise Ratio (SNR) which is defined as:

$$SNR = \frac{P_{signal}}{P_{noise}} \quad (3.9)$$

where P is average power.

Both signal and noise power must be measured at the same or equivalent points in a system, and within the same system bandwidth. An example of the SNR

of the signal received and collected by JPL on Venus Express (DOY 044 2014) is reported in Figure 3.16.

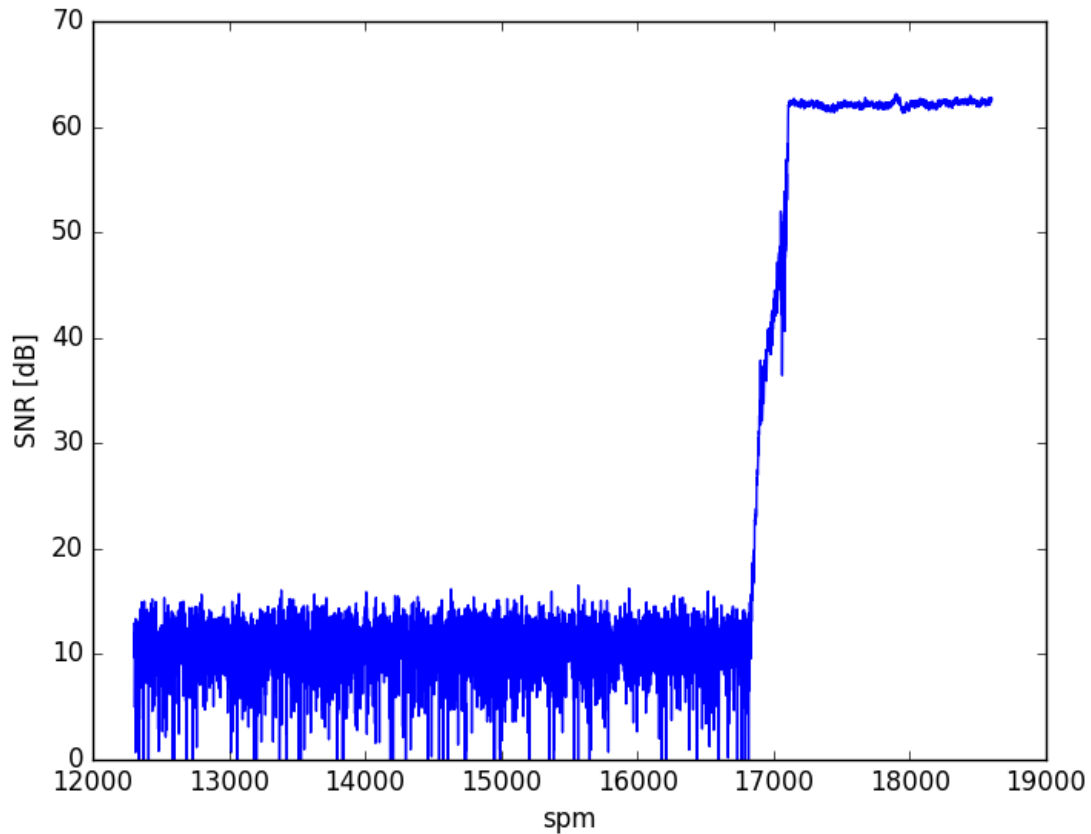


**Figure 3.16:** Signal to Noise Ratio (SNR) of the occultation of VEX on the 13th February 2014.

By looking at Figure 3.16 is possible to understand clearly what explained before: the spacecraft is occulted by Venus when the SNR (in dB) is low (lower signal and same noise) and then as soon as the egress starts the SNR increases. This plot is a typical example of an egress occultation. The SNR is helpful to understand from the general point of view when the occultation is taking place and when the signal is received by the DSS. However, especially in the atmosphere region the ground station is usually able to receive the signal even if the SNR is low, so there is not a common threshold value between all the occultation experiments.

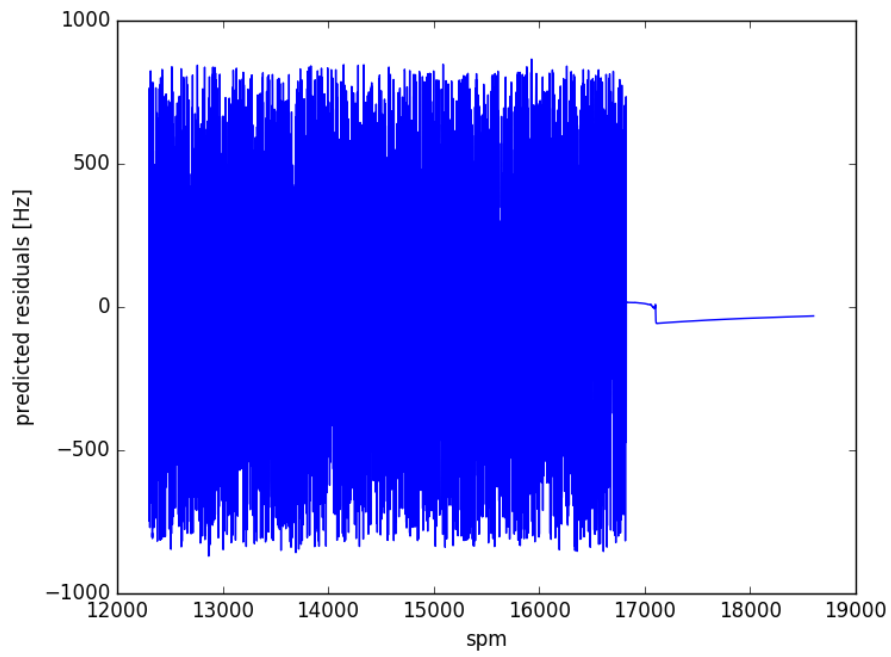
To understand when the occultation started and ended, without losing crucial data, is preferable to use the FFT algorithm, which is able to extrapolate the main frequency from the signal, if this exists, even when the SNR is low.

### 3.3.5 Predicted frequency residuals

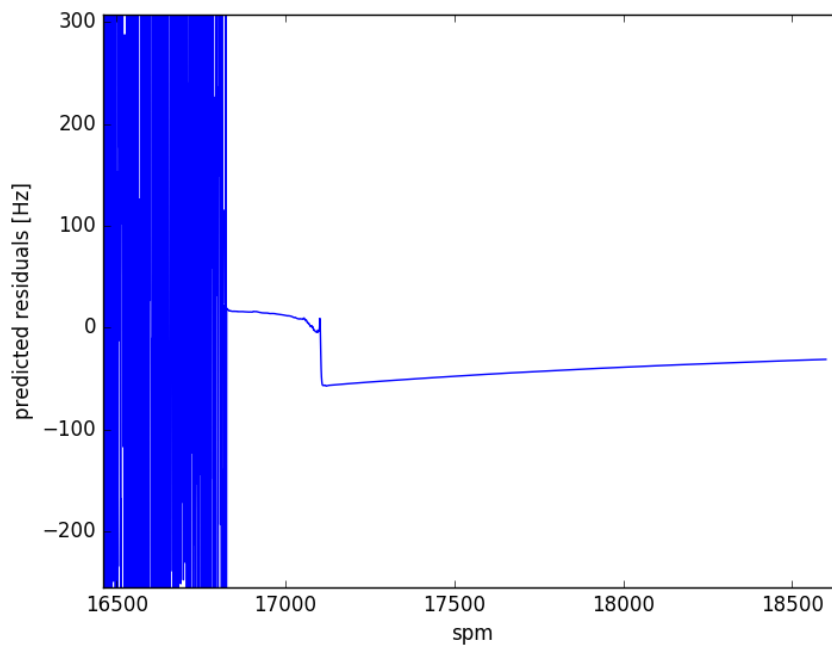
Since the main component frequencies of the incoming signal are now available, the next step is to compute the predicted frequency residuals  $\Delta f_{predicted}$ . These are defined as:

$$\Delta f_{predicted} = f_{observed} - f_{predicted} \quad (3.10)$$

Where  $f_{predicted}$  is the frequency sent by the spacecraft, generated by the Ultra Stable Oscillator and corrected for the predicted Doppler effects, while  $f_{observed}$  is the frequency observed at the ground station (after the processing of the recorded signal, as explained before). Note that these frequency residuals are called predicted because, at this step, the Doppler effects which are considered are the ones predicted, before the occultation experiment through the navigation models. Then after the occultation, the Navigation team is able to compute, with more precision, the positions and velocities of the spacecraft, target and receiver, so that the reconstructed Doppler effects are made available, leading to a higher accuracy of the computation. Another JPL tool has been used to compute the predicted frequency residuals. The method behind this tool is a summary of what explained before: an FFT algorithm is performed on the signal in the time domain so that the main component frequencies are acquired; then these recorded frequencies are compared with the predicted ones and a plot of the residuals vs time is finally available, see Figure [3.17](#).



(a)



(b)

**Figure 3.17:** a) Predicted frequency residuals of the egress occultation of 13th February 2014. b) closer look on a).

As can be seen from Figure 3.17, after the noise due to the occultation, there is an almost linear trend. This represents that the ground station is able to receive the spacecraft signal. In addition, since this is an egress, the first part after the noise is the most important occultation data, which contains all the atmosphere's information needed. Then as the time goes on, the spacecraft exits the atmosphere of the planet, and the signal collected in this region (slightly before 17500 spm in the Figure 3.17) is usually called baseline. A good baseline, which means a trend of the frequency residuals characterized by a zero mean value is fundamental in order to perform correctly the Abel transform, and so to obtain reliable results. The meaning of "a good baseline" will be showed in the calibration Section 4.4. Another important aspect, which can be analyzed from the Figure 3.17, is the peak present after 17000 spm. The almost linear trend, between the noise and the 17000 spm, is interrupted by that peak, then another linear trend re-starts. The meaning of this interruption is related to the fact that the Venus' atmosphere is not correctly modeled. In fact, the tools which perform the predicted frequency residuals, evaluate the predicted frequency taking into account the atmosphere effects of the target, this in order to keep the signal in the band when the data was recorded. On the other hand, the atmosphere of the target will not be taken into account when performing the reconstructed frequency residuals, so that the total atmosphere signature of the target will be considered within the Abel transform algorithm.

### 3.3.6 Doppler effect

The atmosphere of the target and the plasma noise present in the interplanetary medium are not the only terms responsible in modifying the frequency of the signal transmitted from the spacecraft to the receiver. In fact, also the relative radial velocity between the spacecraft and the DSS causes the so-called Doppler shift or Doppler Effect, which affects the frequency of the signal, as well. This effect does not depend on the frequency of the electromagnetic wave and was discovered by Christian Doppler (1803-1853). It causes the observed frequency to differ from the radiated frequency of the source if there is motion that is increasing or decreasing the distance between the source and the observer, see Figure 3.18. If the distance between the source and receiver of electromagnetic waves remains constant, the frequency of the source and received wave forms is the same. If the

distance between the source and receiver of electromagnetic waves is increasing, the frequency of the received wave forms appears to be lower than the actual frequency of the source wave form. Each time the source has completed a wave, it has also moved farther away from the receiver, so the waves arrive less frequently. Lastly, when the distance is decreasing, the frequency of the received wave form will be higher than the source wave form. This is due to the fact that since the source is getting closer, the waves arrive more frequently. The Doppler effect is measured in the frequency signals received by the ground stations when tracking the spacecrafts. This effect may be caused by a combination of the spacecraft's trajectory, its orbit around a planet, Earth's revolution about the sun, and Earth's daily rotation on its axis. For example, a spacecraft approaching the Earth, will add a positive frequency bias to the received signal.

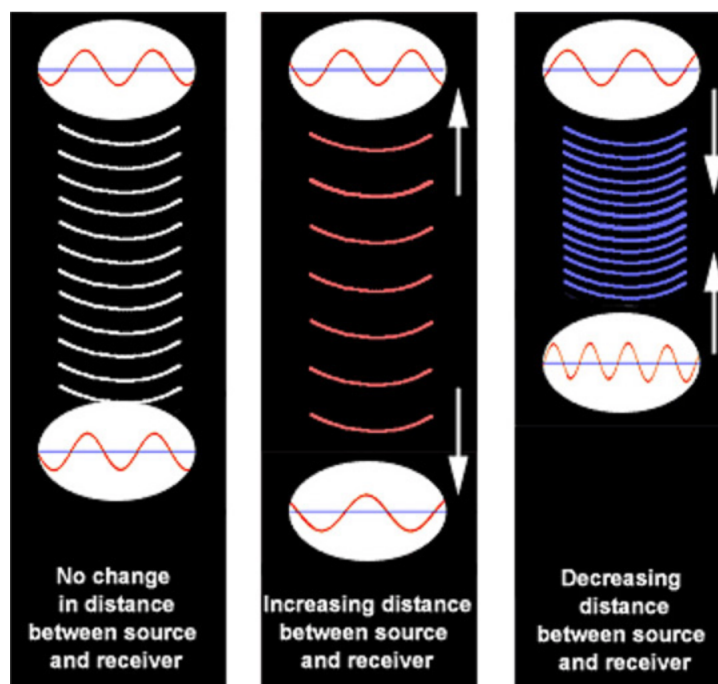


**Figure 3.18:** Examples of Doppler effect. Credit: NASA Science

The Navigation team collects the ephemeris, which are the trajectories (i.e. the positions and velocities over time) of astronomical objects as well as artificial satellites in the sky and are the ones used to evaluate the reconstructed Doppler Ef-

fect. As explained before, from the navigations models is also possible to estimate the trajectories and so the predicted doppler effects, but the greatest accuracy comes from the reconstructed ones. The ephemeris evaluated by the Deep Space Network are available at the “Planetary Data System Navigation Node – NAIF” (at <https://naif.jpl.nasa.gov/pub/naif/>). Before evaluating the Doppler effects, a setup of SPICE (the observation geometry system for space science missions), and all the files needed for these computations, has been made in MATLAB and on the remote machine of JPL (via Terminal).

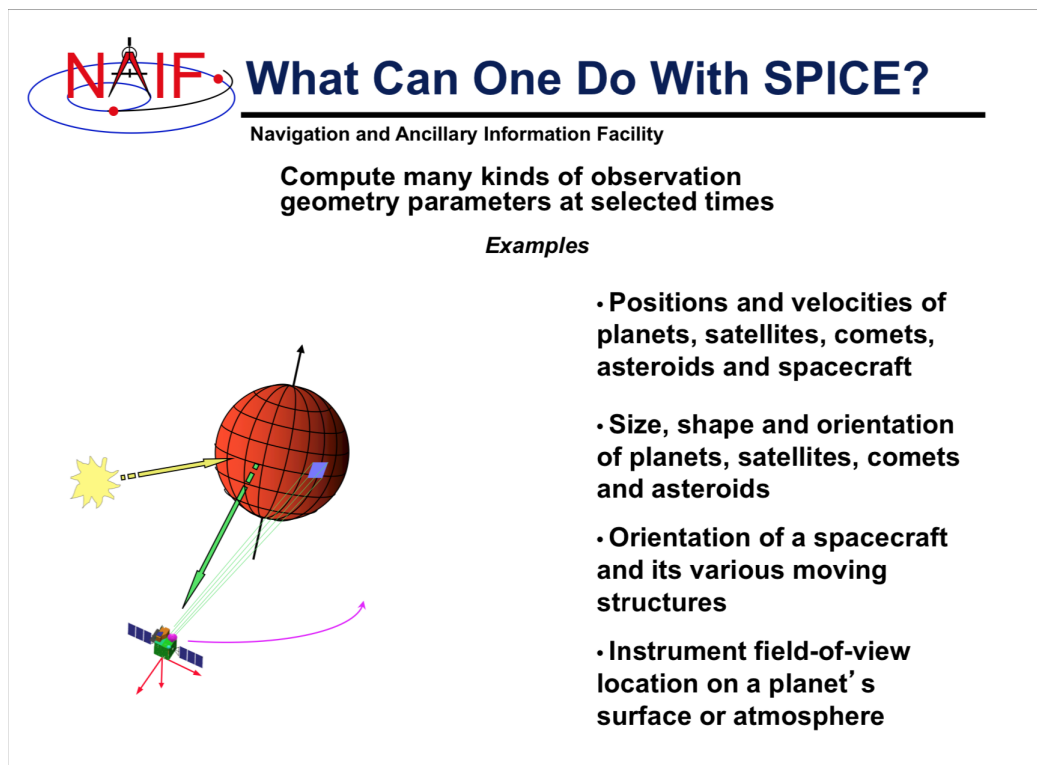


**Figure 3.19:** Examples of SPICE computations. Credit: NAIF, NASA-JPL

In Figure 3.19 are reported some of the many computations which can be obtained through SPICE. The ephemeris files needed for the desired computations within SPICE, as well as the evaluation of the Doppler effects, are collected in Kernels, see Figure 3.20. Depending on the computation needed, SPICE gets information from different Kernels and return the desired output. Examples of Kernels are the SPK which collect the positions of planets, satellites, comets and asteroids ephemerides; the Pck, which contain Planets, satellites, comets and

asteroids orientations, sizes and shapes; FK in which information on the definitions of and specification of relationships between reference frames (coordinate systems) can be found. In case one or more kernels are missing, or if the kernels loaded do not match the time-frame of the computation, errors will show up.

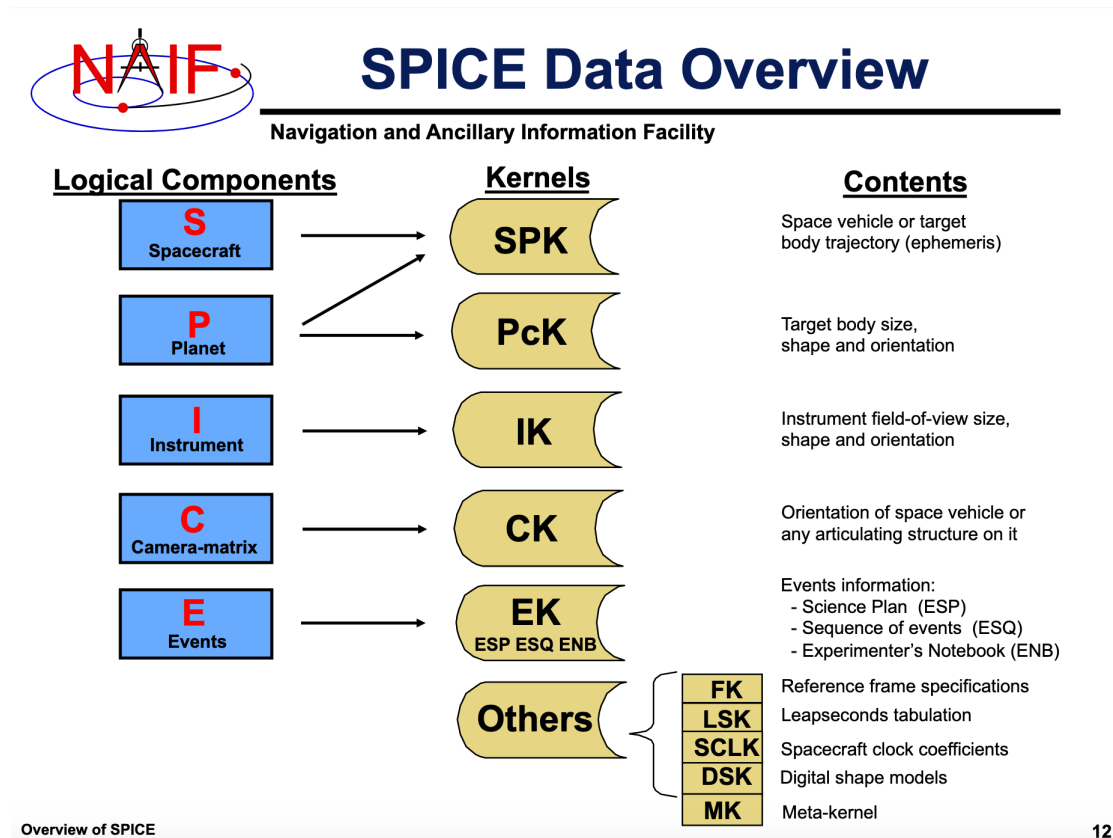


**Figure 3.20:** Kernels of SPICE. Credit: NAIF, NASA-JPL

For the Venus Express mission, as well as for MGS, all the kernels needed have been collected in a Meta-kernel, which is a SPICE text kernel that collects the names of the kernels to use together, see Figure 3.21. These meta-kernels, have been used both in the Abel Transform algorithm (developed in Matlab environment, and explained in Chapter 4) and in the JPL tool which returned the reconstructed frequency residuals.

```

\begin{code}
\begin{data}
PATH_VALUES = ('/Users/egramign/Documents/MATLAB/SPICE/mice/kernels')
PATH_SYMBOLS = ('A')
KERNELS_TO_LOAD = (
  '$A/lsk/naif0010.tls',
  '$A/fk/planets/earthfixeditr93.tf',
  '$A/fk/spacecrafts/vex_v10.tf',
  '$A/fk/stations/earth_topo_050714.tf',
  '$A/fk/planets/rssd0002.tf',
  '$A/pck/de403-masses.tpc',
  '$A/pck/earth_000101_150330_150107.bpc',
  '$A/pck/pck00010.tpc',
  '$A/sclk/vex_141112_step.tsc',
  '$A/spk/planets/de405.bsp',
  '$A/spk/stations/earthstns_itr93_050714.bsp',
  '$A/spk/orvy_140101000000_00530.bsp',
  '$A/spk/orvy_140201000000_00536.bsp',
  '$A/spk/orvy_140301000000_00542.bsp',
  '$A/spk/orvy_140401000000_70000.bsp',
  '$A/spk/orvy_140501000000_00546.bsp',
  '$A/spk/orvy_140601000000_00546.bsp',
  '$A/spk/orvy_140701000000_00551.bsp',
  '$A/spk/orvy_140801000000_00556.bsp',
  '$A/spk/orvy_140901000000_00560.bsp',
  '$A/spk/orvy_141001000000_00564.bsp',
  '$A/spk/orvy_141101000000_00569.bsp',
  '$A/spk/orvy_141201000000_00569.bsp'
)
\end{code}

```

Figure 3.21: Meta-kernel created to analyze the Venus Express data of JPL.

### 3.3.7 Reconstructed frequency residuals

Thanks to the predicted frequency residuals, and the meta-kernel setup, is finally possible to compute the reconstructed frequency residuals, which is the goal of this Section.

These residuals are defined as:

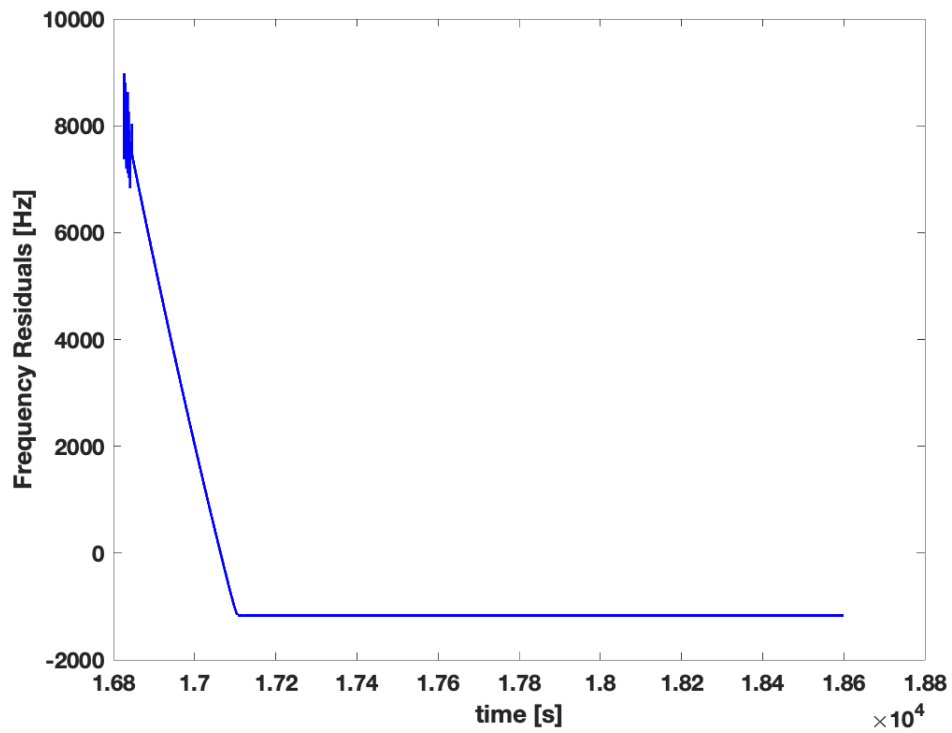
$$\Delta f_{reconstructed} = f_{observed} - f_{reconstructed} \quad (3.11)$$

Where  $f_{reconstructed}$  is the signal frequency of the spacecraft corrected for the reconstructed Doppler effects;  $f_{observed}$  is the observed frequency by the DSS, or sky frequency, obtained by adding predicted frequency to the predicted frequency residuals. As explained before, the reconstructed frequency residuals are the main input needed for the Abel transform algorithm, which permits to obtain the atmospheric parameters of the target by processing the residuals and the geometry of the occultation. The JPL tool used for the evaluation of the reconstructed

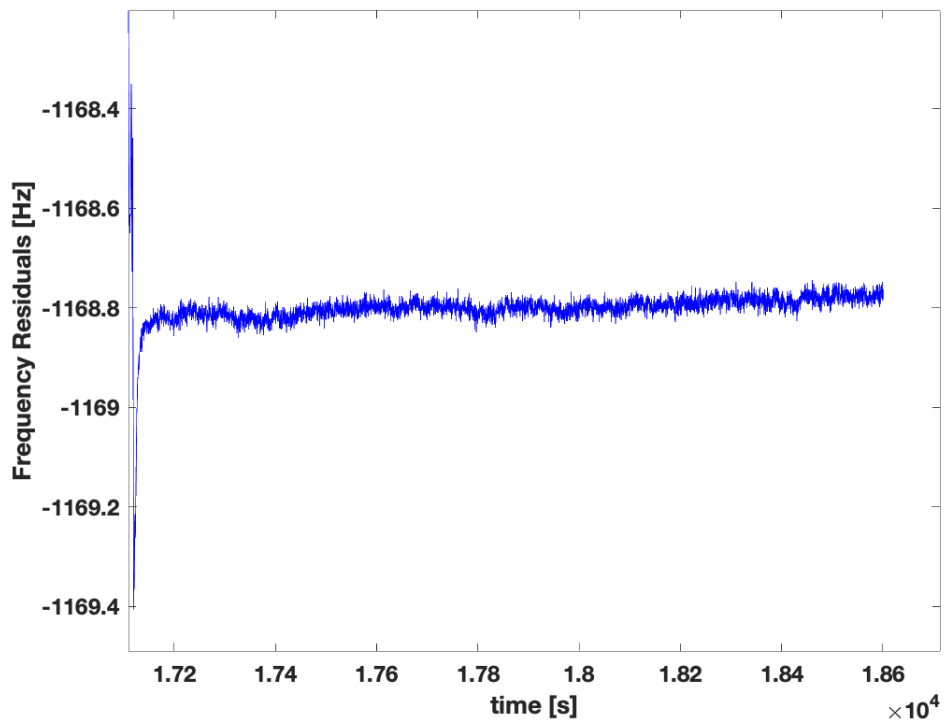
---

frequency residuals takes as input the observed frequency (skyfrequency) and the meta-kernel (SPICE file input): it evaluates firstly the Ultra Stable Oscillator reference frequency of the Spacecraft, it corrects this reference frequency with the reconstructed Doppler effects (through the meta-kernel and SPICE computations) so that the reconstructed frequency is evaluated; then it compare the reconstructed frequency with the recorded one, to give as output the frequency residuals. This processed is done for each time step, so that in the end, the reconstructed frequency residuals are available as a function of time, see Figure [3.22](#).

The plot of Figure [3.22](#) represents the reconstructed frequency residuals for an egress occultation of VEX at Venus. The first part, where the residuals show high values is the Venus' atmosphere signature. These frequency residuals almost reach 8000Hz, which is an extremely high value if compared to the typical frequency residuals from Mars' atmosphere (typically 1-2 Hz maximum). In fact, this is due to the effect of the dense atmosphere of Venus, which strongly refracts and bents the radio signal sent by the spacecraft, resulting in a strong frequency shift of the signal. Moreover, by looking at the baseline (which is the region of the frequency residuals outside the atmosphere of the planet) of these frequency residuals of Figure [3.22b](#) is possible to notice that they are not characterized by a zero mean value. This is the reason why, within the post processing and especially for Venus, the frequency residuals must be calibrated before being analyzed by the Abel transform. Otherwise the algorithm will not be able to perform correctly the numerical integrations and the results will not be reliable. Section [4.4](#) will provide all the details regarding the Calibration process: in particular for Mars a first order polynomial fit was used for calibrate the residuals, while for Venus a second order (and sometimes even higher order for the ingress cases) polynomial was required. This calibration process is needed to correct for all the errors present in the measurements, coming from the spacecraft clock, thermal noise, plasma noise and the dynamics of the planet which influence the estimated trajectory.



(a)



(b)

**Figure 3.22:** a) Reconstructed frequency residuals of the VEX egress occultation occurred the 13th of February 2014; b) closer look on the baseline.

### 3.4 Processing of radio occultation data

The goal of this section is to provide a detailed explanation, as well as instructions, for one critical aspect of radio occultation data processing: how to determine vertical profiles of atmospheric properties from time series of frequency residuals. The information reported here are mainly from Withers (2014) [24], a paper which collects the classical radio occultation theories (from Phinney, Anderson, Fjeldbo, Kliore, Yakovlev...) and explains how to deal with them from the practical point of view, in order to create a functional radio occultation processing tool. Furthermore, these information have been used in order to develop an algorithm within a MATLAB environment, which transforms the frequency residuals into relevant atmospheric parameters, see Chapter 4. The model has been validated with the results presented by Withers (2014) on a Mars Global Surveyor (MGS) occultation and with other two occultations from Venus Express, which results can be found from Pätzold (2007) [17]. Then, the model has been adapted for the Venus' atmosphere analyses. As already explained in the Section 3.1, radio occultation investigations transmit a radio signal, which during its journey from the transmitter to the receiver, it travels in the target's atmosphere. Then, this signal is refracted in the neutral gas and ionospheric plasma around the target object, so that the frequency of the radio signal is affected. By studying the time series of the received radio frequency is then possible to retrieve vertical profiles of relevant atmospheric parameters as number density of neutral gas, electron density of ionospheric plasma, pressure and temperature. First of all, in geometric optics the relation between the direction of propagation of a ray and the refractive index  $n$  (which is one of the primary environmental property) is given by:

$$\frac{d}{dl} \left( n \hat{l} \right) = \nabla n \quad (3.12)$$

Where the unit vector  $\hat{l}$  is defined as the direction of propagation of the ray. As a consequence, the radio ray bends as it passes through an atmosphere and/or ionosphere, and the bending angle depends on the refractivity of the target's environment through which the ray travels. Furthermore, the refractive index as a function of radial distance to the target could be obtained from the dependence of bending angle on impact parameter (this is valid only under certain assumptions, which will be explained later). In fact, the relation between the impact parameter

and the bending angle is extremely useful, since it permits to obtain firstly the refractive index, which in turn permits to retrieve radial profiles of neutral and plasma densities. So the first step would be to determine the bending angle as a function of the impact parameter; the bending angle is not directly observable, but it can be obtained by studying the frequency residuals.

### 3.4.1 Frame of reference definition

In radio science experiments, the selection of the frame of reference is fundamental, since it permits to consider certain assumptions and so it can simplify the problem a lot. The frame of reference selected is the one introduced by [7] but with different symbols, see Figure 3.23.

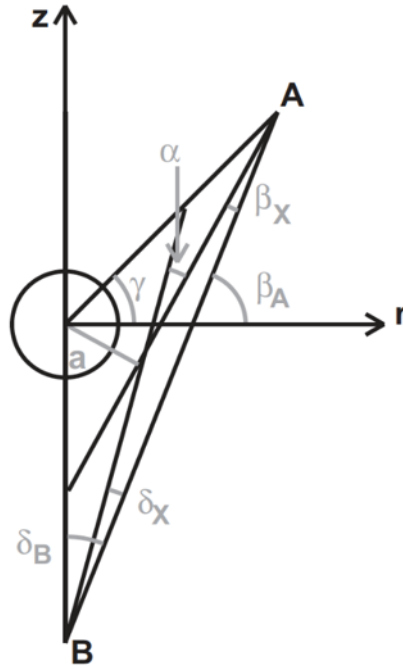


**Figure 3.23:** Frame of reference adopted, and geometry for a radio occultation experiment involving transmitter A, receiver B, and target P at the origin of the reference system.

In Figure 3.23, the transmitter at  $x_A$  (in this case Venus Express) sends a radio signal at time  $t_A$ , which is received by the receiver at  $x_B$  at time  $t_B$ . Note that  $x_i$  represent the vector position at location  $i$ . The radio signal sent from the spacecraft

does not follow the straight line path between the transmitter and the receiver. In fact, it starts with a certain angle difference with respect to that path, but still on a straight line. Then, the signal travels through the ionosphere and atmosphere of the target, it is refracted and so it changes the direction of propagation, emerging then still on a final straight line path towards the location of the receiver at time  $t_B$ . The initial and final straight line paths are the so called asymptotes of the ray path. From these is possible also to obtain the impact parameter  $a$ . Furthermore,  $x_0$  is defined as the position of the point of closest approach of the radio signal transmitted at time  $t_A$  to the target object P, and  $t_0$  is the time related to this event. It is important to note that the two asymptotes intersect at  $x_X$  but  $x_0 \neq x_X$ . Obviously, an accurate knowledge of the times  $t_A$ ,  $t_B$  and  $t_0$  is extremely important for the experiment. Errors in these times can have a great impact on the results. The frame of reference of Figure [3.23](#) has the origin at  $x_P(t_0)$  and is defined as:

$$\begin{aligned}\hat{z}(t_0) &= \frac{(\underline{x}_P(t_0) - \underline{x}_B(t_B))}{|(\underline{x}_P(t_0) - \underline{x}_B(t_B))|} \\ \hat{n}(t_0) &= \frac{(\underline{x}_A(t_A) - \underline{x}_P(t_0))}{|(\underline{x}_A(t_A) - \underline{x}_P(t_0))|} \times \hat{z} \\ \hat{r}(t_0) &= \hat{z} \times \hat{n}\end{aligned}\tag{3.13}$$

This frame of reference is defined so that the r-component of  $x_B(t_B)$  is zero, while its z-component is negative. In addition, the r-component of  $x_A(t_A)$  is positive, as well as its z-component during the occultation. The reason behind the selection of this particular frame of reference is due to the fact that a ray signal which belongs to the z-r plane greatly simplify the analysis. So, in order for a particular ray to remain confined to this plane, the refractive environment at the target object P must be *spherically symmetric* as encountered by the ray. This requires that this frame is moving with the target object P. Obviously, introducing assumptions cause limitations on the model which will be addressed in the Subsection [3.4.6](#). Regarding the times,  $t_B$  is the one recorded at the ground station so is directly available; the transmitter and the receiver are solar system objects, which follow deterministic trajectories, so the transmission time  $t_A$  can be found from:

$$|x_A(t_A) - x_B(t_B)| = c(t_B - t_A)\tag{3.14}$$

Where  $c$  is the speed of light in vacuum.

Lastly, the time  $t_0$ : the occultation position  $x_0$  is not known a priori (it does not obey Newton's laws of motion), so the best way to determine  $t_0$  is to use an iterative procedure. The starting value is set as  $t_A = t_0$  (since it is assumed that the target object is closer to the transmitter A than to the receiver B). Then, the unrefracted ray straight line from the transmitter A at time  $t_A$  and the receiver B at time  $t_B$  is constructed. On this line, find the point at which the distance between the line and the target object P at time  $t_0$  is minimum. This point is called "pseudo-occultation point"; then find the travel time  $\Delta T$  between the transmitter A at time  $t_A$  and this pseudo occultation point. The new value of  $t_0$ , for the iterative procedure, will be set as  $t_A + \Delta T$ . Finally, repeat this procedure until acceptable convergence is achieved.

### 3.4.2 Relativistic and non-relativistic equations for frequency residuals

In this subsection the two formulas needed for obtaining the two unknowns, which are  $\delta_X$  and  $\beta_X$  (see Figure 3.23), will be presented. In particular, both the relativistic solution and the non-relativistic one have been analyzed, in order to study if the relativity effects, for a radio occultation experiments made on Venus and Mars, are important or insignificants. First of all, the relativistic version presented by Withers [24] is analyzed, see Equation 3.15 which represents the first of the two formula needed for solving the system (note that for the relativistic case, the 2x2 system will be a non-linear system, which will be solved through numerical integration routines; on the other hand, the non-relativistic case is characterized by a 2x2 linearized system, easier to be solved). In case there is no refraction at the target object P, the radio signal travels directly from the transmitter to the receiver, the initial and final straight line are equal and so the unit vectors  $\hat{n}_B(t_B)$  and  $\hat{n}_A(t_A)$ , which will be called  $\hat{n}_{B,Direct}(t_B)$  and  $\hat{n}_{A,Direct}(t_A)$  are equal. In this case, the received radio frequency is called  $f_{B,Direct}(t_B)$ . On the other hand, if refraction of the radio signal occurs at the target object, then these unit vectors are different and will be called "occultation unit vectors":  $\hat{n}_{B,Occ}(t_B)$ ,  $\hat{n}_{A,Occ}(t_A)$ . In this case the received frequency is called  $f_{B,Occ}(t_B)$ . The frequency residuals evaluated in the Subsection 3.3.7 represent the difference between  $f_{B,Occ}(t_B)$  and  $f_{B,Direct}(t_B)$  and are defined as  $\Delta f(t_B)$ .

$$\begin{aligned} \frac{\Delta f(t_B)}{f_A(t_A)} = & \left( \frac{1 - \frac{v_B(t_B) \cdot \hat{n}_{B,Occ}(t_B)}{c} - \frac{U_B(t_B)}{c^2} + \frac{v_B(t_B)^2}{2c^2}}{1 - \frac{v_A(t_A) \cdot \hat{n}_{A,Occ}(t_A)}{c} - \frac{U_A(t_A)}{c^2} + \frac{v_A(t_A)^2}{2c^2}} \right) \\ & - \left( \frac{1 - \frac{v_B(t_B) \cdot \hat{n}_{B,Direct}(t_B)}{c} - \frac{U_B(t_B)}{c^2} + \frac{v_B(t_B)^2}{2c^2}}{1 - \frac{v_A(t_A) \cdot \hat{n}_{A,Direct}(t_A)}{c} - \frac{U_A(t_A)}{c^2} + \frac{v_A(t_A)^2}{2c^2}} \right) \end{aligned} \quad (3.15)$$

In addition the frequency residual can be related to the refractive properties of the planet through the relativistic equation written above.

### 3.4.3 Geometric definitions

The Figure 3.23 permits to define the unit vectors of Equation 3.15 as a function of the occultation geometry.

Firstly, some angles are defined:

$$\tan \delta_B = \frac{(r_A(t_A) - r_B(t_B))}{(z_A(t_A) - z_B(t_B))} \quad (3.16)$$

The angle  $\beta_A$  is defined by:

$$\beta_A + \delta_B = 90^\circ \quad (3.17)$$

Note that the frame of reference definition requires that during the occultation  $0^\circ < \delta_B < 90^\circ$  and  $0^\circ < \beta_B < 90^\circ$ . So that,  $\cos \beta_A = \sin \delta_B$  and  $\sin \beta_A = \cos \delta_B$ .

The angle  $\delta_X$  is defined by:

$$\tan (\delta_B - \delta_X) = \frac{(r_X(t_0) - r_B(t_B))}{(z_X(t_0) - z_B(t_B))} \quad (3.18)$$

The angle  $\beta_X$  is defined by:

$$\tan (\beta_B - \beta_X) = \frac{(r_A(t_A) - r_X(t_0))}{(z_A(t_A) - z_X(t_0))} \quad (3.19)$$

Thanks to the equations defined above, is possible to relate the unit vectors to the geometry of the occultations:

$$\begin{aligned}
 -\hat{\underline{n}}_{B,Direct}(t_B) &= \hat{\underline{r}}(t_0) \sin \delta_B + \hat{\underline{z}}(t_0) \cos \delta_B \\
 -\hat{\underline{n}}_{B,Occ}(t_B) &= \hat{\underline{r}}(t_0) \sin(\delta_B - \delta_X) + \hat{\underline{z}}(t_0) \cos(\delta_B - \delta_X) \\
 -\hat{\underline{n}}_{A,Direct}(t_A) &= \hat{\underline{r}}(t_0) \cos \beta_A + \hat{\underline{z}}(t_0) \sin \beta_A \\
 -\hat{\underline{n}}_{A,Occ}(t_A) &= \hat{\underline{r}}(t_0) \cos(\beta_A - \beta_X) + \hat{\underline{z}}(t_0) \sin(\beta_A - \beta_X)
 \end{aligned} \tag{3.20}$$

By using the geometric definitions of Equation 3.20, then Equation 3.15 becomes:

$$\begin{aligned}
 \frac{\Delta f}{f_A} &= \left( \frac{1 + \frac{vr_B \sin(\delta_B - \delta_X) + vz_B \cos(\delta_B - \delta_X)}{c} - \frac{U_B}{c^2} + \frac{v_B^2}{2c^2}}{1 + \frac{vr_A \cos(\beta_A - \beta_X) + vz_A \sin(\beta_A - \beta_X)}{c} - \frac{U_A}{c^2} + \frac{v_A^2}{2c^2}} \right) \\
 &\quad - \left( \frac{1 + \frac{vr_B \sin \delta_B + vz_B \cos \delta_B}{c} - \frac{U_B}{c^2} + \frac{v_B^2}{2c^2}}{1 + \frac{vr_A \cos \beta_A + vz_A \sin \beta_A}{c} - \frac{U_A}{c^2} + \frac{v_A^2}{2c^2}} \right)
 \end{aligned} \tag{3.21}$$

Note that in Equation 3.21 the times references have been omitted, and in addition, other conventions have been defined:

$$\begin{aligned}
 \underline{v}_A(t_A) &= \dot{\underline{x}}_A(t_A) - \dot{\underline{x}}_P(t_0) \\
 \underline{v}_B(t_B) &= \dot{\underline{x}}_B(t_B) - \dot{\underline{x}}_P(t_0) \\
 vr_A(t_A) &= \underline{v}_A(t_A) \cdot \hat{\underline{r}}(t_0) \\
 &\quad \text{(which is the r-component of } \underline{v}_A(t_A))
 \end{aligned}$$

All the variables in this equation are known or can be obtained from the ephemeris of transmitter, receiver and target object, except for the two unknowns: the angles  $\beta_X$  and  $\delta_X$ . In order to obtain the two unknowns, a second formula is needed. The second one comes from the geometry of the occultation, in particular from the impact parameter  $a$ , which represents the closest approach distance between the ray asymptote and the center of mass of the target. Furthermore, since the refractivity around the target object is considered spherically symmetric, then the closest approach distances of the two asymptotes are identical and satisfy:

$$a(t_0) = -z_B(t_B) \sin(\delta_B - \delta_X) \quad (3.22)$$

$$a(t_0) = (r_A^2(t_A) + z_A^2(t_A))^{1/2} \sin(\beta_A - \beta_X - \gamma) \quad (3.23)$$

where  $\gamma$  is defined as:

$$\tan \gamma = \frac{z_A(t_A)}{r_A(t_A)} \quad (3.24)$$

So the second equation, valid to solve both the 2x2 relativistic and non-relativistic system, is obtained by combining the Equation [3.22](#) and Equation [3.23](#), which is:

$$-z_B(t_B) \sin(\delta_B - \delta_X) = (r_A^2(t_A) + z_A^2(t_A))^{1/2} \sin(\beta_A - \beta_X - \gamma) \quad (3.25)$$

Now, the Relativistic system of two equations in two unknowns can be solved. The solution provides the value of  $\beta_X$  and  $\delta_X$  for an individual radio ray. The values of  $\delta_X$  and  $\beta_X$  can be obtained as a function of time, by solving the 2x2 systems for each ray belonging to the time series recorded at the receiver. Thanks to the values of  $\delta_X$  and  $\beta_X$ , as functions of time obtained during the occultation, the total angle of refraction  $\alpha$ , as well as the impact parameter  $a$ , can be obtained as functions of time too:

$$\alpha = \beta_X + \delta_X \quad (3.26)$$

$$a(t_0) = (r_A^2(t_A) + z_A^2(t_A))^{1/2} \sin(\beta_A - \beta_X - \gamma) \quad (3.27)$$

The first goal of this method has been achieved, which was to find a series of bending angles function of the impact parameter. From these it will be possible to obtain the refractive index and the vertical profiles of atmospheric properties.

Before continuing in the process, the non-relativistic system adopted for obtaining the non-relativistic solution of the occultation problem is showed below, see Equation [3.28](#). As mentioned before, the second equation of the system (impact parameter, Equation [3.27](#)) is the same for both cases, while the frequency residuals equation for the non-relativistic equations is the one from [\[7\]](#). Then, as

explained before, the 2x2 system (for the non-relativistic case is linear) can be solved in order to obtain the two unknowns  $\delta_X$  and  $\beta_X$ , and then by using the same formula showed above the total bending angle  $\alpha$  and impact parameter  $a$  can be obtained.

$$\begin{aligned} \frac{\Delta f}{f_A} = & \left( 1 - \frac{vr_A \cos(\beta_A - \beta_X) - vz_A \sin(\beta_A - \beta_X)}{c} \right. \\ & \left. + \frac{vr_B \sin(\delta_B - \delta_X) + vz_B \cos(\delta_B - \delta_X)}{c} \right) \\ & - \left( 1 - \frac{vr_A \cos \beta_A - vz_A \sin \beta_A + vr_B \sin \delta_B + vz_B \cos \delta_B}{c} \right) \end{aligned} \quad (3.28)$$

#### 3.4.4 Abel transform

The series of bending angles function of the impact parameter can be used in order to retrieve the refractivity index  $\mu$ , as a function of the radial distance,  $R$  [7]. The tool which permits this conversion is the Abel transform, an integral relationship which relates the refractivity index, the impact parameter and the bending angle. The real closest approach distance (of the real refracted ray path between the transmitter and the receiver) is defined as  $|x_0(t_0) - x_P(t_0)|$  which is called here as  $R(t_0) = R_0$ . The value of  $\mu$  at  $R = R_0$ , through the Abel transform, satisfies:

$$\pi \ln \mu(R_0) = \int_{a=a_0}^{a=\infty} \ln \left\{ \frac{a}{a_0} + \left[ \left( \frac{a}{a_0} \right)^2 - 1 \right]^{1/2} \right\} \frac{d\alpha}{da} da \quad (3.29)$$

where  $a_0 = a(t_0)$ .

From the Abel transform, the refractivity index can be obtained. In addition, the Bouguer's rule permits to relate the radial distance  $R$  to the impact parameter  $a$  through the refractivity index  $\mu$ :

$$R_0 = \frac{a_0}{\mu(R_0)} \quad (3.30)$$

Then, by using the derived bending angles, impact parameters and by repeating this process for each  $R = R_0$  is possible to obtain the value of  $\mu$  at  $R = R_0$  for any  $R_0$ . This process yields the function  $\mu(r)$ . The propagation of a radio signal

through a medium is determined by the medium's complex refractive index. In particular, the real part controls the phase speed, while the imaginary part controls extinction. The interest of this work is to focus on the real part of the refractivity index, which variations are related to refraction and bending of the ray.

### 3.4.5 Atmospheric parameters

From the refractivity index, now is possible to define how to determine the others atmospheric parameters needed. First of all, is quite simple to obtain the refractivity,  $\nu$ , function of the radius  $r$ , too.

$$\nu = \mu - 1 \quad (3.31)$$

In particular the refractivity is defined as the sum of the refractivity of the ionosphere,  $\nu_e$  and the one of the neutral atmosphere,  $\nu_n$ :

$$\nu = \nu_e + \nu_n \quad (3.32)$$

The ionosphere has negative refractivity ( $\mu < 1$ ) while the neutral atmosphere has positive refractivity ( $\mu > 1$ ), so radio signals entering the ionosphere of a planet from vacuum are refracted in the opposite direction from radio signals entering a neutral atmosphere from vacuum [23]. Both  $\nu_e$  and  $\nu_n$  can be determined from a single measurement of  $\nu$  for most planetary atmospheres and radio frequencies. In fact, in the ionosphere neutral densities are low and electron densities are high, so  $\nu_e$  is relevant and  $\nu_n$  is small. On the other hand, at lower altitudes, within the neutral atmosphere, neutral densities are high and electron densities are low, so  $\nu_n$  is the one dominant. So, to summarize, from the practical point of view the analysis of a single-frequency radio occultation data are based on the following assumptions [23]:

- If the measured value of  $\nu$  is negative, it will be assumed that  $\nu_e = \nu$  and  $\nu_n = 0$ ;
- If the measured value of  $\nu$  is positive, it will be assumed that  $\nu_n = \nu$  and  $\nu_e = 0$ ;
- In the intermediate altitude region, above the detectable neutral atmosphere and below the detectable ionosphere, where  $\nu$  is experimentally indistinguish-

able from 0, it will be assumed  $\nu_n = \nu_e = 0$  (in reality the two refractivities are not actually zero, they have comparable but opposite values).

In case the radio occultation is made through multiple-frequencies, the above assumptions are not necessary since  $\nu_e$  depends on frequency while  $\nu_n$  does not. So, in that case will be easier to separate the two contributes.

Other atmospheric parameters which can be found are the neutral number density  $n(r)$  and electron number density  $N_e(r)$  both evaluated in [ $m^{-3}$ ].  $N_e(r)$  can be determined from  $\nu_e(r)$  using:

$$\mu_e - 1 = \nu_e = -\frac{N_e e^2}{8\pi^2 m_e \epsilon_0 f^2} \quad (3.33)$$

Where  $N_e$  is electron density,  $e$  is the elementary charge,  $m_e$  is the electron mass,  $\epsilon_0$  is the permittivity of free space and  $f$  is frequency. While the neutral number density can be obtained from:

$$\mu_n - 1 = \nu_n = \sum k_i n_{n,i} \quad (3.34)$$

Where  $k_i$  is the refractive volume of constituent  $i$  and  $n_{n,i}$  is the number density of constituent  $i$  [5]. Within this research, a mean refractive volume,  $k$ , have been defined (for Venus from S. Tellmann [21] ; while for Mars from D.P. Hinson [9]), which is based on the known chemical composition of the atmosphere such that:

$$\nu_n = k n_n \quad (3.35)$$

Where  $n_n$  is the total neutral number density; so  $n_n(r)$  can be found from  $\nu_n(r)$ .

The next atmospheric parameter is the mass density,  $\rho(r)$ , which can be retrieved from the formula:

$$\rho(r) = m \cdot n_n(r) \quad (3.36)$$

Where  $m$  is the mean molecular mass of the atmosphere in [kg/molecule].

Other parameters which can be now defined, and obtained, are the pressure and temperature. Starting from the pressure, it can be obtained from the density  $\rho(R)$  and the known gravitational field, by applying the hydrostatic equilibrium

equation, together with a boundary condition at the edge of the vertical profile analyzed. The assumption made in order to use the hydrostatic equilibrium equation is that the atmosphere is a *well-mixed atmosphere*, that is, one composed of air parcels all originating from a common, hypothetical reservoir, all with the same heat content. This assumption is valid both for Mars and Venus, but particularly for Venus, since its clouds experience the phenomenon of super-rotation, in which the atmosphere circles the planet in just four Earth days, much faster than the planet's sidereal day of 243 days.

The hydrostatic equilibrium equation can be written as:

$$\frac{dp}{dr} = \rho g_r \quad (3.37)$$

Where  $g$  is the gravitational acceleration,  $\rho$  is the density and  $dr$  represent the infinitesimal variation in the radial direction, or altitude.

The upper boundary condition is obtained from the scale height  $H$ , of the neutral number density,  $n_n(R)$ . It is assumed that the pressure at the edge is:

$$p(R_{edge}) = \rho \times g(R_{edge}) \times H \quad (3.38)$$

Where  $R_{edge}$  is the radial distance where the B.C is applied.

Then the pressure, function of the radial distance is:

$$p(r) = \rho(R_{edge})g(R_{edge}) \times \left( \frac{d}{dr} (\ln \rho) \Big|_{R_{edge}} \right)^{-1} + \int_{R_{edge}}^r \rho(r)g_r(r) dr \quad (3.39)$$

To conclude the atmospheric parameters, the temperature is obtained by applying the Ideal gas state law:

$$T = \frac{p \cdot m_{mmw}}{\rho \cdot k_B} \quad (3.40)$$

Where  $p$  is the pressure,  $\rho$  is density,  $k_B = 1.38064852 \times 10^{-23} m^2 K g s^{-2} K^{-1}$  is the Boltzmann constant and  $m_{mmw}$  is the mean molecular mass.

Note that errors in the upper boundary condition have minimal effect on the derived pressures, and so temperatures, at altitudes more than several scale heights

below the upper boundary [25].

### 3.4.6 Limitations

The method explained in this Section is valid for:

1. One-way link
2. Single frequency experiment
3. Stable frequency source of the transmitter (usage of USO at the transmitter is highly recommended, if possible)
4. The refractive environment at the target is spherically symmetric.
5. Frequency residuals already processed.
6. Well-mixed atmosphere for applying the hydrostatic equilibrium equation
7. Ideal gas behaviour of the neutral atmosphere

First of all, regarding the radio-link (1), in case the experiment is two-way, the radio signal propagates through the atmosphere and ionosphere twice, and the rays pass through different regions in the uplink and downlink. So, it is difficult to separate the refraction due to the neutral atmosphere between the uplink and downlink; however, the refraction due to the ionosphere is frequency dependent, so can be easily separated. Furthermore, the single-frequency hypothesis (2) is not a limitation on the method because the multi-frequency experiments permit to isolate ionospheric refraction and plasma noise. The important thing is that the method works with a single set of frequency residuals, so the residuals coming from the multi-frequencies must be processed and a single set of the corrected frequency residuals should be prepared before dealing with the method. In case the spacecraft has not a stable frequency (3), which usually is set by an Ultra stable oscillator, then a one-way experiment is not reliable. In fact, the frequency residuals are not precise so it is impossible to study the atmosphere of the planet. In this case, it is better to set the experiment in a two-way mode. If the spherical symmetry hypothesis (4) cannot be assumed, as for example in the oblate planets like Jupiter, Saturn, then gradients of refractivity will exist perpendicular to the  $r$ - $z$  plane of Figure 3.23, which contains the target, the transmitter and the receiver, thus the radio signal will travel outside this plane and this method is no more

valid. To conclude in order to evaluate the pressure and the temperature, the assumptions (6) and (7) have been considered.

### 3.5 Noise characterization

The radiometric measurements are affected by errors related to the presence of noises. The main classification of the noises is:

- Electronic instrumentation noise
- Media propagation noise

#### 3.5.1 Electronic instrumentation noise

This noise source is related to the characteristics of the instrument adopted. In the frame of this work, the main instrument affected by this noise is the Ultra Stable Oscillator (USO) of the transmitter. A first error comes from the Oscillator stability, which is given in terms of Allan deviation  $\sigma$  or “fractional frequency uncertainty”, i.e. residual frequency divided by transmitted frequency:

$$\sigma = \frac{\Delta f}{f} \quad (3.41)$$

For example, the Allan deviation for the USO of VEX is  $\sim 3 \cdot 10^{-13}$  over timescales of 1-100 seconds, and almost the same  $10^{-13}$  for MGS USO, too. The lower the value of the Allan deviation, the better it is for the radio occultation experiment, since it is reflected in a higher stability of the transmitted frequency.

Another noise source related to the electronic instrumentations is the thermal noise. Every electronic system, which works in a temperature condition different from the absolute zero (as for example the spacecraft transponder and its USO) generates a noise component due to the thermal agitation of the electrons in the conductor. Furthermore, this noise is ideally a white noise, while in statistics and in probability theory it can be represented as a normal distribution, or Gaussian amplitude distribution. Moreover, the presence of the thermal noise is directly linked to a finite value of the Signal to noise ratio, defined as the ratio between the Power of the signal and the power of the noise associated to it. Usually, the ground electronic equipment, which record the signals and send the uplinks, is working in

cryogenic conditions, resulting in a lower thermal noise. For this reason, the SNR at the receiver is always higher with respect to the SNR at the transmitter, which usually cannot adopt cryogenic systems due to the limitations in power, weight and complexity. For radiometric tracking, the error introduced by the Doppler thermal noise can be expressed in terms of Allan deviation as:

$$\sigma_v = \frac{c}{2f_c} \frac{\sqrt{2B_L}}{2\pi T_C \sqrt{P_C/N_0}} \quad (3.42)$$

Where  $\sigma_v$  is the Doppler thermal noise error, in [mm/s];  $B_L$  is the 1-sided loop bandwidth, in [Hz];  $T_C$  is the count time, in seconds;  $f_c$  is the carrier frequency, in [Hz];  $P_C/N_0$  is the carrier signal-to-noise spectral density ratio.

To conclude, for an open loop optimal processing, as the one adopted in this work,  $B_L$  is set as:

$$B_L = 1/(2T_C) \quad (3.43)$$

### 3.5.2 Plasma noise

The first of the media propagation noise analyzed, which lead to errors in the radiometric measurement, is the Plasma noise. This noise comes from the propagation of the radio signal in the solar plasma, which is a stream of charged particles released from the corona of the sun, its upper atmosphere. This plasma is mainly composed by electrons, protons and alpha particles. From the theoretical point of view, the delay in the propagation of the radio signal, due to its interaction with the solar plasma, could be evaluated through the TEC (Total Electron Count), which could be obtained with multifrequency experiments [19]. The best way to calibrate the plasma noise is by having a full multifrequency link calibration, which is a radio system which generates three different observables, as the one adopted by Cassini (X/X, Ka/Ka, X/Ka) [13]. However a full multifrequency link increase the complexity and the costs so that some methods have been developed, which are capable to calibrate most of the plasma noise even when the radio link is made only by a dual-frequency link [13]. Within this research only single frequency experiments were available, so that there has not been the possibility to evaluate and calibrate the plasma noise. However, a useful parameter, called Sun-Earth-

spacecraft (SEP) angle, see Figure [3.24](#), permits to understand the influence of the errors due to the plasma noise on the radiometric measurement. If the SEP is small (worst case is  $SEP=0^\circ$ ), then the radiometric signal is propagating into the region of the solar wind, so a high value of the plasma noise, and its Allan deviation on the measurement is expected. On the other hand, if the value of the SEP increase (best case  $SEP=180\text{deg}$ ), then the plasma noise and its Allan deviation decrease. The Figure [3.25](#) shows the relation of the Allan deviation for the plasma noise with respect to the SEP for one-way link, as well as the contribute of the earth's troposphere, which will be analyzed in the next subsection.

### 3.5.3 Earth's troposphere and ionosphere

Radio waves travelling in the Earth's atmosphere of the Earth are delayed due to electromagnetic refraction. So, as a consequence, this delay depends on the length of the path, thus on the incident elevation angle of the radio wave with respect to the receiver. The delay caused by the Earth atmosphere is separated in the two main components: the one due to the troposphere and the one caused by the ionosphere.

#### Troposphere

The troposphere is the lowest layer of the Earth's atmosphere. This is also the layer where all the weather conditions take place. The average height of the troposphere is 18 km in the tropics, 17 km in the middle latitudes, and 6 km in the polar regions in winter. In this region the pressure, as well as the temperature, are maximum at sea level and they decrease with the height, this because in this layer the hydrostatic equilibrium assumption is valid, so that the pressure is equal to the weight of air above a given point. For the temperature, by using the ideal gas state law, one can obtain it through the pressure. The tropospheric delay  $N$  can be studied as the sum of two components:

$$N = N_{dry} + N_{wet}$$

The wet delay is caused by the permanent dipole in atmospheric water vapor, while the dry delay is caused by induced dipoles in all atmospheric gasses [4]. Within this work, the troposphere delay has been calibrated by using the atmosphere information provided by the NASA-JPL. The troposphere is considered azimuthally symmetric so that the azimuthal delay, provided by the JPL, has been corrected with a mapping function which takes into account the slant-range correction to the spacecraft elevation, see Figure 3.26. If the elevation angle is small, then the radio signal travels more time in the troposphere and the delay will be higher. To conclude, the tropospheric delays are general and do not depend on a particular spacecraft. The details on how to calibrate the tropospheric delay are provided in the Section 4.4.

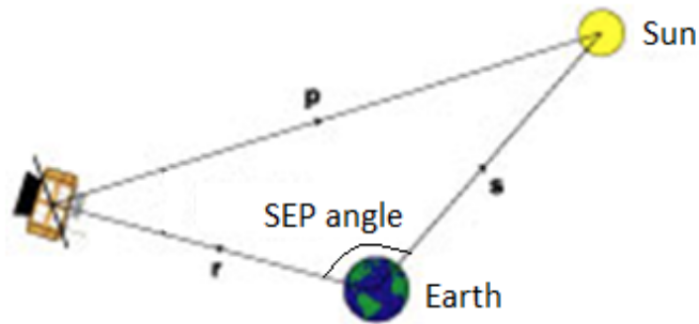


Figure 3.24: SEP angle definition. [15]

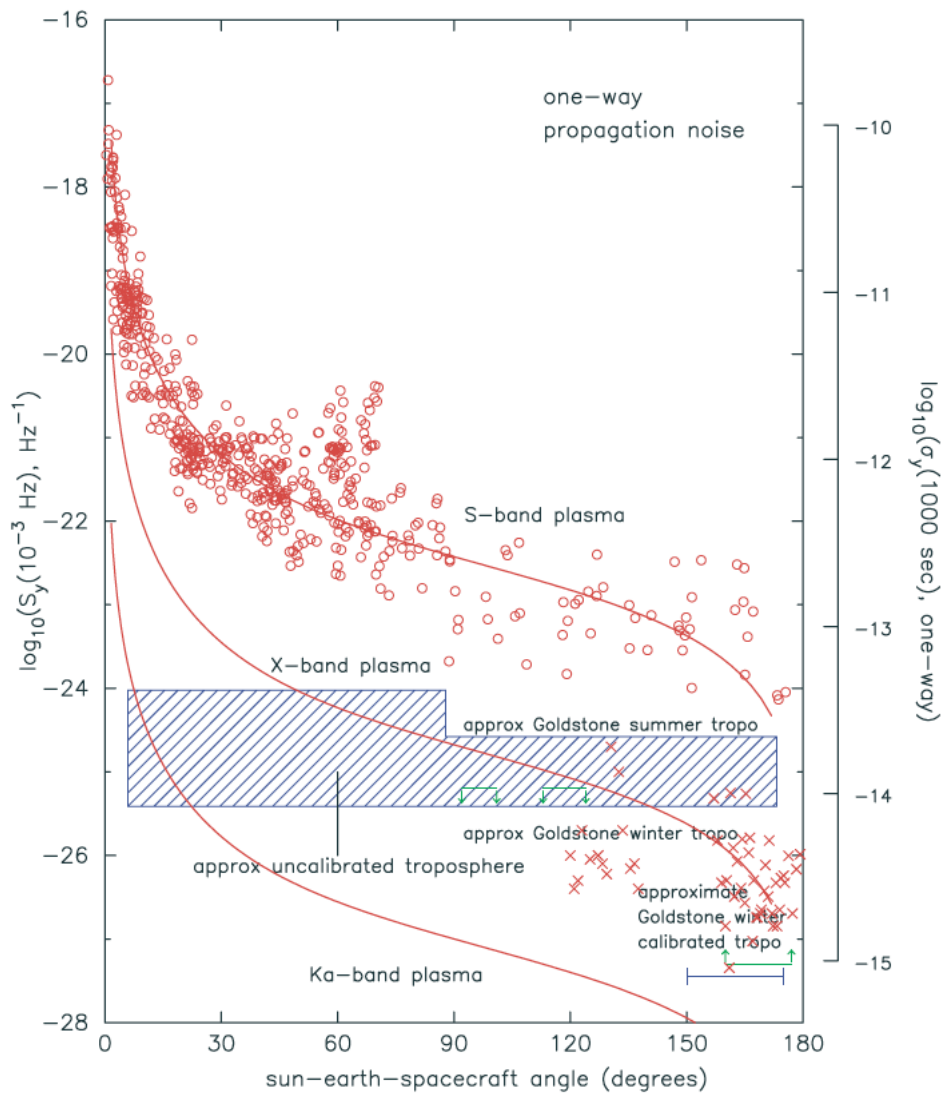


Figure 3.25: Trend of the power spectral density of plasma noise and troposphere noise with respect to the SEP angle. [1]

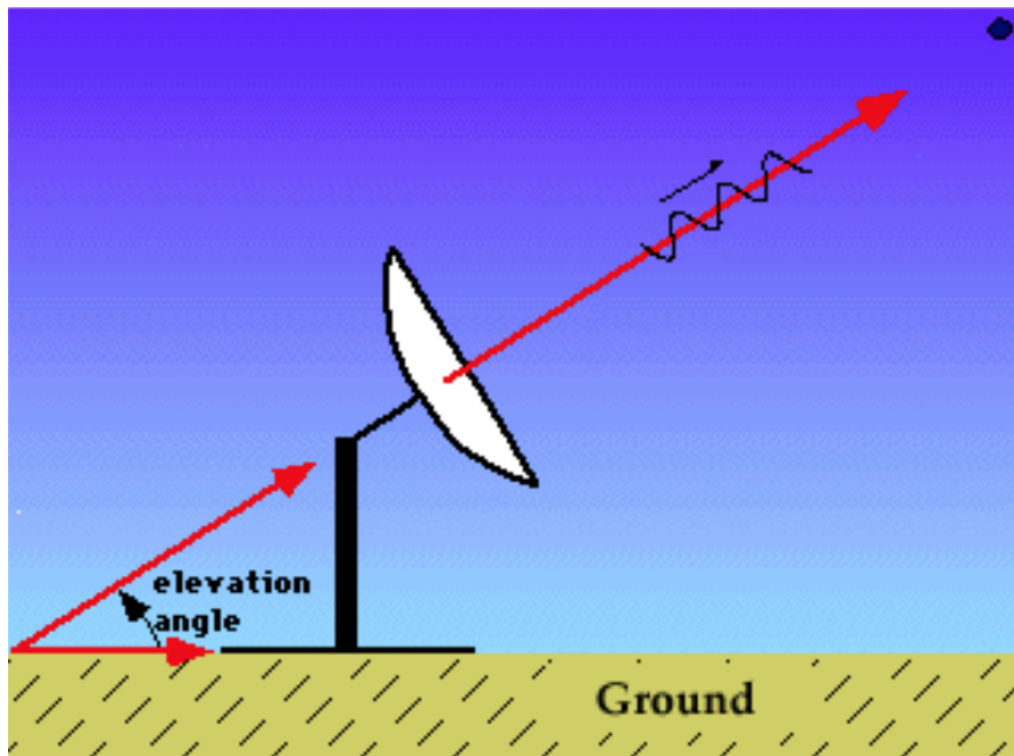
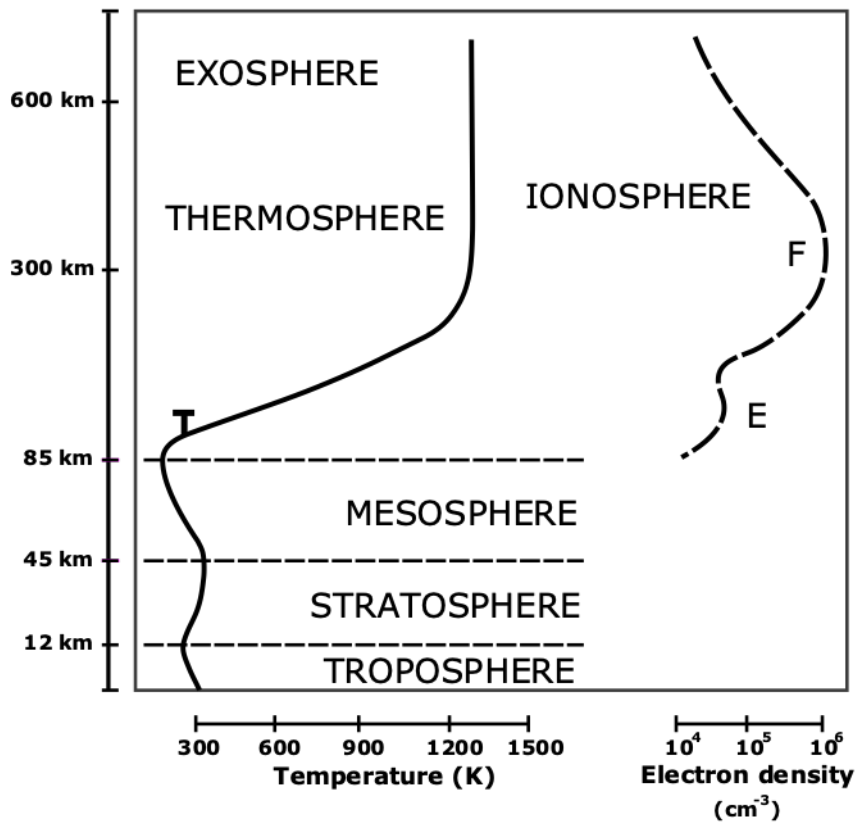


Figure 3.26: Elevation angle. [15]

## Ionosphere

The ionosphere is the upper part of Earth's atmosphere, at altitudes between the 60 km to 1000 km, and is ionized by solar radiation, see Figure 3.27. The ionosphere, as well as the troposphere, cause a delay on the radiometric measurement due to the refraction of the charged particles. One main difference between the ionosphere and the troposphere is that the distribution of the charged particles in the ionosphere is highly inhomogeneous. This means that the magnitude of the ionosphere range delay, at a certain position, depends on the spacecraft line of sight, the observing frequency, time of the day, season and solar cycle. As for the troposphere, the details on how the ionosphere delays have been calibrated are given in Section 4.4.



**Figure 3.27:** Earth's atmosphere layers.

Credit: <https://en.wikipedia.org/wiki/Ionosphere>



## Chapter 4

# Venus and Mars atmosphere algorithm

The algorithm has been developed in a MATLAB environment, following the guidelines presented in Section 3.3 by Withers [24], and it has been adapted both for Venus and Mars. The algorithm takes as inputs the reconstructed frequency residuals and gives as outputs the vertical profiles of electron density, bending angle, impact parameter, refractivity, neutral density, temperature and pressure for a planetary body. Its fundamental assumption is the spherical symmetry of the atmosphere around the target. In this Chapter the first Section is dedicated to an overview of the structure of the algorithm, focusing the attention on the key points to obtain a successful radio science occultation experiment. In addition, the algorithm has been validated by comparing the results obtained with the ones in the literature, a comparison of these results is shown in Section 4.2. Section 4.3 will show a comparison of two different solutions, which are evaluated within the algorithm: the relativistic one, which takes into account the relativity effects during the radio science experiment, and the non-relativistic one, which simplify the computation without taking into account the relativity effects on the radio signal. Section 4.4 will provide details on the time-step selection for the radio science investigations adopted within this investigation, showing which are the parameters involved and how they change, depending on the time-step chosen. The last section is dedicated to the calibrations of the reconstructed frequency residuals, which include the Earth's troposphere and ionosphere, spacecraft clock and trajectory calibrations, needed in order to correct the residuals before being analyzed

by the algorithm.

## 4.1 Algorithm's structure overview

The algorithm starts with the evaluation of the receiver time  $t_B$ , the transmitter time  $t_A$ , and the closest approach time  $t_0$ . The accuracies of the time evaluations, as well the positions and velocities of the objects, are crucial to the success of the experiment. The receiver time  $t_B$ , is the one recorded at the ground stations, so it is already available within the reconstructed frequency residuals, which include the reception time for each residual evaluated, as seconds past midnight. However, the SPICE functions used for the following computations require the ephemeris time, defined as seconds past J2000 epoch, which is noon January 1, 2000. So, as a first step, the received times have been transformed from seconds past midnight to the ephemeris times, thanks to a SPICE function. After that, the received time  $t_B$  can be used in order to determine the transmitted time from the spacecraft, thanks to one SPICE function which is able to evaluate the light time between the transmitter and the receiver given their positions, so that:

$$t_A = t_B - LT \tag{4.1}$$

where  $LT$  is the light time.

The last time to be evaluated is  $t_0$ , the closest approach time, which is evaluated through an iterative procedure as explained in the section 3.3. After the evaluation of the times, is then possible to obtain all the positions and velocities of the transmitter, receiver and target at their respective times  $t_A$ ,  $t_B$  and  $t_0$ . In particular the positions, velocities and the frame of reference must be evaluated for each frequency residual analyzed, so that the geometrical problem (i.e. the angles and relative positions of Figure [3.23](#)) of the occultation can be analyzed for each time-step. The next important step is the computation of the two geometrical unknowns  $\delta_X$  and  $\beta_X$ , which will permit to obtain the impact parameter  $a$  and the total bending angle  $\alpha$ . These two unknowns can be evaluated in two different ways: the first one is by using a 2x2 non-linear system made with the relativistic frequency residuals Equation [3.21](#) and the impact parameter Equation [3.25](#). The non-linear system is solved through the Broyden's numerical method, which returns the two unknowns. The second solution, easier to be found, is characterized by a 2x2

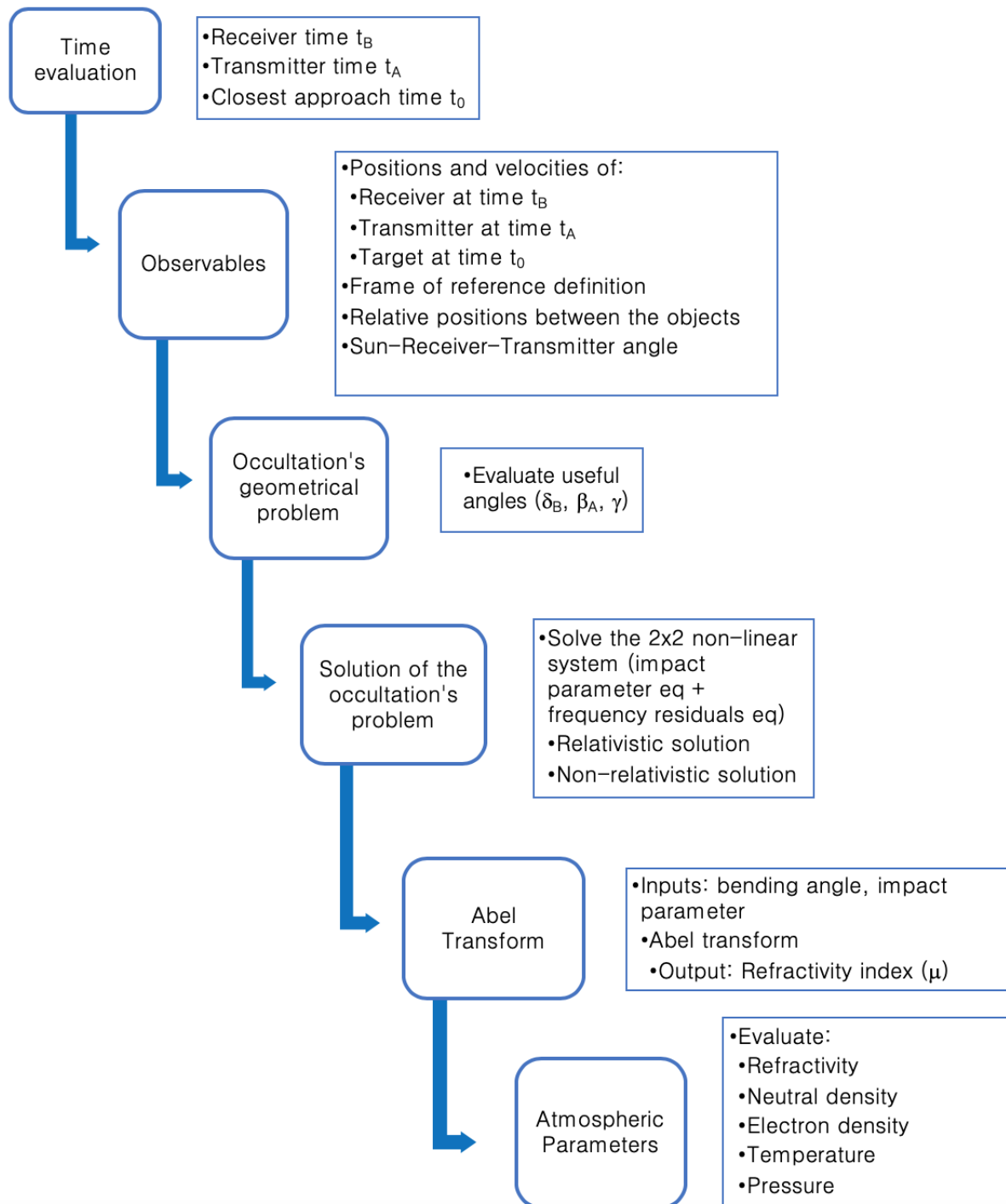


Figure 4.1: MATLAB algorithm structure overview.

linearized system, with a non-relativistic frequency residuals Equation 3.28 and the same impact parameter Equation 3.25. The non-relativistic equation, reported in the Subsection 3.4.3 can be directly found from Equation 3.21 if relativistic terms  $U/c^2$  or  $(v/c)^2$  and higher can be neglected, or from the Appendix A of [7].

Then, this linearized system is solved within the algorithm as presented by [7]: basically, the values of the unknowns  $\delta_X$  and  $\beta_X$ , are replaced by  $\delta_X + \Delta\delta_X$  and  $\beta_X + \Delta\beta_X$  and the transcendental equations are linearized with regard to  $\Delta\delta_X$  and  $\Delta\beta_X$ . The new problem to be solved becomes:

$$b_{11}\Delta\beta_X + b_{12}\Delta\delta_X = k_1, \quad (4.2)$$

$$b_{21}\Delta\beta_X + b_{22}\Delta\delta_X = k_2, \quad (4.3)$$

where

$$b_{11} = -vr_A \sin(\beta_A - \beta_X) + vz_A \cos(\beta_A - \beta_X),$$

$$b_{12} = -vr_B \cos(\delta_B - \delta_X) + vz_B \sin(\delta_B - \delta_X),$$

$$b_{21} = (r_A^2 + z_A^2)^{1/2} \cos(\beta_A - \gamma - \beta_X),$$

$$b_{22} = z_A \cos(\delta_B - \delta_X),$$

$$\begin{aligned} k_1 = c \frac{\Delta f}{f} + vr_A [\cos(\beta_A - \beta_X) - \cos \beta_A] \\ + vz_A [\sin(\beta_A - \beta_X) - \sin \beta_A] \\ - vr_B [\sin(\delta_B - \delta_X) - \sin \delta_B] \\ - vz_B [\cos(\delta_B - \delta_X) - \cos(\delta_B)] \end{aligned} \quad (4.4)$$

$$k_2 = z_B \sin(\delta_B - \delta_X) + (r_A^2 + z_A^2)^{1/2} \sin(\beta_A - \gamma - \beta_X) \quad (4.5)$$

The new set of equations is used to find the non-relativistic solutions  $(\delta_X, \beta_X)$  of the occultation experiment, as a function of time. The best approach to solve this problem is to start analyzing the radio signals travelling outside the atmosphere, where both  $\delta_X$  and  $\beta_X$  are zero, and then moves to rays at lower altitudes. Each ray is solved by making an initial estimate of  $\delta_X$  and  $\beta_X$ , which comes from the

rays at higher altitudes, and the linearized problem will provide the corrections  $\Delta\delta_X$  and  $\Delta\beta_X$  needed. Then, the new values of  $\delta_X$  and  $\beta_X$  are fed back into the linearized system and the new corrections are evaluated, as an iterative procedure, until the desired precision is obtained. Thanks to the solutions it is then possible to obtain the impact parameter  $a$  (Equation 3.27) and the total bending angle  $\alpha$  (Equation 3.26). Furthermore, in order to obtain the atmospheric parameters, the algorithm takes as input the solution of the 2x2 system solved (depending on which solution would like to be analyzed by the user) and the Abel transform, implemented in the algorithm, converts the impact parameter and the bending angles into the refractivity index of the atmosphere around the target. The last step is to evaluate all the atmospheric parameters with the formula presented in the Subsection 3.3.5. As discussed before, the temperature and pressure are obtained by imposing a boundary condition at the edge of the vertical profile analyzed. Two different methods have been studied within this research, the first one is the one presented by Withers [24], already showed in the Chapter 3; the second one was presented by S. Tellmann [21], which consists in imposing, as a boundary condition, a temperature  $T_{up}$  at the edge of the profile at  $h = h_{up}$ , then the vertical profile of the temperature is retrieved thanks to the Equation 4.6:

$$T(h) = \frac{\mu_{up}}{\mu(h)} \cdot T_{up} + \frac{\bar{m}}{k \cdot n(h)} \int_h^{h_{up}} n(h') \cdot g(h') dh' \quad (4.6)$$

Finally, the pressure can be computed through the ideal gas state law, Equation 4.7:

$$p = \rho T \frac{k_B}{m_{mmw}} \quad (4.7)$$

From the algorithm point of view, one of the main differences between Venus and Mars, is that for Venus is more difficult to find the numerical solution of the non-linear system of the occultation problem. This is due to the thick and dense atmosphere effect, which is translated in stronger fluctuations in the frequency residuals, which in turn are not as good as the ones from Mars. However, as will be explained in Section 4.5, the difference between the relativistic and non-relativistic solution is negligible, so that this did not represent a great problem within this work. The results of the two methods outlined will be shown in Section 4.2, while the differences between the relativistic and non-relativistic solutions is provided in

Section [4.5](#).

## 4.2 Validation of the algorithm

The algorithm has been validated by comparing the profiles obtained with the ones present in literature, in particular for three different occultation experiments:

- MGS occultation 8361M48A [\[24\]](#)
- VEX ESA DOY 234 egress [\[17\]](#)
- VEX ESA DOY 200 ingress [\[17\]](#)

Within the next subsections are showed the results of the profiles obtained through the algorithm developed in this work, and the comparison with the profiles present in the papers of Withers and Pätzold.

### 4.2.1 MGS 8361M48A ingress occultation

Here are presented the results of the MATLAB algorithm (left plots) with respect to the results presented by Withers (2014) [\[24\]](#) (right plots), regarding the occultation experiment 8361M48A performed by Mars Global Surveyor at the target Mars. The frequency residuals needed for this occultation are available within the paper of Withers (2014) [\[24\]](#).

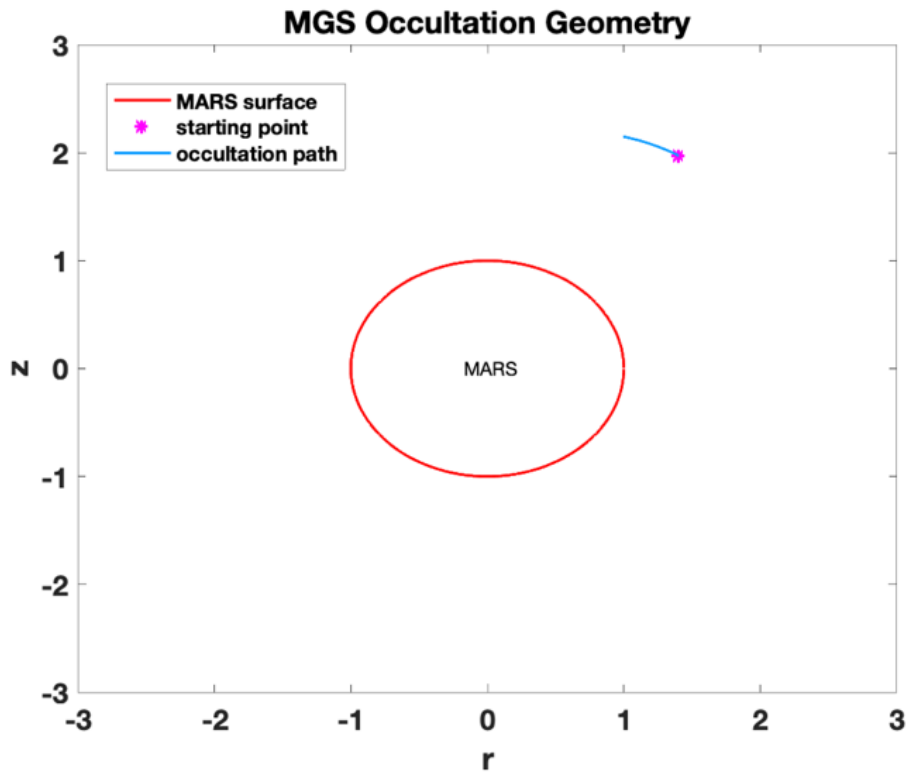
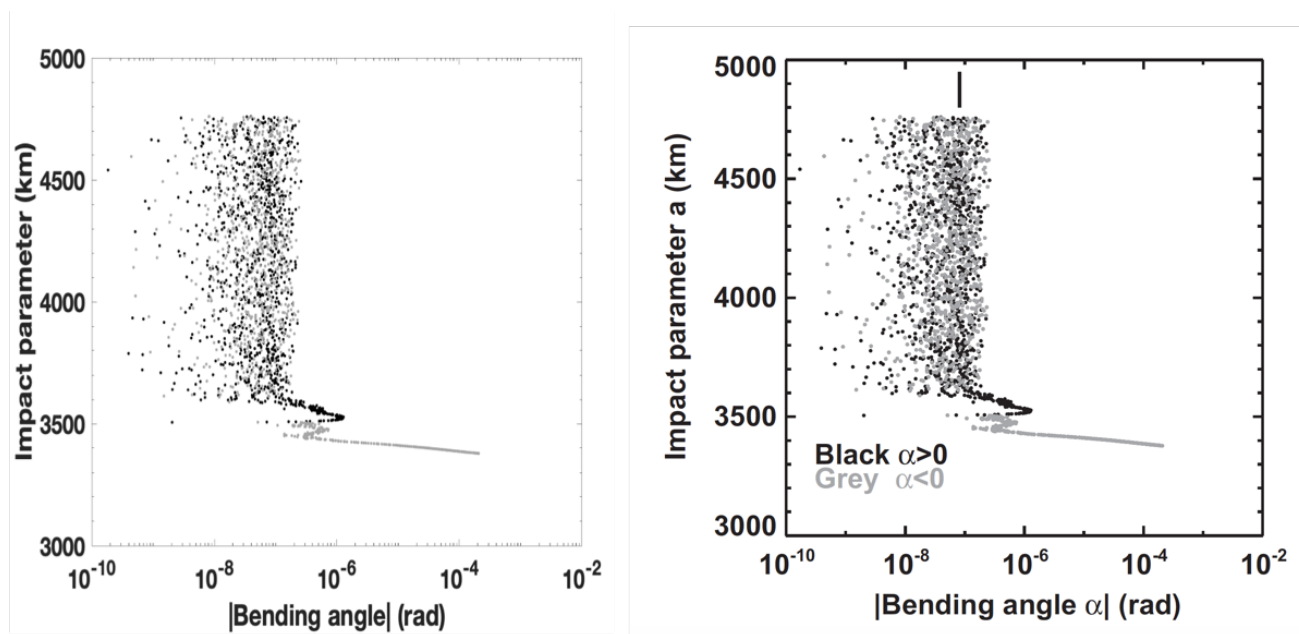
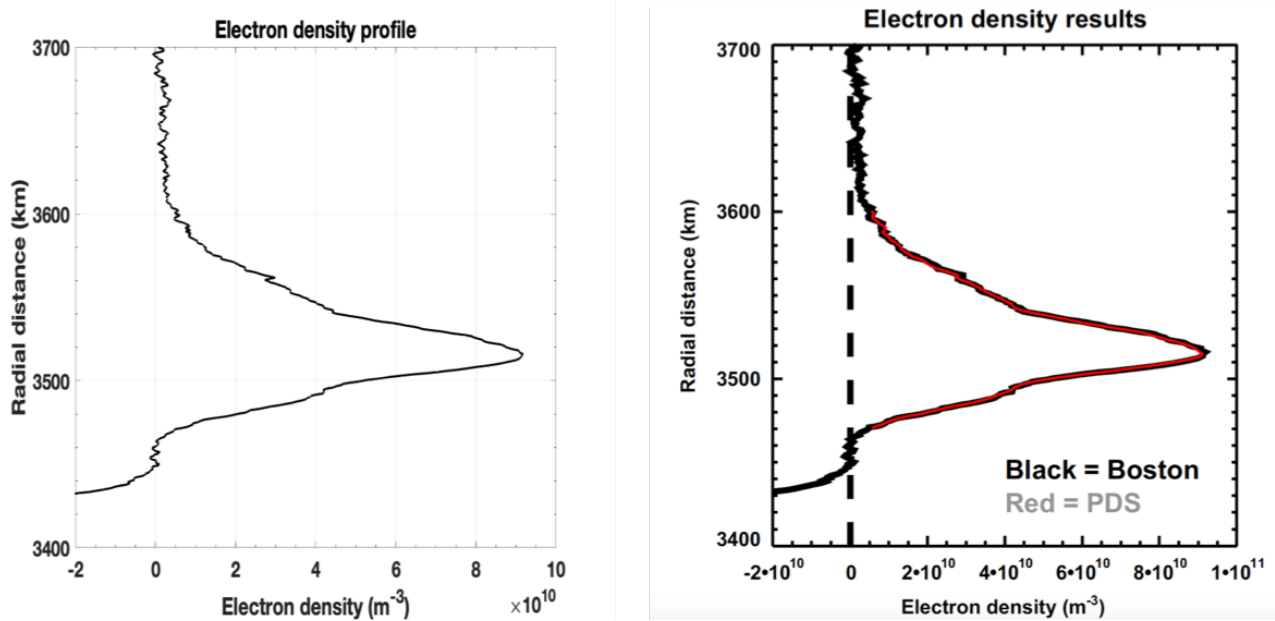


Figure 4.2: MGS 8361M48A Ingress occultation geometry.



**Figure 4.3:** Comparison of bending angles vs impact parameters between MATLAB algorithm (left) and Withers (2014) (right), for the MGS 8361M48A occultation.



**Figure 4.4:** Comparison of the electron density between MATLAB algorithm (left) and Withers (2014) (right), for the MGS 8361M48A occultation.

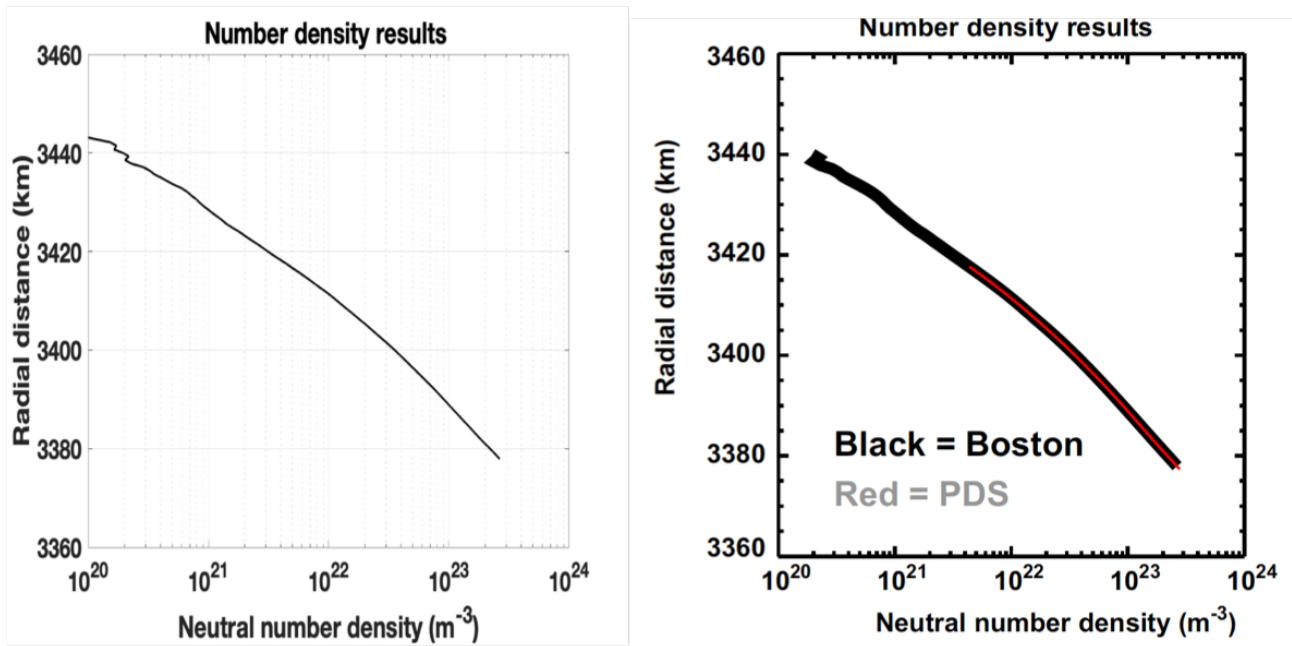


**Figure 4.5:** Comparison of the neutral number density between MATLAB algorithm (left) and Withers (2014) (right), for the MGS 8361M48A occultation.

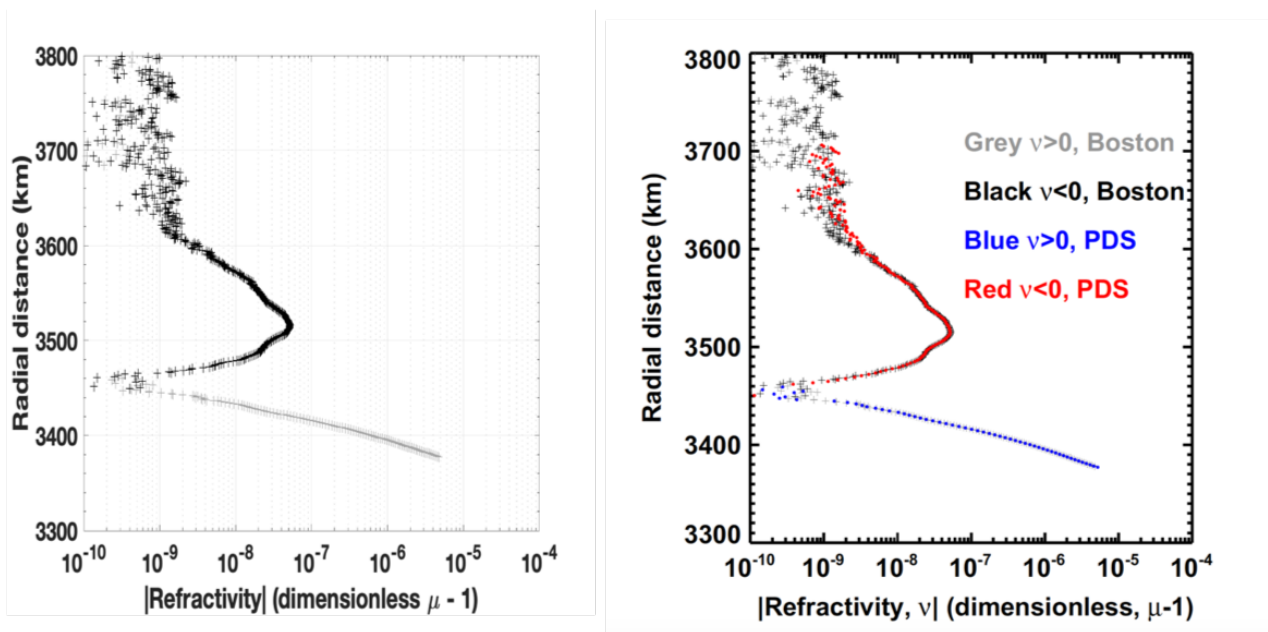


**Figure 4.6:** Comparison of the refractivity between MATLAB algorithm (left) and Withers (2014) (right), for the MGS 8361M48A occultation.

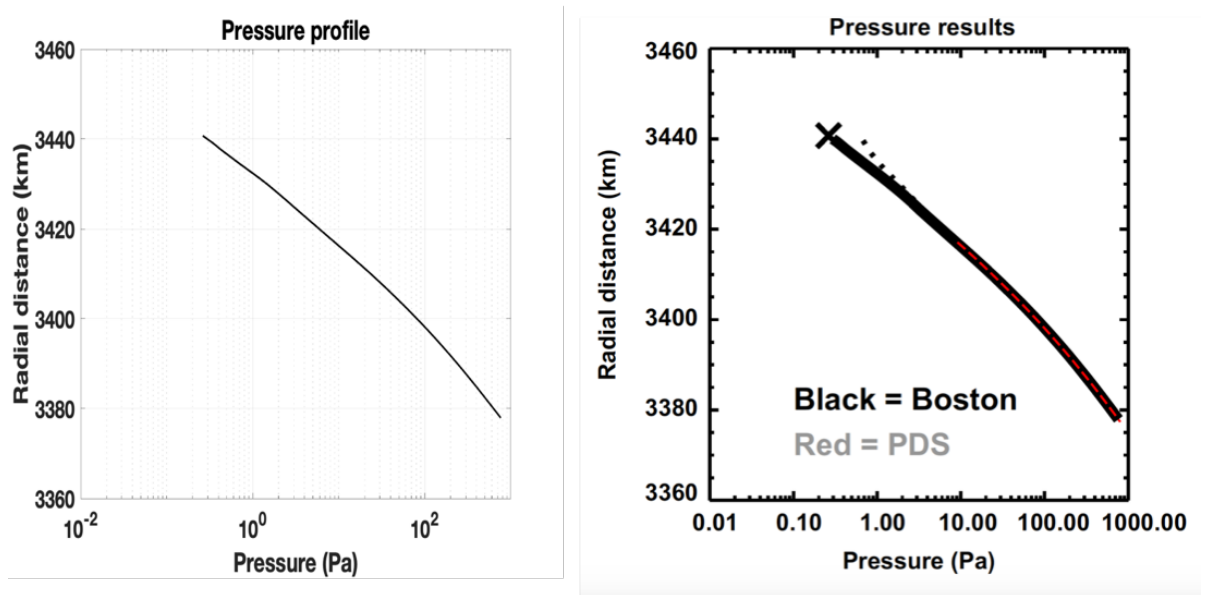


**Figure 4.7:** Comparison of the pressure profile between MATLAB algorithm (left) and Withers (2014) (right), for the MGS 8361M48A occultation.

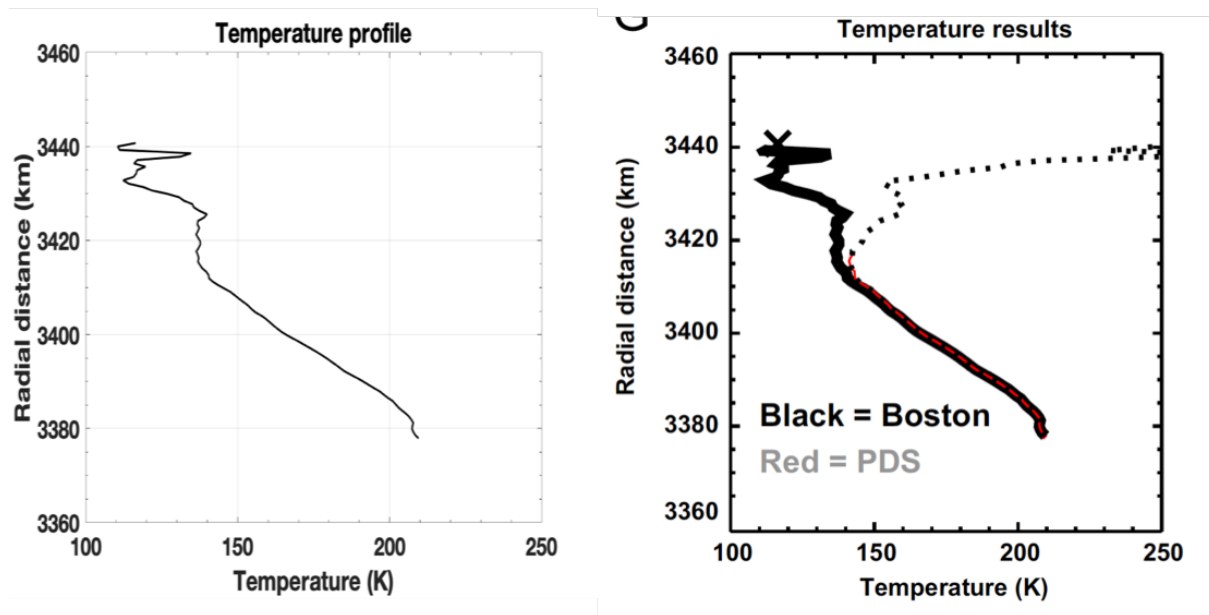


**Figure 4.8:** Comparison of the temperature profile between MATLAB algorithm (left) and Withers (2014) (right), for the MGS 8361M48A occultation.

By comparing the results of the MATLAB algorithm with the ones presented by

Withers (2014) [24], for this particular occultation, it has been found a very good matching in the profiles obtained, as showed in the figures above. In particular as a reference, the temperature values have been compared, and they showed differences lower than 0.05 K.

#### 4.2.2 VEX ESA DOY 234-2006 egress occultation

Another comparison has been made with respect to the results presented by Pätzold (2007) [17], regarding the egress occultation performed by Venus Express at Venus on the 22<sup>nd</sup> August 2006, with the data collected by the European Space Agency at the New Norcia ground station. In the left are present the plots of the MATLAB algorithm, while on the right are showed the results from the paper of M. Pätzold [17]. The frequency residuals for this occultation has been found from the European Space Agency's Planetary Science Archive (PSA).

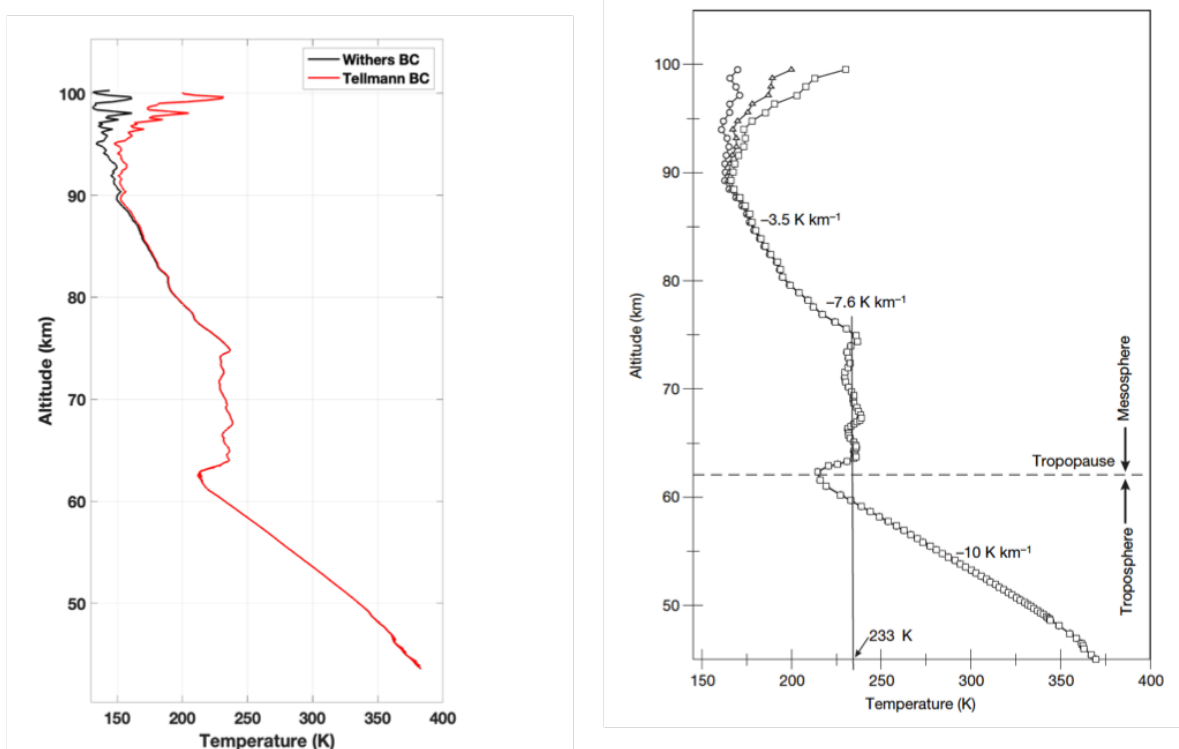


**Figure 4.9:** Comparison of temperature profiles between MATLAB algorithm (left, with different boundary condition methods) and Pätzold (2007) result (right), for the VEX 234-2006 occultation.

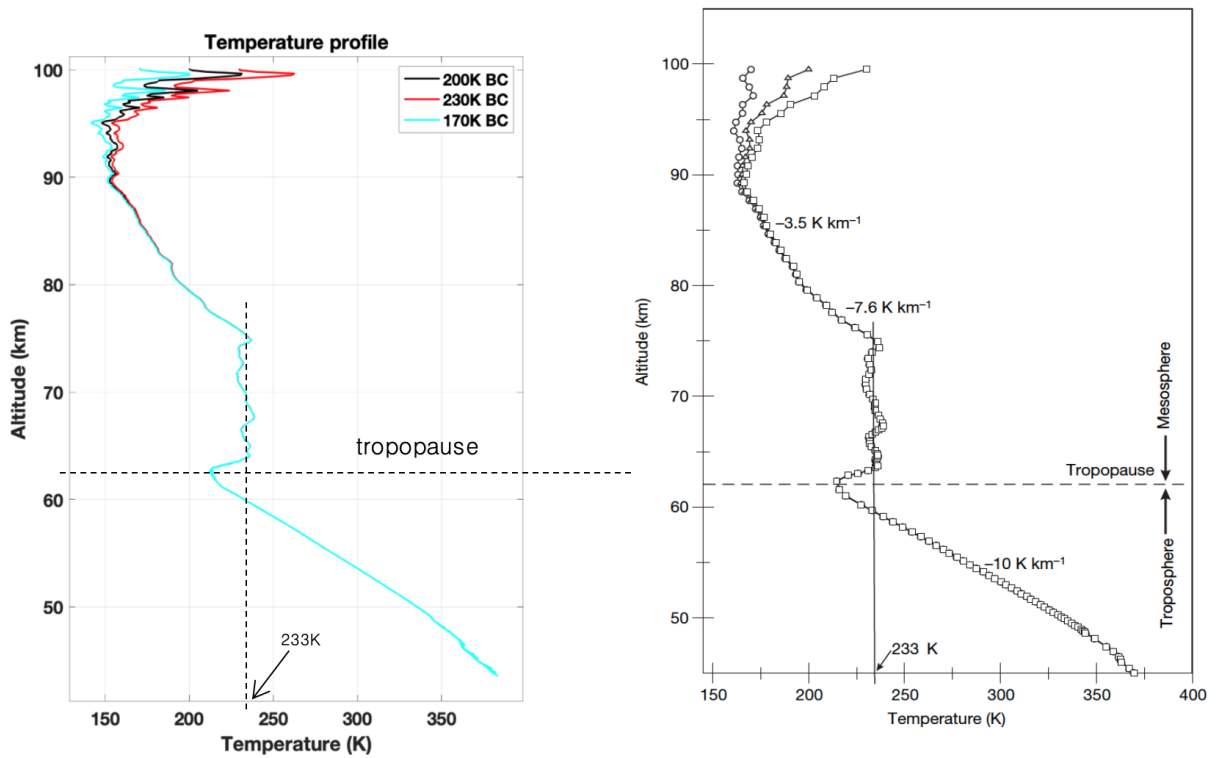


**Figure 4.10:** Comparison of temperature profiles between MATLAB algorithm (left, with three different starting B.C) and Pätzold (2007) result (right), for the VEX 234-2006 occultation.

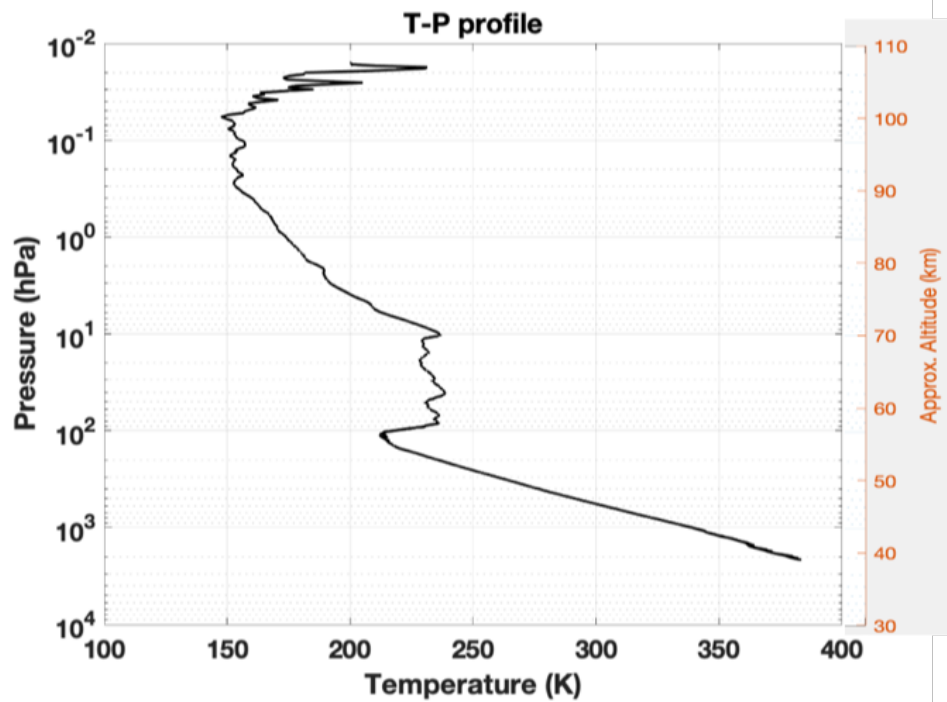


**Figure 4.11:** Temperature-pressure profile obtained for the VEX 234-2006 occultation.

As an additional validation, the algorithm has been compared with the results of another target, Venus. Also for this experiment, the MATLAB algorithm shows results which reproduce what presented by Pätzold (2007) [17]. In particular, the tropopause altitude, as well as the average temperature above the tropopause (233K) match accurately what presented in the paper. Within this experiment, it has been shown also the differences between the Withers boundary condition method and the Tellmann boundary condition method (as discussed in Section 4.1) see Figure 4.9. It can be seen that even if starting in a different way, they converge at the same value at around 85km altitude. This confirms what presented in several radio occultations investigations: the selection of the boundary condition does not influence the results at around one scale height below the edge of the profile analyzed. Furthermore, another study has been made, focusing the results on the Tellmann boundary condition method, since it was the one used by Pätzold (2007) [17], see Figure 4.10. In this figure, the same results presented by Pätzold (2007) has been reproduced, with three different starting boundary conditions, fixed at 170K, 200K and 230K. Here, again, is possible to show how the three temperature profiles converge, confirming what presented in the paper with high accuracy.

### 4.2.3 VEX ESA DOY 200-2006 ingress occultation

The third comparison presented is the one related to the occultation performed by Venus Express at Venus on the 19<sup>th</sup> July 2006, and studied by Pätzold (2007) too [17]. As a third comparison an ingress has been selected, so that the algorithm has been validated both for ingress and egress occultations, increasing the reliability of the algorithm itself.

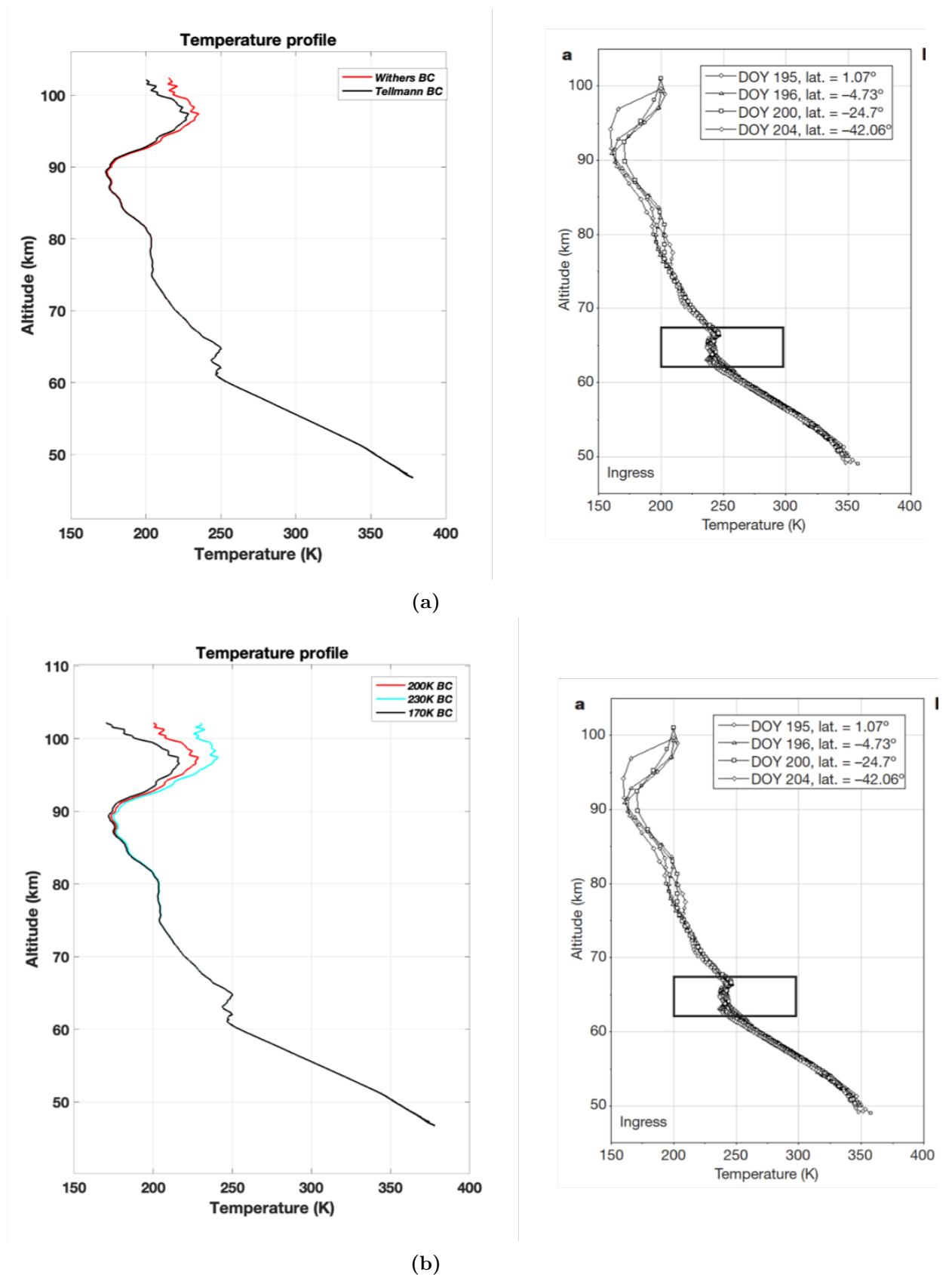


**Figure 4.12:** Comparison of temperature profiles between MATLAB algorithm (left) and Pätzold (2007) (right) for the VEX DOY 200-2006 occultation **a)** Different B.C methods; **b)** Three different B.C, Tellmann [21] method.

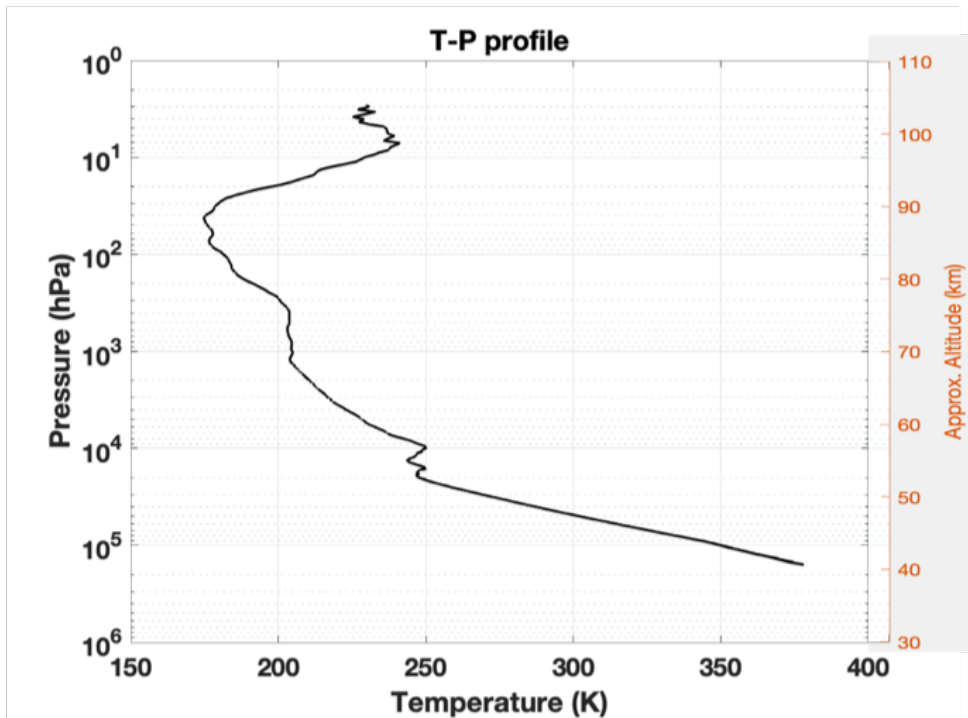


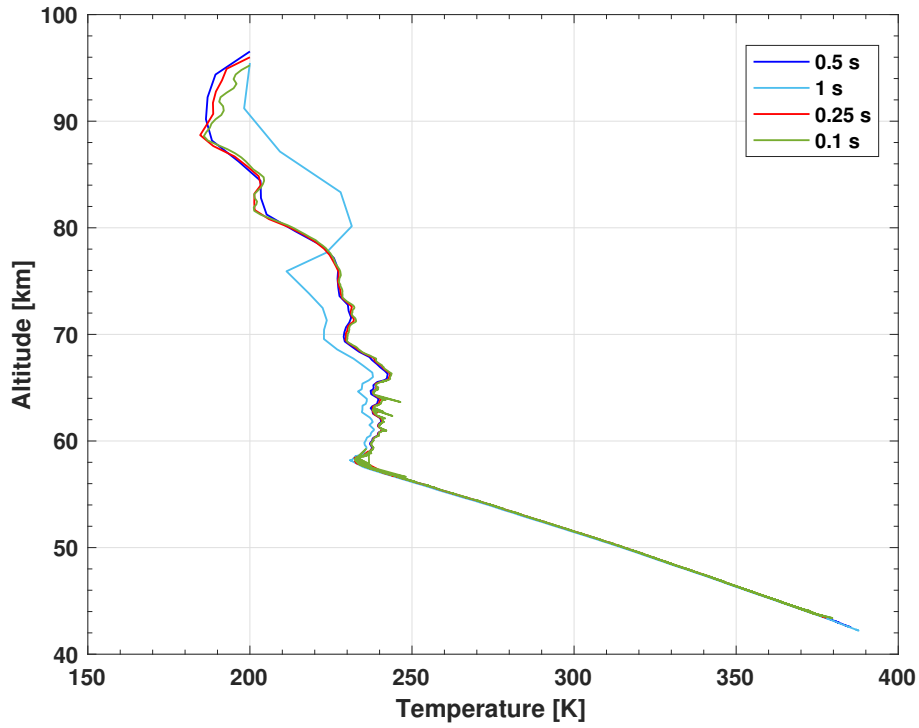
**Figure 4.13:** Temperature-pressure profile obtained for the VEX DOY 200-2006 occultation.

As for the previous validations, in these investigations the algorithm reproduced in a good way the results showed by Pätzold (2007) [17].

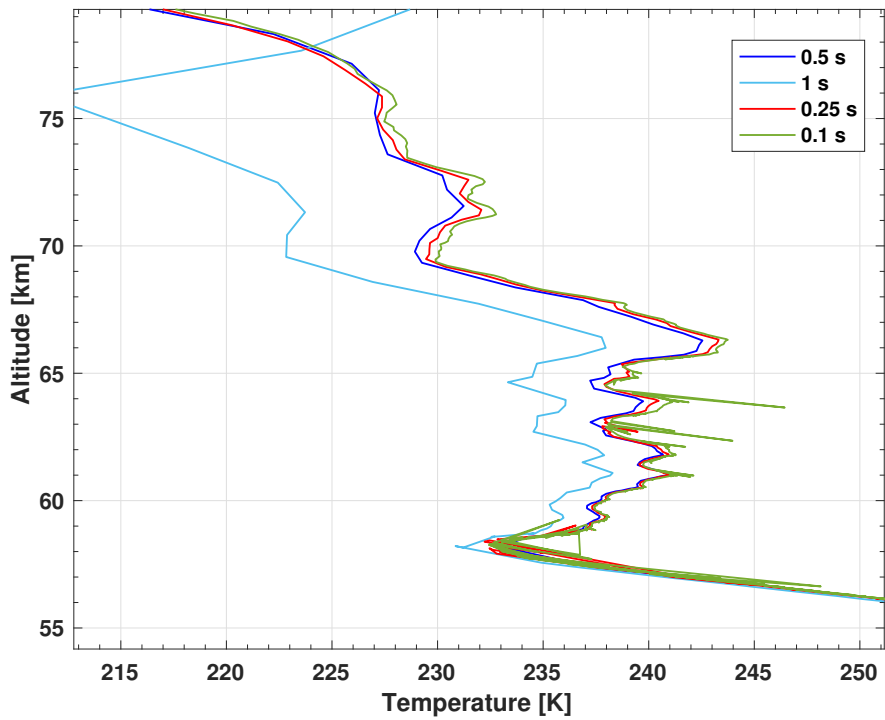
### 4.3 Integration time selection

The integration time selection took into account a trade off between the thermal noise and the number of points in the vertical profiles analyzed. In Figure 4.14 are reported the profiles obtained for four different integration times. The desire of decreasing the integration time to get a higher amount of points, and so a more detailed vertical profile, is affected by an increase in the thermal noise, which is due to the random agitation of the electrons. The thermal noise increases because the random agitation of the electrons is averaged in a shorter amount of time, resulting in higher noise for a lower time-step. This lead to errors in the computations of the frequency residuals, the so called outliers, as can be seen in the 0.1 seconds solution of Figure 4.14. The desire to deal with a higher amount of points is particularly true for Venus. In fact, a time-step of *1 second* generates frequency

residuals with strong variations between two time steps, leading to more difficult evaluations and numerical integrations for the algorithm. That is why a time-step of *0.25 seconds* has been adopted for Venus, which represents a good trade-off between a smoother frequency residuals variation (so easier to be computed) and the thermal noise. Regarding Mars, the frequency residuals have lower variations if compared to Venus (please note that the Venus frequency residuals can reach values between 0 and 10000Hz, while the ones for Mars only between 0 and 1-2 Hz), so a time-step of *0.5 seconds* has been adopted.



(a)



(b)

Figure 4.14: a) Temperature profiles for different integration times ; b) closer look

## 4.4 Calibration of the reconstructed frequency residuals

The reconstructed frequency residuals, before being analyzed through the atmosphere algorithm, must be calibrated. In fact, the recorded signal is always affected by some errors (as explained in Section 3.5 these errors come from the different type of noise present in a radiometric tracking) which should be corrected.

- Plasma noise
- Earth's troposphere noise
- Earth's ionosphere noise
- Thermal noise
- Spacecraft clock
- Errors in the trajectory of the spacecraft

### 4.4.1 Plasma noise

First of all, one error which affects the reconstructed frequency residuals, comes from the plasma noise, which is related to the interplanetary medium present in the path travelled by the radio signal between the transmitter and receiver. However, as already mentioned in the Subection 3.5.2, this error cannot be calibrated within this work, since the occultation data available are only single-frequency, while in order to calibrate the plasma noise a multi-frequency experiment is required. So, the plasma noise has been neglected, but the Sun-Earth-Spacecraft angle has been evaluated and the Figure 4.15 analyzed, in order to document the influence which the plasma noise has on the experiment.

### 4.4.2 Earth's troposphere and ionosphere

Furthermore, other two sources of errors, considered and calibrated within this research, are the ones due to the Earth's troposphere and ionosphere, which both cause a delay (in meters) in the range and Doppler of the spacecraft and so ultimately, in the frequency of the signal recorded. In practice this delay is translated in the phase delay of the recorded signal and then converted as a frequency shift.

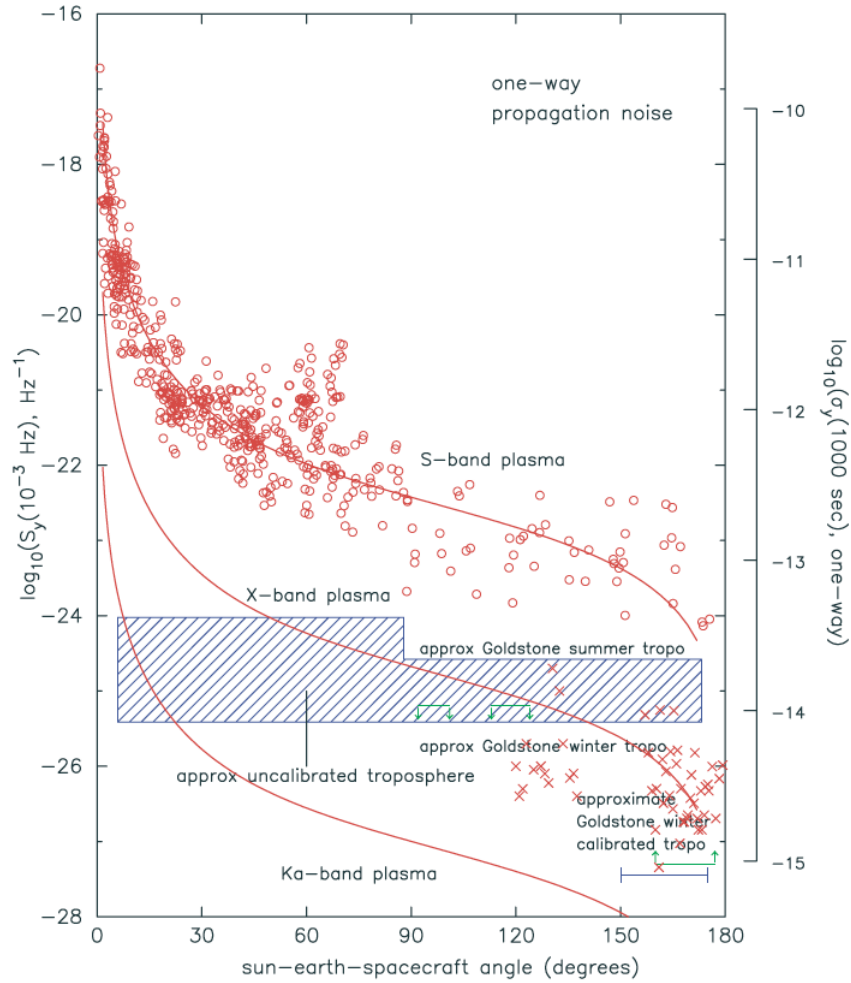
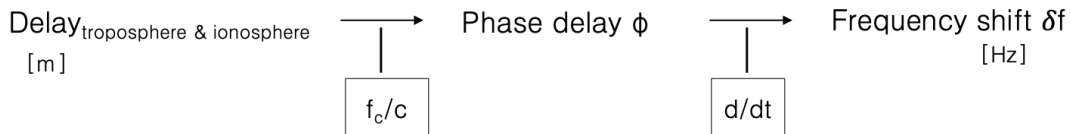


**Figure 4.15:** Trend of the power spectral density of plasma noise and troposphere noise with respect to the SEP angle. [1]



The troposphere delay is characterized by two main contributes: the *seasonal* one and the *daily* one. In particular, the seasonal effect permits to obtain a first order evaluation of the delay, by considering the troposphere average delay obtained through the past years. On the other hand, the daily effect corrects the first order evaluation made by the seasonal delay, in order to get higher calibration accuracies.

In this evaluation, the troposphere is considered azimuthally symmetric, and a mapping function is used in order to perform the slant-range correction to the spacecraft elevation. Both the *seasonal* and *daily* contributes are characterized by two main components: the wet component and the dry component (as explained in Section 3.5), see Equation 4.8.

$$Delay_{troposphere} = (Z_{wet\_daily} + Z_{dry\_daily} + Z_{const\_seasonal} + Z_{wet\_seasonal} + Z_{dry\_seasonal}) \cdot M \quad (4.8)$$

where  $M = 1/\sin(Elevation)$ .

In the Equation 4.8, first of all  $Z_{const\_seasonal}$  is a term which accounts for the particular DSS used. In fact, the seasonal models are evaluated with respect to the reference altitude of the 70-m antenna (DSS-43), so when using other antennas adjustments for the dry components are required (see Figure 4.17). Furthermore, M is the slant-range factor which is used in order to perform the slant range correction due to the spacecraft elevation, also called mapping function. This influence the delay of the troposphere, as well as the ionosphere one, since a low elevation radiometric tracking is characterized by a signal which propagates for more time in the Earth atmosphere. Thus, this means that the troposphere and ionosphere effect on the signal is higher, resulting in a higher delay. As a matter of fact, the slant-range factor is always  $\geq 1$ . The troposphere seasonal components of Equation 4.8 have been evaluated through Fourier series in the form (P, A0, A1, B1, A2, B2, ..., AN, BN), see Figure 4.16. So the tropospheric seasonal calibration at time T can be described as:

$$Z_{seasonal} = A_0 + A_1 \cos X + B_1 \sin X + A_2 \cos 2X + B_2 \sin 2X \dots + A_N \cos NX \quad (4.9)$$

Where T is replaced by  $X = 2\pi \cdot (T - S) / P$  and P is the period of the fundamental mode, in seconds.

On the other hand, the daily models (Figure 4.18) are evaluated through the Equation 4.10, so the tropospheric daily correction at time T can be evaluated as:

$$Z_{daily} = C_0 + C_1 \cdot X + C_2 \cdot X^2 + \dots + C_N \cdot X^N \quad (4.10)$$

Where  $T$  is replaced by the normalized (dimensionless) argument:

$$X = 2 \cdot ((T - S) / (E - S)) - 1.$$

```
ADJUST(ALL) DSN(C40) MODEL(WET NUPART) FROM(72/01/01) BY
TRIG(31557600., 0.1149, 0.0255, 0.0020, 0.0010, 0.0026, 0.0036,
-0.0001, 0.0007, 0.0012).
ADJUST(ALL) DSN(C40) MODEL(DRY NUPART) FROM(72/01/01) BY
TRIG(31557600., 2.1579, -0.0032, -0.0002, 0.0012, 0.0017, -0.0043,
0.0052, 0.0016, -0.0021).
```

**Figure 4.16:** Troposphere seasonal model for calibration.

```
ADJUST(ALL) DSN(033) MODEL(DRY NUPART) BY CONST( 0.0012204).
ADJUST(ALL) DSN(034) MODEL(DRY NUPART) BY CONST(-0.0008071).
ADJUST(ALL) DSN(042) MODEL(DRY NUPART) BY CONST( 0.0036483).
ADJUST(ALL) DSN(043) MODEL(DRY NUPART) BY CONST( 0.0000000).
ADJUST(ALL) DSN(045) MODEL(DRY NUPART) BY CONST( 0.0037169).
ADJUST(ALL) DSN(046) MODEL(DRY NUPART) BY CONST( 0.0030858).
ADJUST(ALL) DSN(049) MODEL(DRY NUPART) BY CONST( 0.0701534).
```

**Figure 4.17:** Earth's troposphere dry seasonal constant term, which adjusts for the particular DSS used.

```
# FITSIG= 0.0007 FLG=01
ADJUST(ALL)BY NRMPow(.0082,-.0165, .0151, .0269,-.0268,-.0213, .0181, .0046,
-.0038)MODEL(WET NUPART)FROM(14/03/01,03:00:00.001)TO(14/03/01,09:00)DSN(C10). #
2017/01/30,20:31:38
# FITSIG= 0.0005 FLG=01
ADJUST(ALL)BY NRMPow(-.0243, .0013,-.0011, .0028, .0002,-.0012)
MODEL(DRY NUPART)FROM(14/03/01,03:00:00.001)TO(14/03/01,09:00)DSN(C10). #
2017/01/30,20:31:38
```

**Figure 4.18:** Earth's troposphere daily model.

Regarding the ionosphere delay, it is evaluated daily and depends on the particular spacecraft line of sight, the observing frequency, solar cycle and time of the day, so the ionospheric delay is not general as the tropospheric one. The

ionospheric delay was provided in S-band so a correction for the X-band of VEX experiments has been required.

The component of the ionospheric delay, have been evaluated through normalized power series, which coefficients has been made available from the Jet Propulsion Laboratory. Given the coefficients ( $C_0, C_1, \dots, C_N$ ) see Figure 4.19, the calibration at time  $T$  is evaluated as:

$$Iono_{calibration} = C_0 + C_1 \cdot X + C_2 \cdot X^2 + \dots + C_N \cdot X^N \quad (4.11)$$

Where  $T$  is replaced by the normalized (dimensionless) argument:

$$X = 2 \cdot ((T - S) / (E - S)) - 1.$$

$E$ = end time of the calibration polynomial,  $S$ =start time of the calibration polynomial; the value is -1 at  $T=S$  and +1 at  $T=E$ . [4]

```
# FITSIG= 0.0406 FLG=01
ADJUST(DOPRNG)BY NRMPow(5.5531, 3.3256,-4.3600,-1.7334, 17.2068,
22.5308,
-19.8714,-31.4257, 8.8289, 13.0372)MODEL(CHPART)
FROM(14/03/01,05:23:00)TO(14/03/01,13:38)DSN(C60)SCID(248). #S01 ADJ
2014/03/14,15:34:39
```

**Figure 4.19:** Earth's troposphere daily model for calibration.

After evaluating the troposphere delay and the ionosphere delay, these contributes have been translated firstly in a phase shift and then in a frequency shift. The Figure 4.20 summarize a numerical computation for the Earth's troposphere and ionosphere frequency shifts evaluated for the occultation VEX DOY 066 2014.

1	2	3	4	5	6	7	8
inputtime	wet_tropo	wet_tropo_el	dry_tropo	dry_tropo_el	tropo_el_tot	iono_comp_xband	
9.9001e+03	0.1924	0.2965	2.1490	3.3110	3.6074	1.4096	
9.9004e+03	0.1924	0.2965	2.1490	3.3110	3.6075	1.4097	
9.9006e+03	0.1924	0.2965	2.1490	3.3111	3.6076	1.4097	
9.9009e+03	0.1924	0.2965	2.1490	3.3111	3.6076	1.4097	
9.9011e+03	0.1924	0.2965	2.1490	3.3112	3.6077	1.4097	
9.9014e+03	0.1924	0.2965	2.1490	3.3112	3.6077	1.4097	
9.9016e+03	0.1924	0.2965	2.1490	3.3113	3.6078	1.4097	
9.9019e+03	0.1924	0.2965	2.1490	3.3114	3.6079	1.4098	
9.9021e+03	0.1924	0.2965	2.1490	3.3114	3.6079	1.4098	
9.9024e+03	0.1924	0.2965	2.1490	3.3115	3.6080	1.4098	
9.9026e+03	0.1924	0.2965	2.1490	3.3115	3.6081	1.4098	
9.9029e+03	0.1924	0.2965	2.1490	3.3116	3.6081	1.4098	
9.9031e+03	0.1924	0.2965	2.1490	3.3116	3.6082	1.4099	
9.9034e+03	0.1924	0.2966	2.1490	3.3117	3.6083	1.4099	
9.9036e+03	0.1924	0.2966	2.1490	3.3118	3.6083	1.4099	
9.9039e+03	0.1924	0.2966	2.1490	3.3118	3.6084	1.4099	
9.9041e+03	0.1924	0.2966	2.1490	3.3119	3.6084	1.4099	
9.9044e+03	0.1924	0.2966	2.1490	3.3119	3.6085	1.4100	
9.9046e+03	0.1924	0.2966	2.1490	3.3120	3.6086	1.4100	
9.9049e+03	0.1924	0.2966	2.1490	3.3120	3.6086	1.4100	
9.9051e+03	0.1924	0.2966	2.1490	3.3121	3.6087	1.4100	
9.9054e+03	0.1924	0.2966	2.1490	3.3122	3.6088	1.4100	
9.9056e+03	0.1924	0.2966	2.1490	3.3122	3.6088	1.4100	
9.9059e+03	0.1924	0.2966	2.1490	3.3123	3.6089	1.4101	
9.9061e+03	0.1924	0.2966	2.1490	3.3123	3.6089	1.4101	
9.9064e+03	0.1924	0.2966	2.1490	3.3124	3.6090	1.4101	
9.9066e+03	0.1924	0.2966	2.1490	3.3124	3.6091	1.4101	
9.9069e+03	0.1924	0.2966	2.1490	3.3125	3.6091	1.4101	
9.9071e+03	0.1924	0.2966	2.1490	3.3126	3.6092	1.4102	
9.9074e+03	0.1924	0.2966	2.1490	3.3126	3.6093	1.4102	
9.9076e+03	0.1924	0.2967	2.1490	3.3127	3.6093	1.4102	
9.9079e+03	0.1925	0.2967	2.1490	3.3127	3.6094	1.4102	
9.9081e+03	0.1925	0.2967	2.1490	3.3128	3.6094	1.4102	
9.9084e+03	0.1925	0.2967	2.1490	3.3128	3.6095	1.4103	

**Figure 4.20:** Earth’s troposphere and ionosphere calibrations for one VEX-JPL occultation.

The Figure [4.20](#) is characterized by:

- *Inputtime* of the frequency residuals (in ephemeris time) [s];
- *wet\_tropo* is the sum of the seasonal and daily tropospheric wet delays, [m];
- *wet\_tropo\_el* is the sum of the seasonal and daily tropospheric wet delays, corrected for the elevation of the spacecraft with the mapping function M, [m];
- *dry\_tropo* is the sum of the seasonal and daily tropospheric dry delays, [m];

- *dry\_tropo\_el* is the sum of the seasonal and daily tropospheric wet delays, corrected for the elevation of the spacecraft with the mapping function M, [m];
- *tropo\_el\_tot* considers the whole tropospheric delay, [m];
- *iono\_comp\_xband* considers the ionospheric delay, for the X-band of VEX.

Please note that the ionospheric coefficients of Figure 4.19 are related to the S-band frequency, so a correction for the X-band (used in this work), has been performed. The delays presented in Figure 4.20 are in meters, then they have been transformed in frequency shifts [Hz], see Figure 4.21.

	1	2	3	4	5
	inputtime	phase_delay_tropo	freq_delay_tropo	phase_delay_iono	freq_delay_iono
1	9.9001e+03	101.3085	0.0018	39.5873	5.2088e-04
2	9.9004e+03	101.3103	0.0018	39.5878	5.2089e-04
3	9.9006e+03	101.3121	0.0018	39.5883	5.2089e-04
4	9.9009e+03	101.3138	0.0018	39.5888	5.2090e-04
5	9.9011e+03	101.3156	0.0018	39.5893	5.2091e-04
6	9.9014e+03	101.3174	0.0018	39.5899	5.2092e-04
7	9.9016e+03	101.3192	0.0018	39.5904	5.2093e-04
8	9.9019e+03	101.3209	0.0018	39.5909	5.2093e-04
9	9.9021e+03	101.3227	0.0018	39.5914	5.2094e-04
10	9.9024e+03	101.3245	0.0018	39.5919	5.2095e-04
11	9.9026e+03	101.3262	0.0018	39.5925	5.2096e-04
12	9.9029e+03	101.3280	0.0018	39.5930	5.2097e-04
13	9.9031e+03	101.3298	0.0018	39.5935	5.2097e-04
14	9.9034e+03	101.3315	0.0018	39.5940	5.2098e-04
15	9.9036e+03	101.3333	0.0018	39.5945	5.2099e-04
16	9.9039e+03	101.3351	0.0018	39.5951	5.2100e-04
17	9.9041e+03	101.3368	0.0018	39.5956	5.2101e-04
18	9.9044e+03	101.3386	0.0018	39.5961	5.2101e-04
19	9.9046e+03	101.3404	0.0018	39.5966	5.2102e-04
20	9.9049e+03	101.3421	0.0018	39.5971	5.2103e-04
21	9.9051e+03	101.3439	0.0018	39.5977	5.2104e-04
22	9.9054e+03	101.3457	0.0018	39.5982	5.2104e-04
23	9.9056e+03	101.3475	0.0018	39.5987	5.2105e-04
24	9.9059e+03	101.3492	0.0018	39.5992	5.2106e-04
25	9.9061e+03	101.3510	0.0018	39.5998	5.2107e-04
26	9.9064e+03	101.3528	0.0018	39.6003	5.2108e-04
27	9.9066e+03	101.3545	0.0018	39.6008	5.2108e-04
28	9.9069e+03	101.3563	0.0018	39.6013	5.2109e-04
29	9.9071e+03	101.3581	0.0018	39.6018	5.2110e-04
30	9.9074e+03	101.3598	0.0018	39.6024	5.2111e-04
31	9.9076e+03	101.3616	0.0018	39.6029	5.2112e-04
32	9.9079e+03	101.3634	0.0018	39.6034	5.2112e-04
33	9.9081e+03	101.3651	0.0018	39.6039	5.2113e-04
34	9.9084e+03	101.3669	0.0018	39.6044	5.2114e-04
35	9.9086e+03	101.3687	0.0018	39.6050	5.2115e-04

**Figure 4.21:** Earth's troposphere and ionosphere frequency shifts [Hz] for the VEX-JPL DOY 066 Ingress occultation.

### Sign of Calibration

Positive troposphere and ionosphere calibrations indicate positive range delays. So, the Doppler observables (i.e. the reconstructed frequency residuals) have been corrected by subtracting troposphere calibrations while adding ionosphere calibrations, due to the charged particles in the ionosphere which advance the Doppler phase.

### 4.4.3 Thermal noise, spacecraft clock and trajectory estimation

Other sources of errors come from the thermal noise, the spacecraft clock and the trajectory estimation. Even if the spacecraft is equipped with an Ultra Stable Oscillator, which generates a stable reference frequency, since the transmitter is not at the absolute zero temperature, there will be always some thermal noise which cause a small, but measurable, difference in the reference frequency generated. In addition, the USO is also affected by its clock's drift, aging and bias [3] and is usually corrected with a first or second order polynomial. The thermal noise, together with the spacecraft clock, cause a variation in the reference frequency sent by the spacecraft, which generates errors in the reconstructed frequency residuals. This is reflected in a baseline (the region of the frequency residuals outside the atmosphere) not fitted properly around a zero mean value, which in the end will led to a wrong evaluation of the atmosphere's parameters of the target. In addition to these effects, there is also a contribute of the trajectory estimation of the spacecraft, which introduce additional errors in the frequency residuals. The trajectory estimation errors have been dominant especially in the Ingress cases of the VEX occultation analyzed. So, before studying the frequency residuals within the Abel transform, is extremely important to calibrate properly the baseline.

The process to obtain the polynomial which corrects for the thermal noise, spacecraft clock, trajectory and other sources of errors is as follow: the portion of the frequency residuals outside the atmosphere (baseline), in particular before the ionosphere of the target, is processed through a polynomial fitting, in order to obtain the coefficients of a order  $n$  polynomial. The selection of the polynomial order depends on how good the baseline is: a baseline already at around zero mean value, without strong sinusoidal trends, can be simply fitted with a first order polynomial, as for all the MGS data analyzed (in general is always preferable to keep as low as possible the order  $n$  of the polynomial). On the other hand, for the Venus Express data, a second order fitting was mainly required. The trend of the baseline is directly linked to the stability of the Ultra Stable Oscillator, which is given in terms of Allan deviation, or "fractional frequency uncertainty", i.e. residual frequency divided by transmit frequency. Both the USO for MGS and VEX, from literature, were characterized by a stability of  $10^{-13}$  over timescales of 1-100 seconds. The reason why the VEX data required a second order fitting, could be related to an effective lower stability on the VEX USO, with respect to

what found in literature. In any case, the polynomial fitted in the baseline is made to obtain a best guess for the reference frequency sent by the spacecraft, which corrects for the errors mentioned before. Then, these coefficients are being used for making new data, through a polynomial evaluation, over the whole time-span of the original frequency residuals. To conclude, the calibrated reconstructed frequency residuals will be the difference between the original reconstructed frequency residuals and the polynomial evaluated through the coefficients from the baseline. This new data can be seen as the reconstructed frequency residuals corrected with a better fit of the reference frequency, which will lead to reliable results for the atmosphere parameters of the planet. The errors described above can all be seen as frequency shifts which affect the frequency residuals of the occultation experiments. The formula [4.12](#) summarize the corrections made on the reconstructed frequency residuals as:

- troposphere T;
- Ionosphere I;
- polynomial of order  $n$  which corrects for the spacecraft clock, plasma noise, thermal noise, trajectory and higher order errors.

$$\Delta f_{reconstructed-calibrated} = \Delta f_{reconstructed} - T + I - [p_1 + p_2t + p_3t^2 + \dots + p_nt^n] \quad (4.12)$$

where  $t$  is the time related to the frequency residuals and  $n$  is the order of the calibration polynomial selected.

Summarizing, all the MGS data have been calibrated with a first order polynomial fitting. On the other hand, for VEX, the Egress cases have been mainly calibrated with second order polynomials (only few cases with first order polynomials), while more attention and details should be provided on the VEX Ingress cases. In fact, within the VEX data analyzed, the baselines of the Ingress cases were all characterized by strong drift and sinusoidal trends (see [Figure 4.22](#)), which cannot be traced back to the USO errors only. This baseline behavior has been analyzed and the probable cause is the trajectory reconstruction of VEX. In particular, in order to consider and study only the atmospheric effects present in the

frequency residuals, the position and the trajectory of the spacecraft should be known perfectly. However, this is not possible, and even small errors in the knowledge of the trajectory (1m) could propagate because of the high dynamics (as gravity for example) when the spacecraft approaches the planet. This is especially pronounced in the Ingress region, because the uncertainty is higher before the closest approach of the spacecraft, while for the Egress this is less common because it is easier to correct the dynamical parameters after the encounter, which results in lower uncertainties in the spacecraft position. This effect will lead to errors in the trajectory, so the expected Doppler shift is characterized by fluctuations too, and in turn, this affects frequency residuals. This is why a strong drift and sinusoidal trend is seen in the frequency residuals (see example of Figure 4.22). The best way to solve this issue would be to simultaneously estimate and correct the trajectory (provided by the Navigation team in SPK kernels) of the spacecraft, however because of time constraints this have not been addressed within this investigation. As a first order, the problem has been solved by increasing the order of the polynomials used for the baseline fitting, so that it will correct also for the errors in the trajectory.

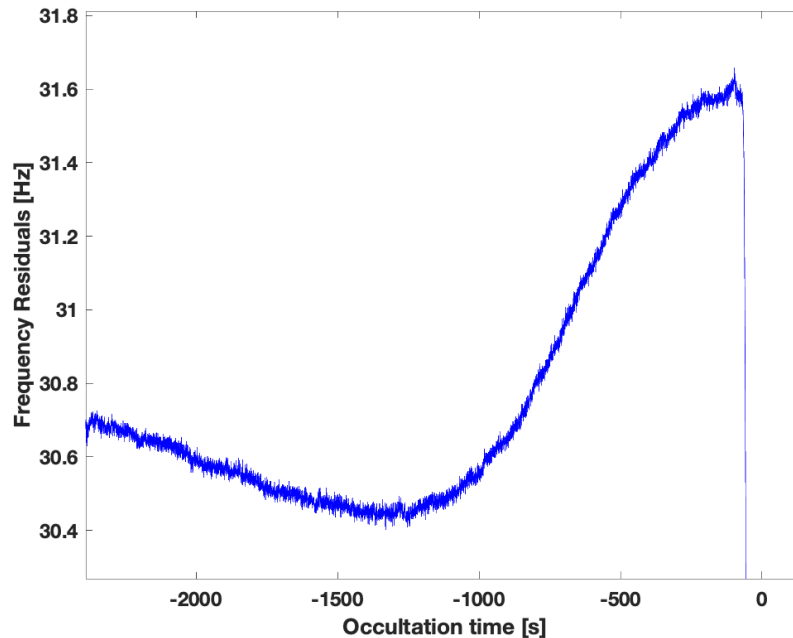


**Figure 4.22:** Baseline of the VEX-JPL DOY 070-2014 Ingress occultation.

The strong drift behavior of the baseline of Figure 4.22 is not caused by the atmosphere of Venus, which starts at around -150 seconds of the occultation time. All the points before this time are far away with respect to the atmosphere of Venus (for example the point at -1270 s is at an altitude of 1818 km with respect to Venus and the point at -500 s is at 215 km altitude), so these points are not influenced by the atmosphere of Venus, and the strong drift seen in the baseline is due to errors in the trajectory reconstruction. (Please note that the occultation time of Figure 4.22 is defined as the time which determine the occultation condition of one target relative to another target, as seen by an observer at a given time).

An example of the effect of the calibration process on the frequency residuals is shown in Figure 4.23, which represents the VEX frequency residuals of Figure 4.22 calibrated for Earth's troposphere/ionosphere and a 7<sup>th</sup> order polynomial to correct for the trajectory estimation errors, thermal noise, spacecraft clock and plasma noise.

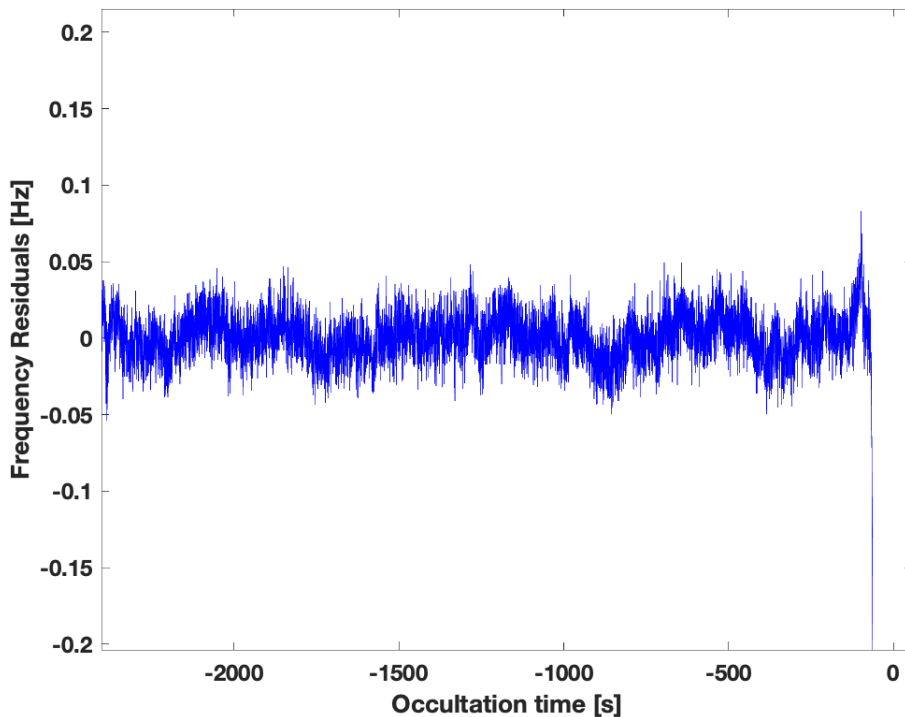


**Figure 4.23:** Baseline calibrated of VEX-JPL DOY 070-2014 Ingress occultation.

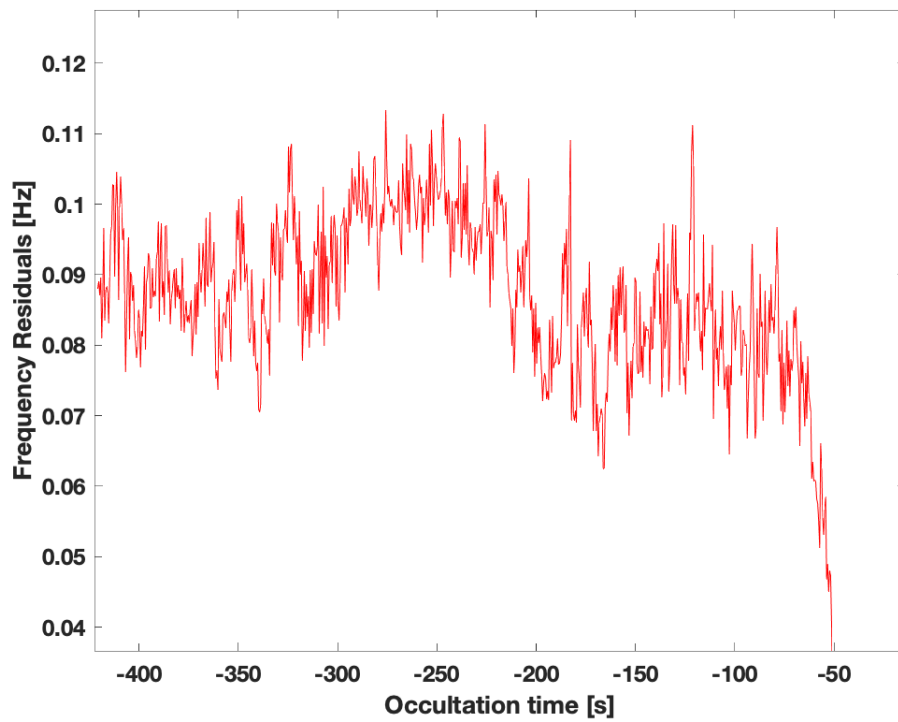


Figure 4.24: Baseline not calibrated of MGS DOY 015-2002 Ingress occultation.

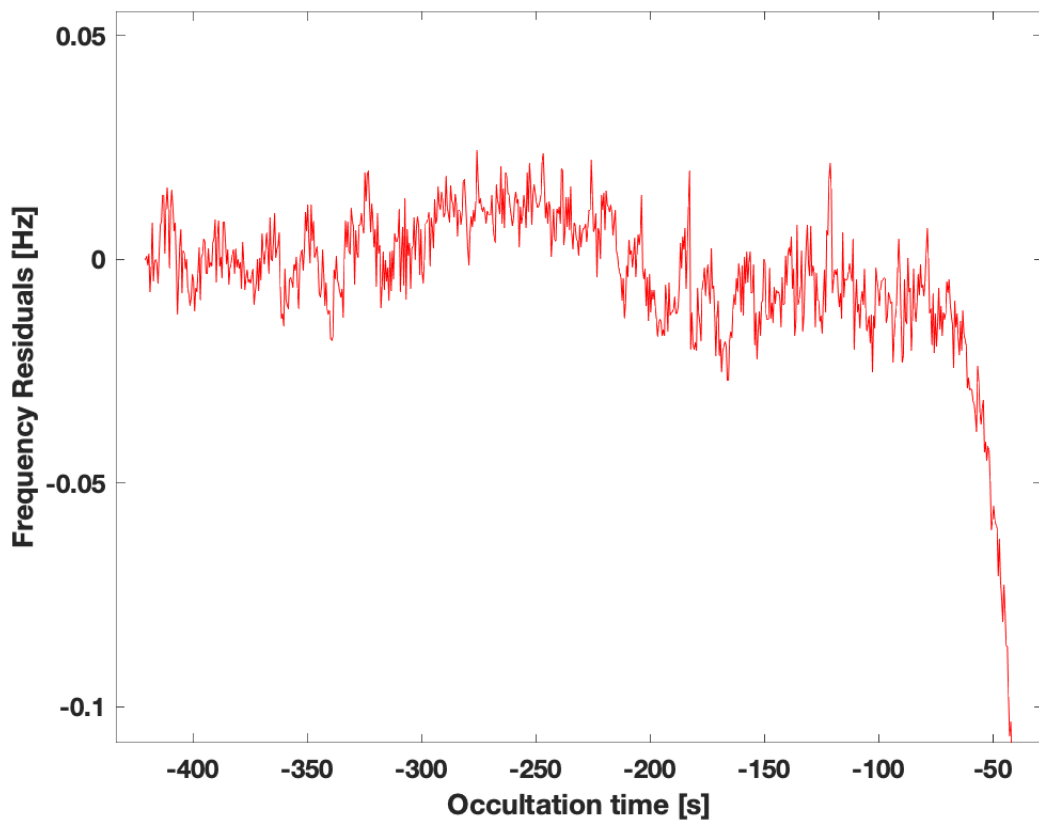


Figure 4.25: Baseline calibrated of MGS DOY 015-2002 Ingress occultation.

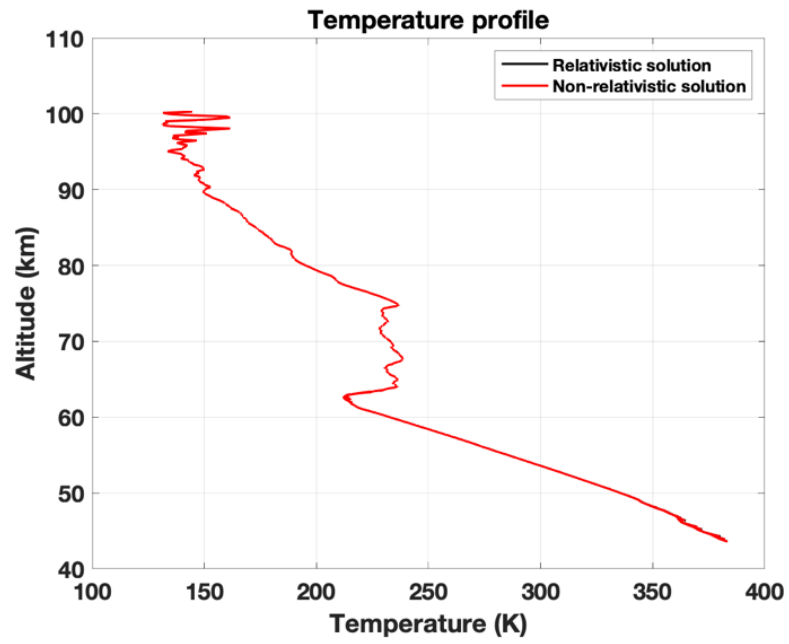
On the other hand, the frequency residuals for Mars, as discussed before, were already flat and without drifts, so only a bias (with a first order polynomial) have been applied in order to have the data around the zero value, see Figures [4.24](#), [4.25](#).

In particular, as can be seen, the Mars occultation data available was characterized by a very short baseline, while for the calibration process is always preferable having longer baseline, which means more points to evaluate properly the fitting of the reference frequency outside the atmosphere. However, since the Mars' residuals were already good fitted from the beginning, the results have been obtained for the Mars data, too.

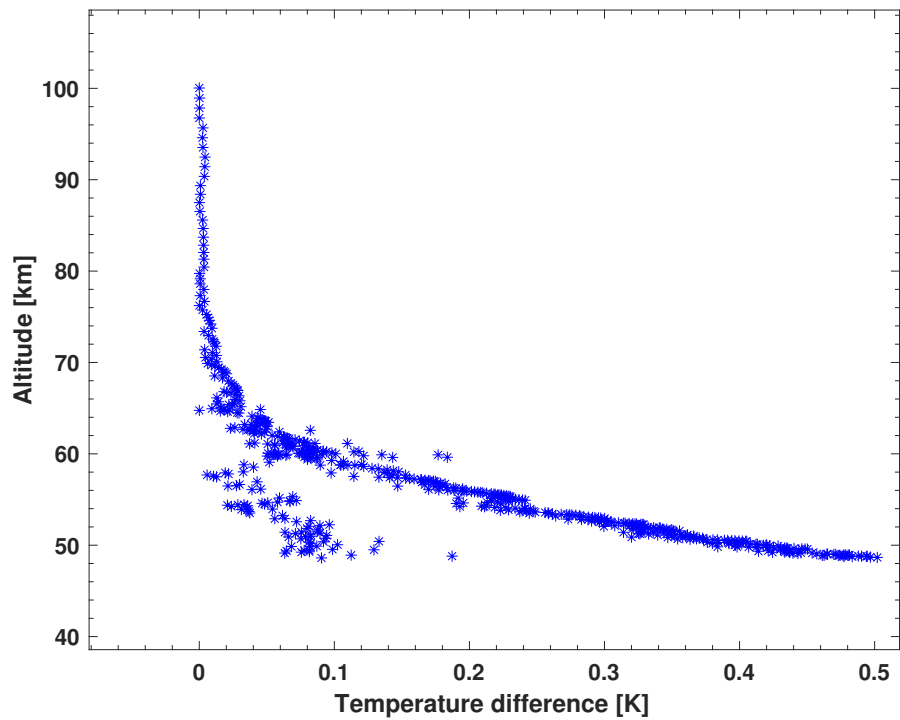
## 4.5 Relativistic vs non-relativistic solution

Another important study has been conducted on the difference between the relativistic solution and the non-relativistic solution, both for planet Venus and Mars. The differences from the physical and mathematical point of view have already been pointed out, here the results and the differences in terms of vertical profiles are showed. For this study, one occultation of Venus Express and one from Mars Global Surveyor (both from JPL data), have been analyzed, see Figures [4.26](#) and [4.27](#).

By looking at Figures [4.26a](#) - [4.27a](#), it can be seen that for Venus, as well as for Mars (as reported in [24](#)), the relativistic effects are negligible. In fact, in the images the two profiles are perfectly overlapping. In addition, Figures [4.26b](#) - [4.27b](#) permit to understand that the difference in temperature between the profiles, is always lower than 0.5 K for both the planets (for Mars these differences are even orders of magnitudes smaller than on Venus, because its thin atmosphere permits to obtain easier computation within the non linear system of the relativistic solution), confirming that within this research the relativistic effects could be neglected. The reason behind these results is that the ratios of the relativistic  $(v/c)^2$  and  $U/c^2$  terms to the non-relativistic  $v/c$  term (of Equation [3.21](#)) are both on the order of 1 part in  $10^5$ . So, within this research the relativistic effects have been neglected since they do not have a strong influence on the results. In addition, the non-relativistic solutions involve linearized systems, which computations are easier to be solved and less affected by errors.

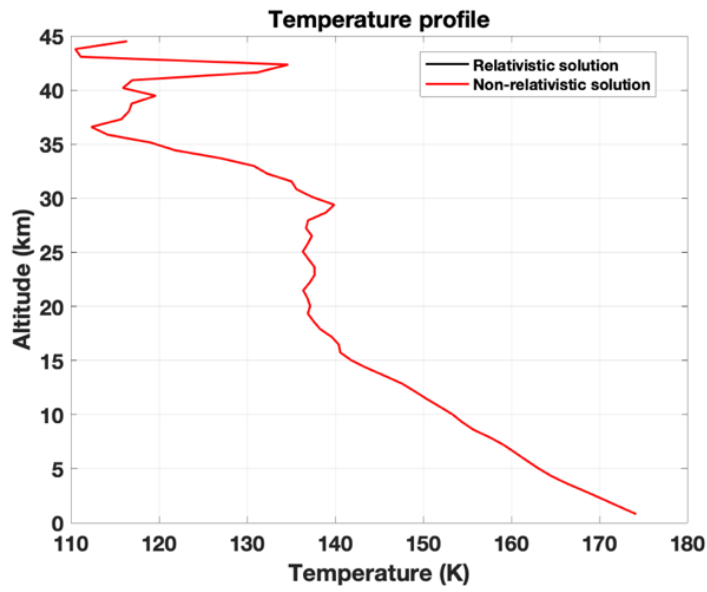


(a)

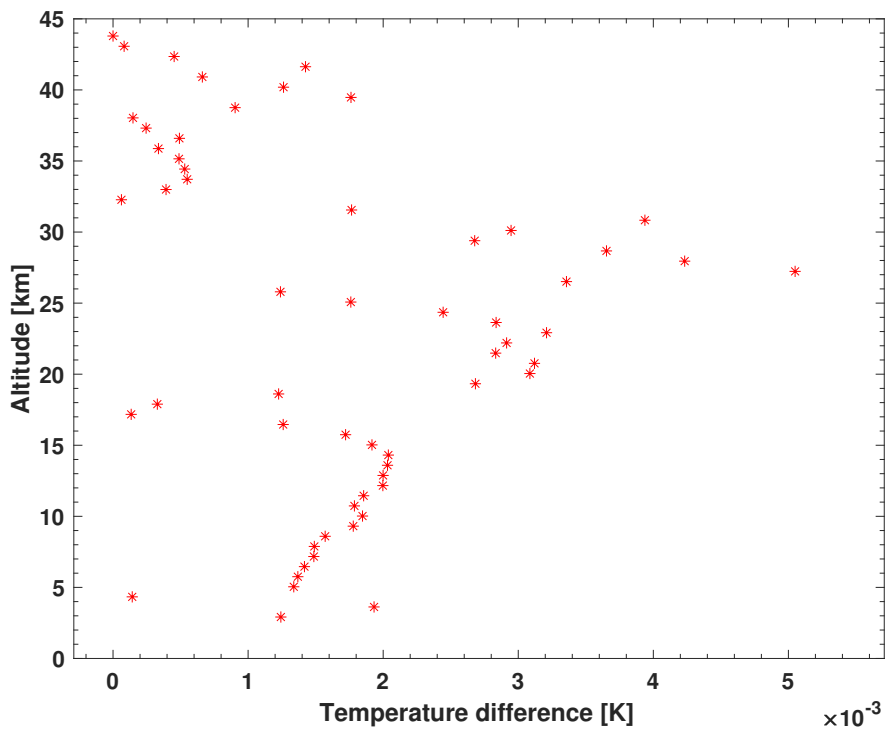


(b)

**Figure 4.26:** a) Comparison of temperature profiles between relativistic solution (black line) and non-relativistic solution (red line) for Venus, from VEX JPL data. b) temperature difference between the two solutions.



(a)



(b)

**Figure 4.27:** a) Comparison of temperature profiles between relativistic solution (black line) and non-relativistic solution (red line) for Mars, from one MGS occultation. b) temperature difference between the two solutions.



## Chapter 5

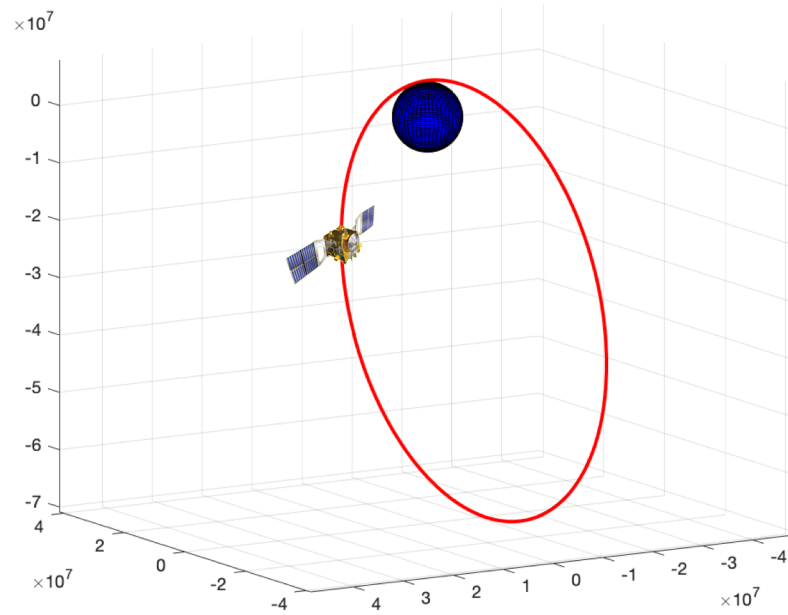
# Radio Occultation results

In this Chapter the results from the MATLAB algorithm developed for the occultation experiments of VEX and MGS are shown. In particular, Section 5.1 will provide and compare the vertical profiles of temperature, pressure, electron density, neutral atmosphere and other scientific parameters to show the main difference between Venus and Mars' atmospheres. Section 5.2 will show the temperature and pressure results obtained for the whole set of Venus and Mars occultations analyzed. To conclude, Section 5.3 will focus on scientific results obtained from the VEX data collected throughout 2014 by NASA's Deep Space Network and managed by the Jet Propulsion Laboratory, which occultation data has never been analyzed before.

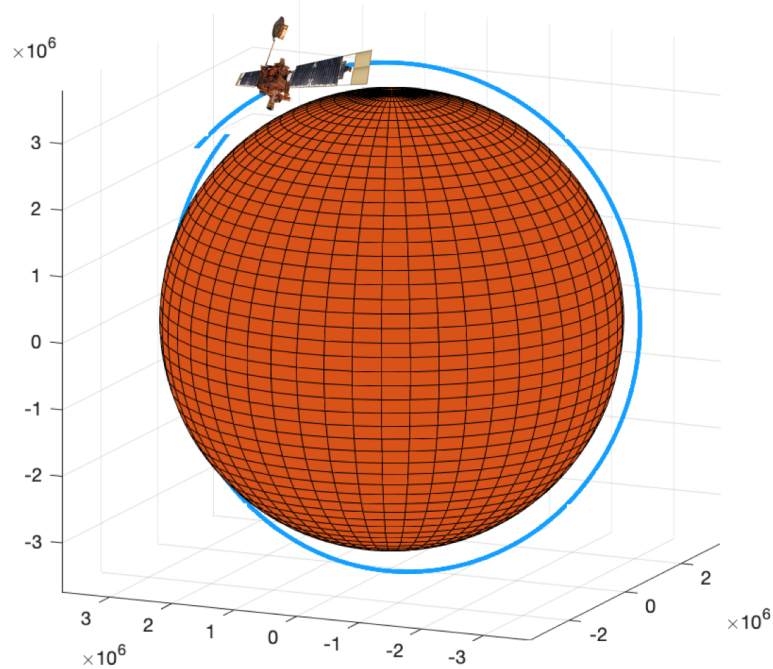
### 5.1 Venus and Mars: Atmospheres comparison

First of all, a reference occultation data, both for Venus and Mars, has been analyzed in order to show the main differences between the two planets' atmospheres. The occultation data selected for this study are:

- Venus: 28<sup>th</sup> January 2014 Egress;
- Mars: 27<sup>th</sup> December 1998 Ingress.



(a)

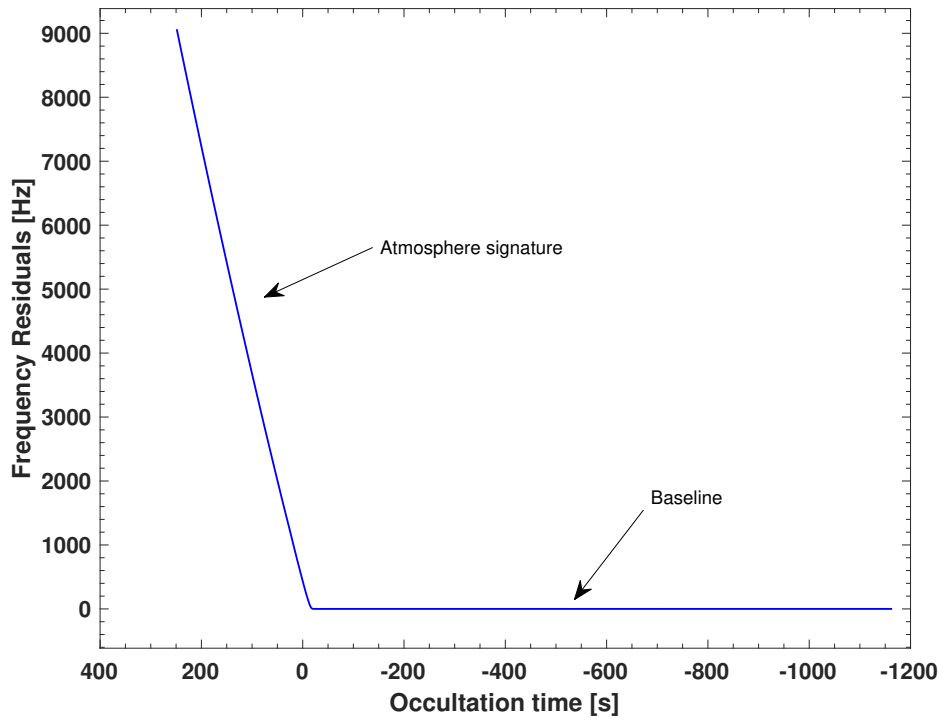


(b)

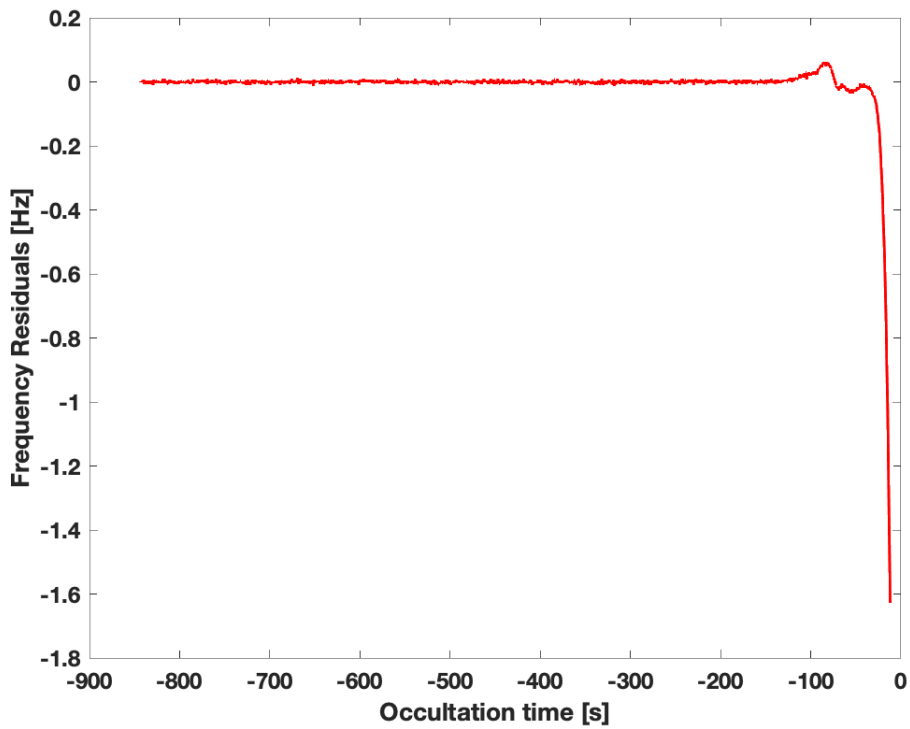
**Figure 5.1:** Orbits of the two missions. **a)** Orbit of VEX around Venus, characterized by an apocenter altitude of 66000 km and pericenter altitude of 250 km; **b)** Orbit of MGS around Mars with an apocenter altitude of 436.5 km and a pericenter altitude of 372.8 km. (spacecrafts not in scale)

The frequency residuals of these occultations, already calibrated, are shown in Figure 5.2. From the general point of view, they are characterized by two main regions: the first one is the flat part of the residuals, the baseline (region between 20 s to 1160 s of Figure 5.2a) and the second part is the slope region, when the residuals start decreasing. This is the region when the signal starts to travel through the planet's atmosphere, which refracts the radio signal causing a frequency shift.

In addition, by looking at the frequency residuals of Venus and Mars, it is possible to see the first major difference between these two atmospheres, which is the stronger influence of Venus' atmosphere on the radio signal sent by the spacecraft compared to the one caused by the Mars' atmosphere. In fact, the frequency residuals of VEX, in the region inside the atmosphere of the planet, are characterized by higher values, with a peak of 5000 Hz. This is due to the thick Venus' atmosphere, which has a strong effect on the Doppler signature. On the other hand, Mars' atmosphere is very thin, and does not cause a frequency shift as high as on Venus, in fact the peak on Mars is -1.6 Hz.

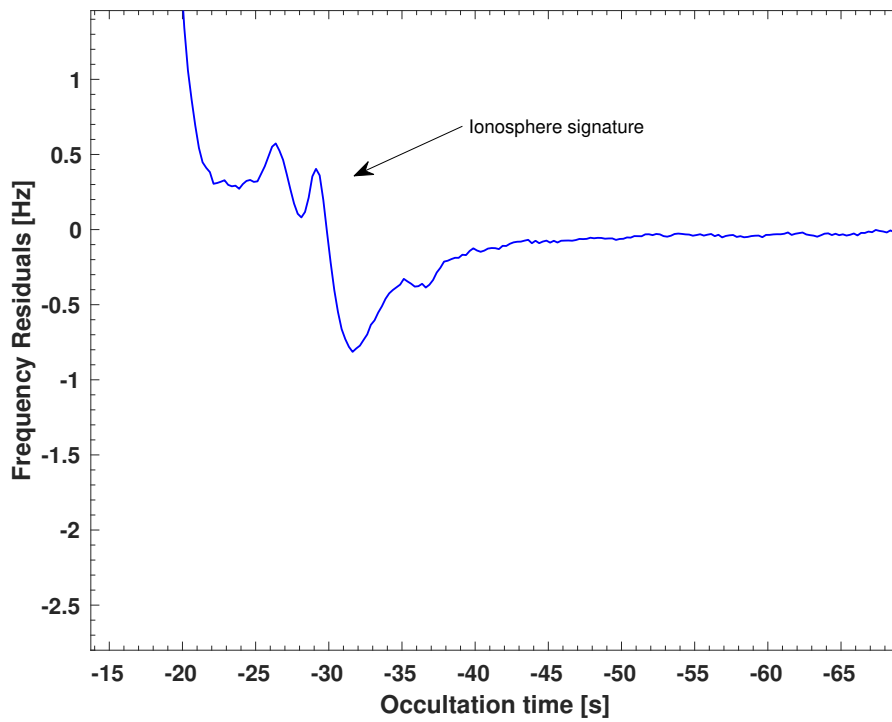


(a)

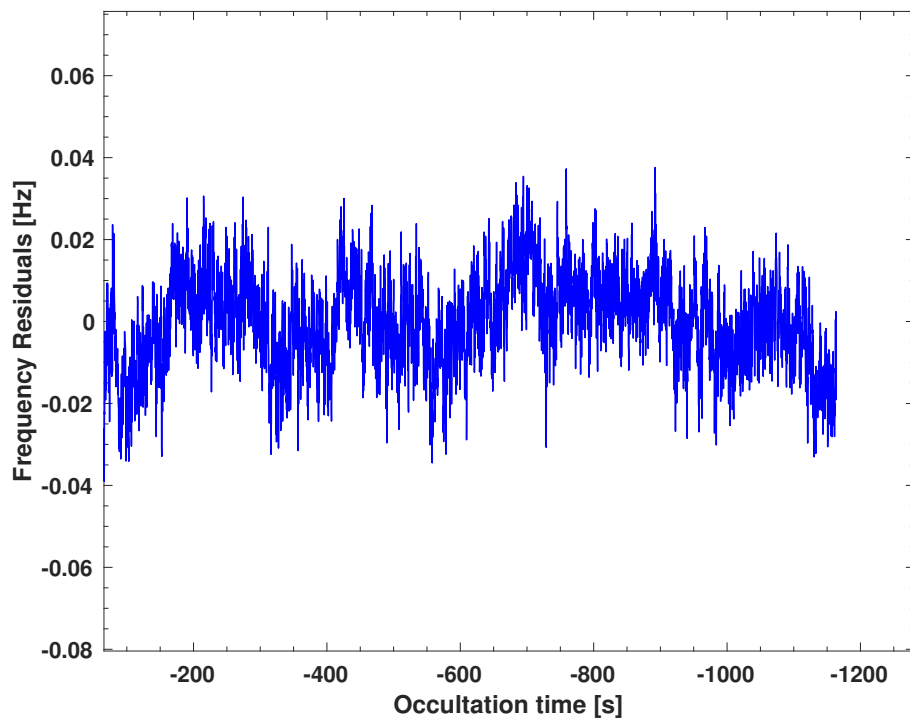


(b)

**Figure 5.2:** Frequency residuals of the occultations. **a)** VEX Egress DOY 028 2014; **b)** MGS Ingress DOY 361 1998.



(a)



(b)

**Figure 5.3:** Closer look of Figure 5.2 on the VEX ionosphere and its baseline. **a)** Ionosphere of VEX Egress DOY 028 2014 ; **b)** Baseline VEX Egress DOY 028 2014.

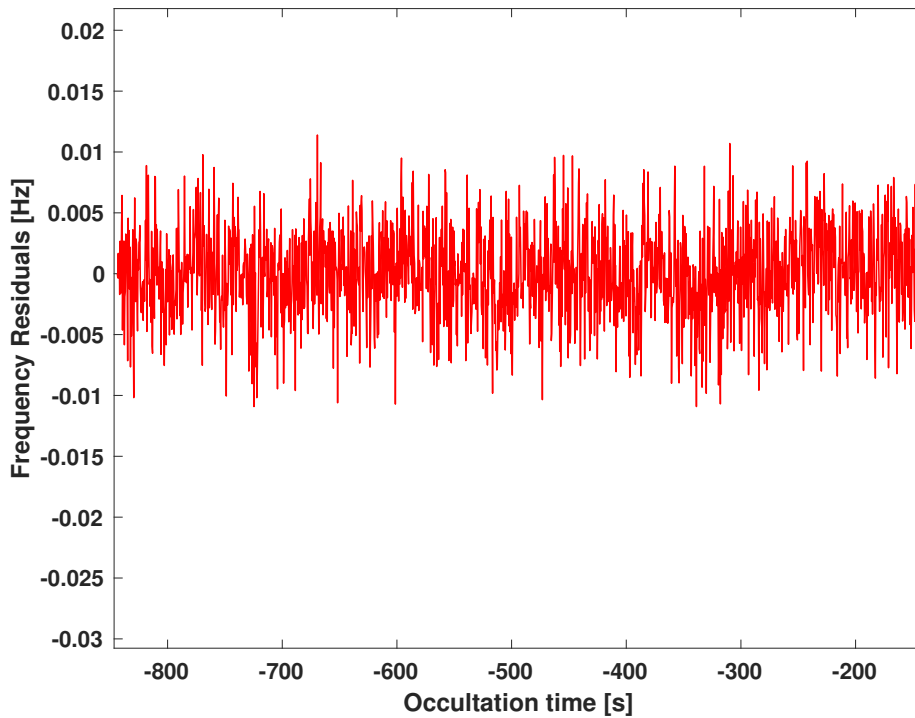
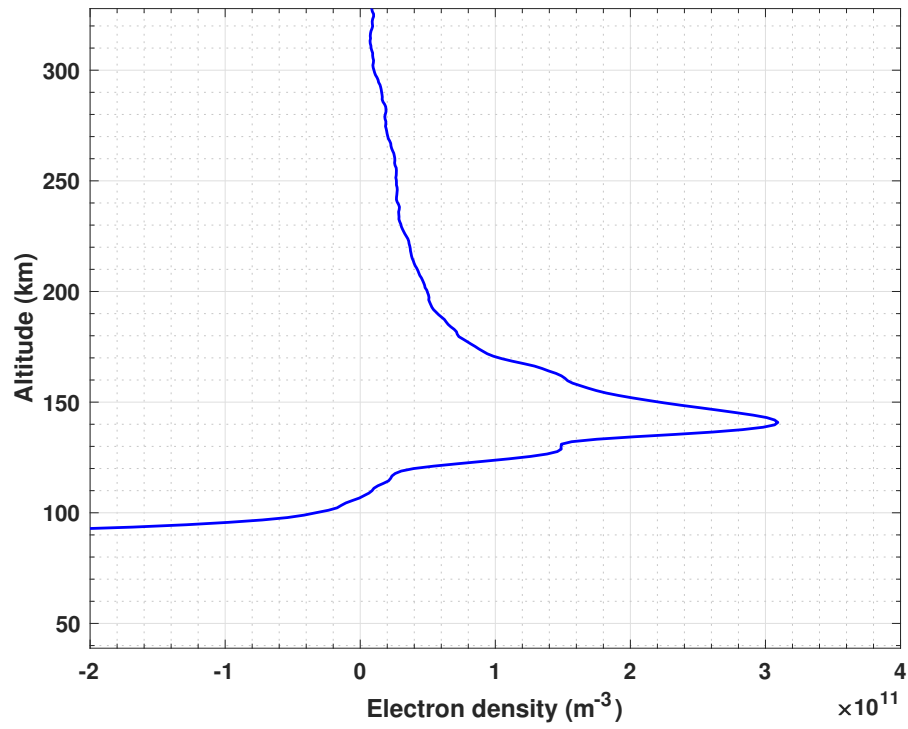


**Figure 5.4:** Baseline MGS Ingress DOY 361 1998.

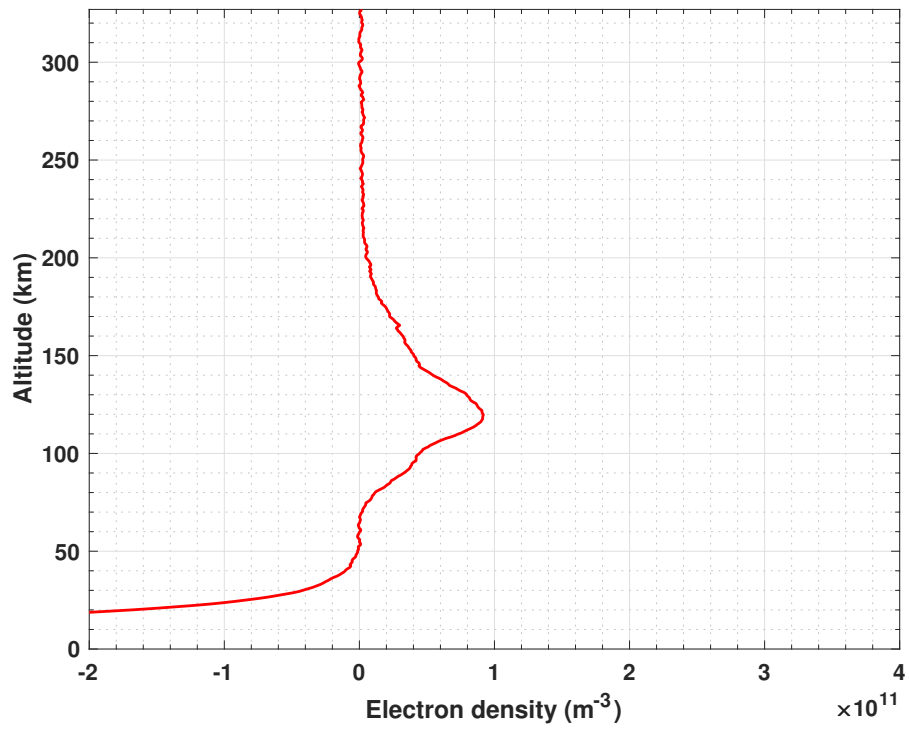
The first requirement on the baseline of the frequency residuals is that it must be flat, with a zero mean value. If not, the results from the atmosphere algorithm will not be reliable since the signal is traveling outside of the atmosphere at the time and is not affected. That is why the residuals must be calibrated, as already mentioned in Section 4.4. Another great difference between Venus and Mars, encountered in this investigation, was that the baselines of the VEX frequency residuals required higher order calibrations than the Mars' residuals, which were characterized by flat and good baselines even without calibration (the first order calibration for Mars was still required to correct for the bias of the baseline with respect to the zero value). This could be related to the Ultra Stable Oscillator of VEX, which was not probably as stable as thought, and could also be related to errors in the trajectory estimated by the navigation team, especially for the ingress case, due to the approach of the spacecraft to the dynamics of the planet. By looking at Figures 5.3a - 5.4 it is possible to notice also the ionospheres of the planets. In fact, the ionosphere signature is characterized by a positive peak in the

frequency residuals (at  $-25s$  s for VEX and  $-100s$  s for MGS). The ionosphere's peak is positive, because the charged particle effect advances the Doppler phase of the signal, which is translated in a positive frequency shift, so that the observed frequency (sky frequency) is higher with respected to the reconstructed one and, as a consequence, the  $\Delta f$  is positive (remember that  $\Delta f = f_{observed} - f_{reconstructed}$ ). Then, after the ionosphere, the spacecraft starts entering in the neutral atmosphere of the planet (slope of the frequency residuals).

These frequency residuals have been analyzed through the atmosphere algorithm developed within this work, and the next plots shows the comparison between the Venus and Mars' relevant atmospheric parameters.



(a)



(b)

**Figure 5.5:** Electron density profiles.  
a) VEX Egress DOY 028 2014;  
b) MGS DOY 361 1998.

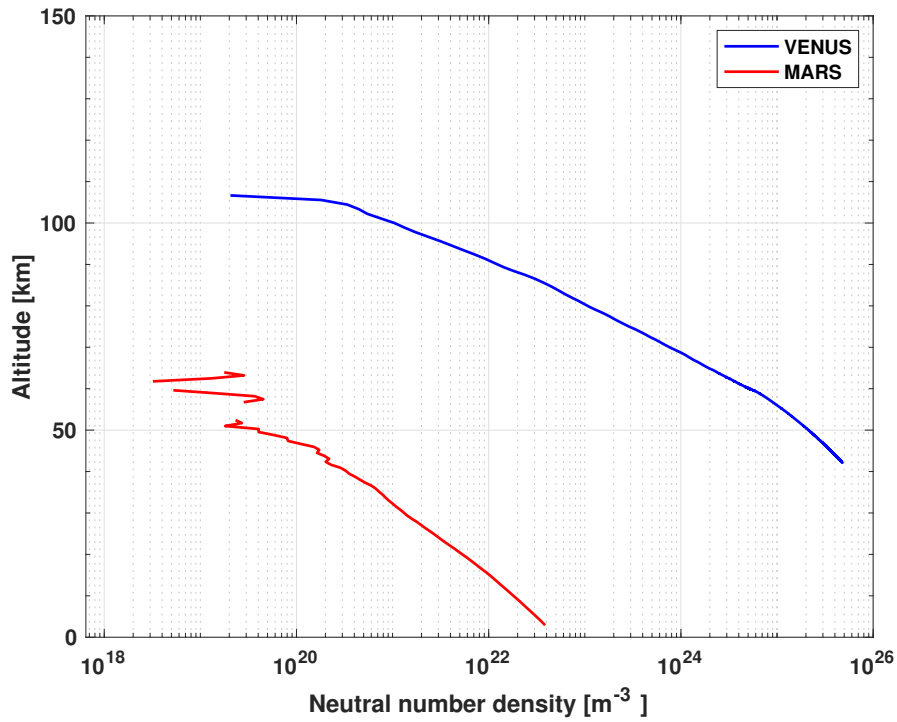


**Figure 5.6:** Neutral number density profiles.  
a) VEX Egress DOY 028 2014;  
b) MGS DOY 361 1998.

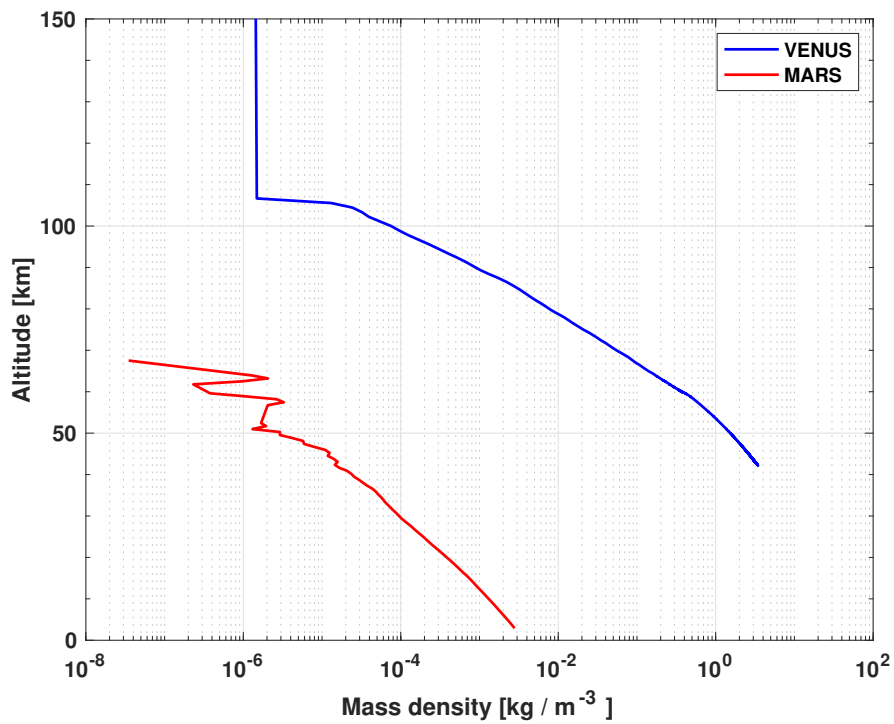
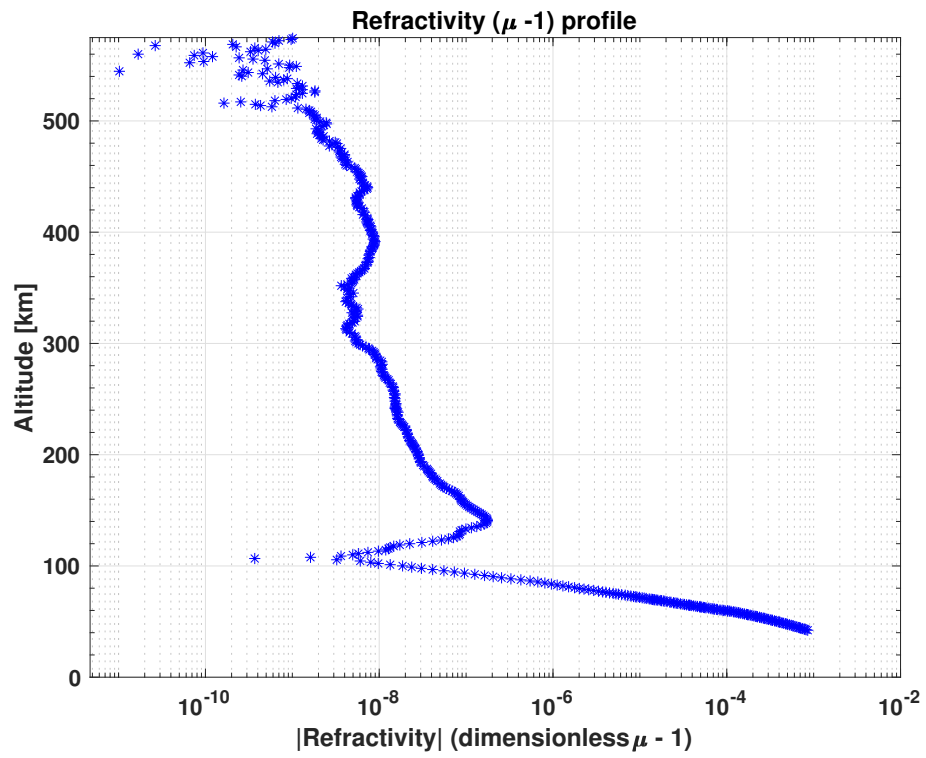
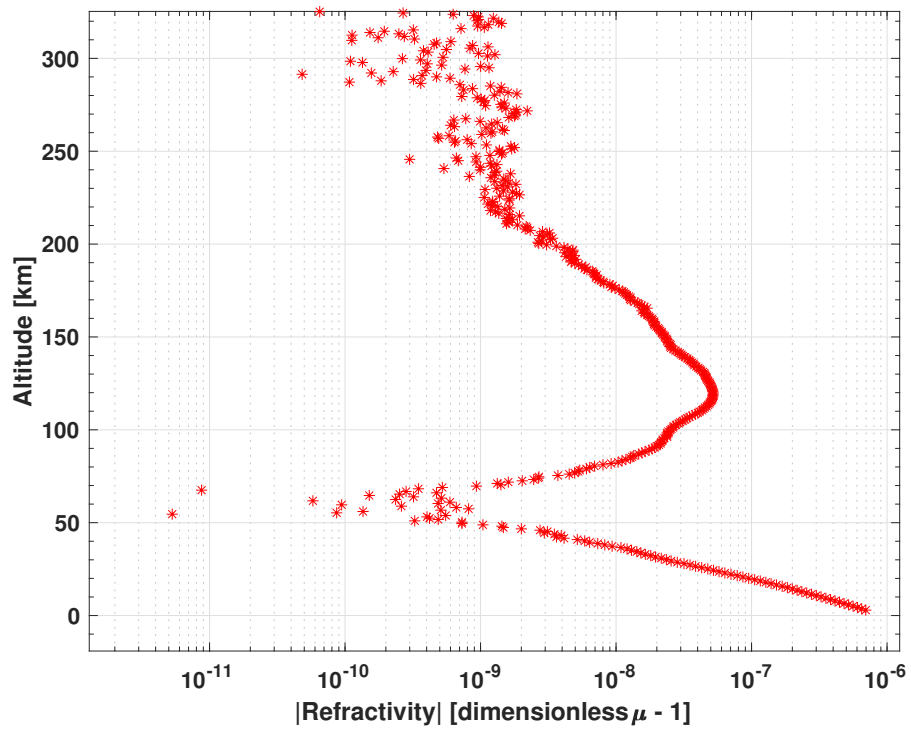


**Figure 5.7:** Mass density of neutral atmosphere profiles.  
a) VEX Egress DOY 028 2014;  
b) MGS DOY 361 1998.

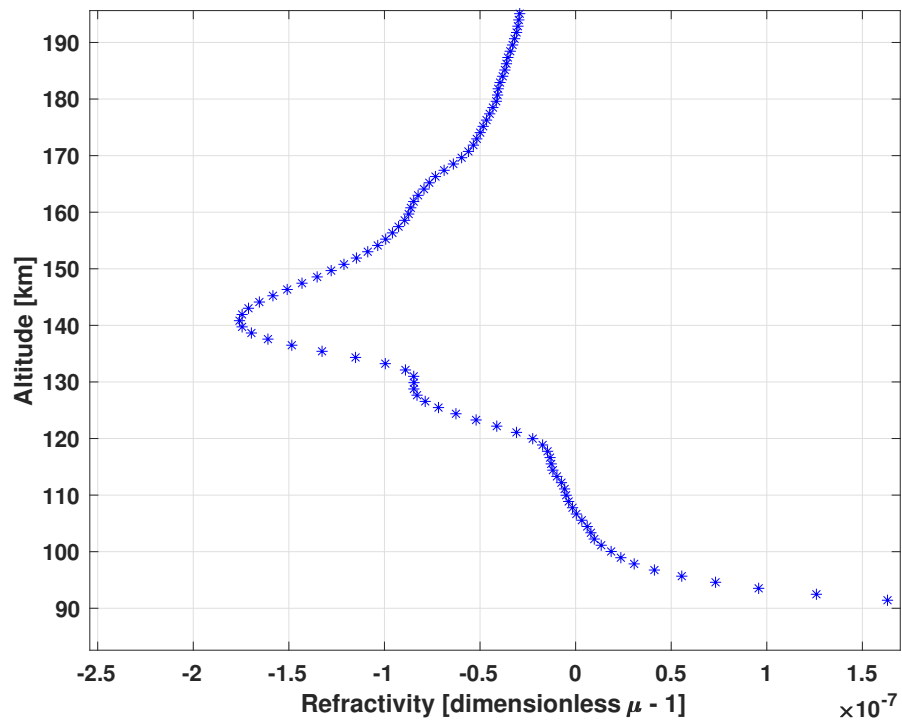


(a)

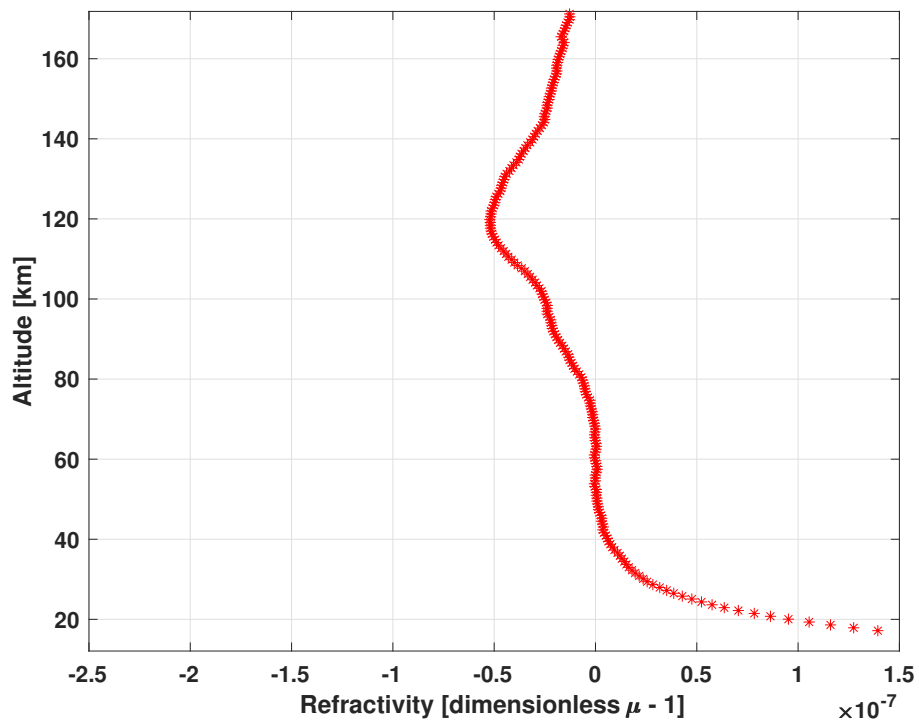


(b)

**Figure 5.8:** Refractivity profiles.  
a) VEX Egress DOY 028 2014;  
b) MGS DOY 361 1998.

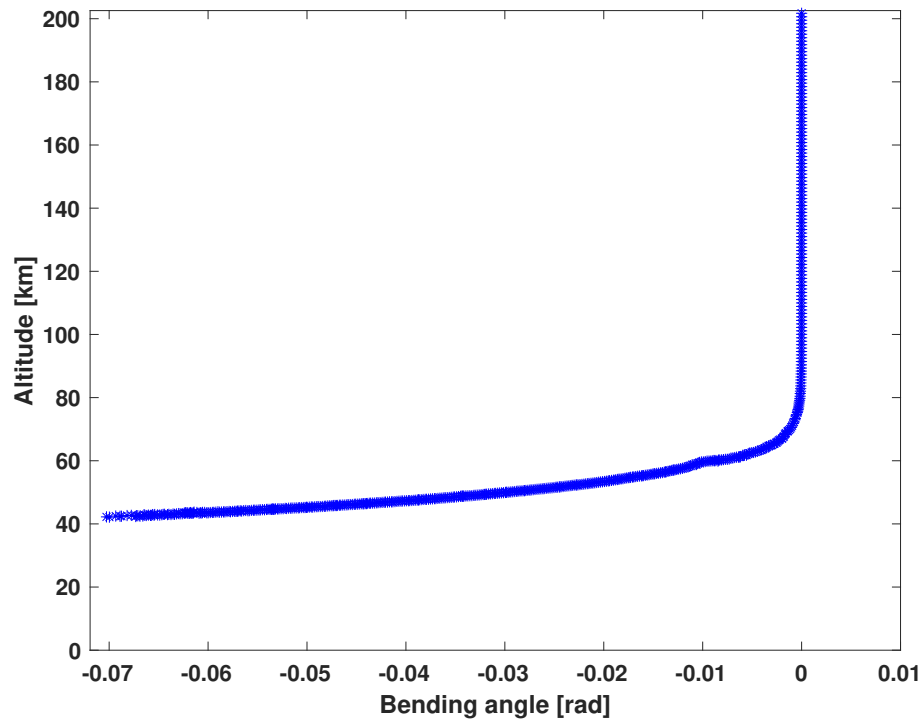


(a)

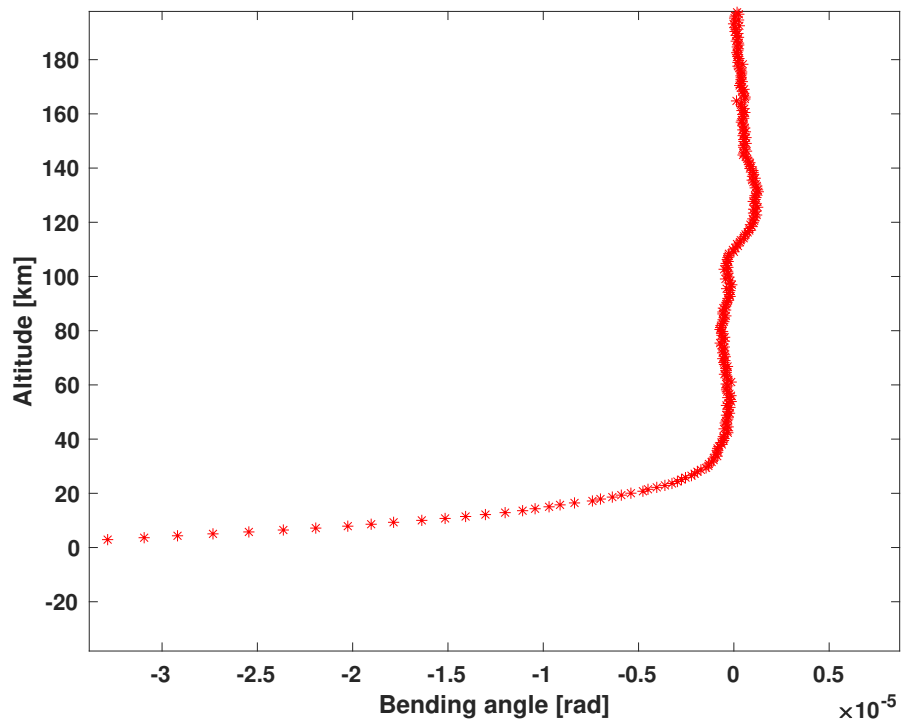


(b)

**Figure 5.9:** Closer look on the refractivity profiles.  
a) VEX Egress DOY 028 2014;  
b) MGS DOY 361 1998.



(a)



(b)

**Figure 5.10:** Bending angle profiles.  
a) VEX Egress DOY 028 2014;  
b) MGS DOY 361 1998.

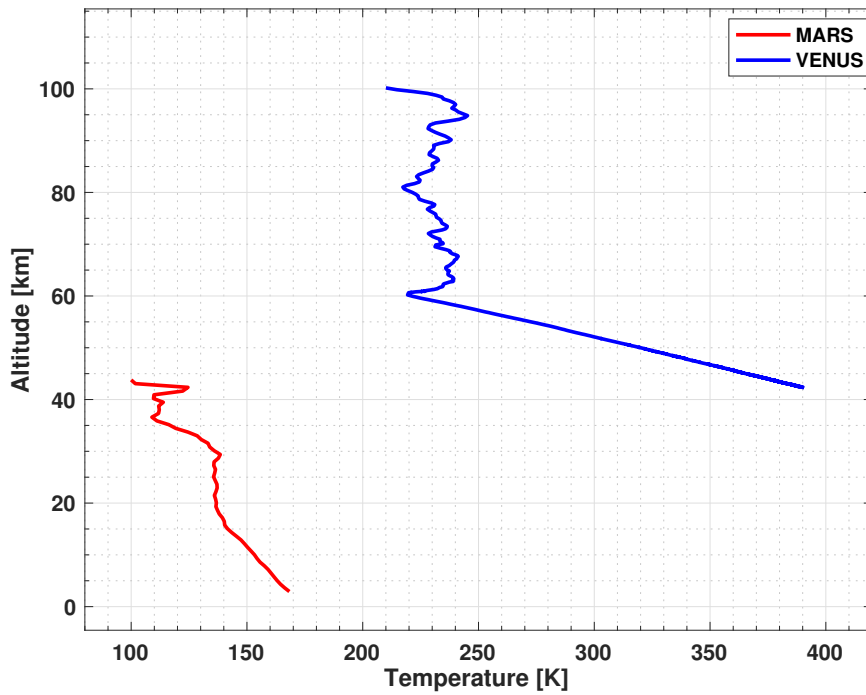


**Figure 5.11:** Temperature profiles.  
 a) VEX Egress DOY 028 2014;  
 b) MGS DOY 361 1998.

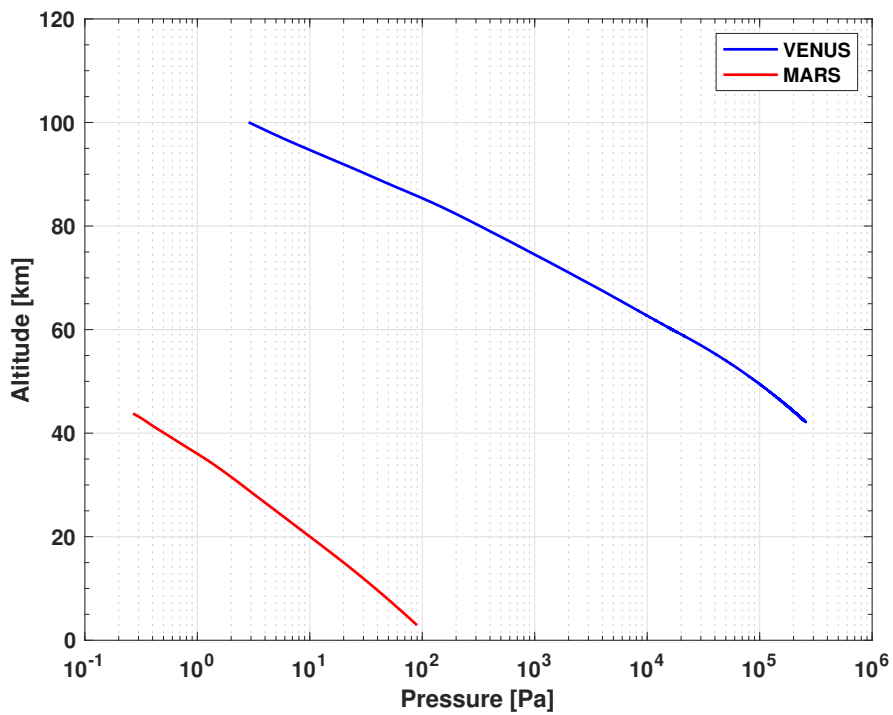


**Figure 5.12:** Pressure profiles.  
 a) VEX Egress DOY 028 2014;  
 b) MGS DOY 361 1998.

First of all, Figure 5.5 shows the electron densities within the ionospheres of the planets: the one of Venus around an altitude of 140 km, and the one of Mars at an altitude around 120 km. The ionosphere is ionized by solar radiation, so it depends on several factors, as the local time, the day of the year, the solar cycle and so on. Furthermore, Venus' ionosphere is characterized by an higher value of the electron density, which could be related to different reasons: Venus is closer to the Sun with respect to Mars, and the Venus occultation occurred during the day 10:20 AM (Local Solar Time) while the one for Mars was in the night 03:51 AM (Local Solar Time), which influences too the amount of charged particles present in the ionosphere.

Another strong difference between the two planets can be seen by analyzing the neutral number density of Figure 5.6, as well as the mass densities in the neutral atmosphere of Figure 5.7. In fact, the difference between these two parameters is five orders of magnitude at an altitude of 50 km. This highlights the extremely thick and dense atmosphere of Venus. In addition, it is interesting to notice the thin neutral atmosphere of Mars, which starts at an altitude of only 50 km, on the other hand the one of Venus is thicker and starts at 105 km altitude. Moreover, by looking at these plots, it is possible to notice that the results for Venus are not available below an altitude of about 40 km, while for Mars is possible to study the whole atmosphere, until few meters above the surface. This is due to the fact that a dense atmosphere, as the one of Venus, is characterized by a lower limit of occultation measurement. This limit is determined by the strong bending, refraction, absorption and defocussing of the radio signal, so that the signal becomes so weak that reliable detection is no longer possible [5]. In particular an absolute lower limit can be defined, called level of super-refraction  $R_c$  where:

$$\frac{1}{R_c} = -\mu \left. \frac{d\mu}{dr} \right|_{r=R_c} \quad (5.1)$$

An horizontal ray path at this critical radius turns with a radius of curvature equal to the radius at that position, in other words the ray circles the planet. For Venus it is known to be around 32 km. Within this research, it has not been possible to study the signal below 40 km. As mentioned before, this does not happen for Mars, since its thin atmosphere does not cause strong bending on the radio signal. The bending of the radio signal can be observed in Figure 5.10, where it is possible

to notice that the bending (evaluated in radians) caused by Venus' atmosphere is several orders of magnitude higher than Mars'. In the same plot of the bending, one can notice also that the ionosphere bends the radio signal in an opposite direction with respect to the bending caused by the neutral atmosphere (within this work the convention adopted is to have the ionosphere characterized by  $\alpha > 0$  while the neutral atmosphere by  $\alpha < 0$ ). In addition, the bending caused by the neutral atmosphere of Venus on the ray path is 4 degrees at 40 km altitude, while for Mars the highest value is only 0.0017 degrees.

To conclude this comparison, from the temperature profiles of Figure 5.11 and the pressure profiles of Figure 5.12, the strong temperature and pressure differences are clearly visible. At an altitude of 45 km the temperature of Venus is 360 K, while the one for Mars is 100 K. Regarding the pressures, at the same altitude Venus is characterized by 2 bar, while Mars only  $3 \cdot 10^{-6}$  bar.

To summarize, the two atmospheres of the planets show mainly big differences and not one similarity, with the Venus' atmosphere characterized by a hostile environment, which is difficult to be studied at altitudes below 50 km. On the other hand, the friendly Mars' atmosphere and its good environment are the reasons why Mars has been studied more than Venus, also with several rovers, which could last only few minutes on the Venus' surface. The similarities, from the engineering point of view are related to the fact that for both planets, the relativistic solutions are negligible, so that for both the non-relativistic ones have been considered. In addition, the MATLAB algorithm performs in the same way for the planets, the only difference are the inputs: the parameters (summarized in Table 5.1) and the frequency residuals. Lastly, as explained before, the calibration process showed differences between the planets, too: MGS was characterized by first order calibrations polynomials, while for VEX first and second order fitting was required for the egress cases, while for the ingress cases some occultations required even higher orders polynomials.

Parameters	Venus	Mars
Radius [km]	6051.8	3396.2
Refractive volume [ $m^3$ ]	$1.7953 \cdot 10^{-29}$ [21]	$1.804 \cdot 10^{-29}$ [9]
Mean molecular mass [kg/molecule]	$7.215210893390900 \cdot 10^{-26}$	$7.2209997659070690 \cdot 10^{-26}$
GM [ $\frac{m^3}{s^2}$ ]	$3.248585920000012 \cdot 10^{14}$	$4.2626422 \cdot 10^{13}$
Transmitted frequency [Hz]	$8419.084073 \cdot 10^6$	$8423 \cdot 10^6$

**Table 5.1:** Venus & Mars algorithm's parameters.

## 5.2 Venus and Mars: temperature and pressure results

Within this section the plots of temperatures and pressures obtained for the whole set of occultations of Venus and Mars will be shown. First of all, Tables [5.2] - [5.3] - [5.4] and Figure [5.13] summarize the details about the occultations analyzed. Note that the Latitude, Longitude and Local Solar Time computed are related to the occultation point at 50 km altitude for Venus, and 25 km altitude for Mars.

DOY-2014	Latitude [deg]	Longitude [deg]	Local Solar Time [hh:mm]	Sun-Earth-Spacecraft angle [deg]
020 Egress	-83.2742	188.1713	11:43	15.26
024 Egress	-80.2226	219.4474	10:25	20.54
028 Egress	-77.9247	233.2037	10:20	25.29
032 Egress	-77.3003	240.9983	10:40	29.45
036 Egress	-78.4562	244.7163	11:13	33.01
040 Egress	-81.0984	241.4943	12:14	35.99
044 Egress	-83.9361	218.4631	14:41	38.46
048 Egress	-82.8917	170.2951	19:00	40.49
052 Egress	-76.8379	150.7760	21:05	42.12
056 Egress	-68.5650	149.0389	22:00	43.42
058 Egress	-63.8022	150.5600	22:17	43.96
060 Egress	-58.8423	152.9668	22:32	44.44
062 Egress	-53.6435	155.9381	22:44	44.86
064 Egress	-47.9584	159.2675	22:57	45.22
066 Egress	-42.0727	162.9111	23:05	45.54
070 Egress	-28.9390	170.7901	23:22	46.02

**Table 5.2:** Venus egress occultations, NASA-JPL data.

Radio Occultation results

DOY-2014	Latitude	Longitude	Local Solar Time	Sun-Earth-Spacecraft
	[deg]	[deg]	[hh:mm]	angle [deg]
048 Ingress	84.4387	39.6256	03:24	40.46
052 Ingress	84.4673	61.0322	07:59	42.11
056 Ingress	84.0351	84.8049	01:35	43.41
058 Ingress	83.5954	96.6121	01:13	43.96
060 Ingress	82.9833	107.9732	00:58	44.43
062 Ingress	82.1854	118.6929	00:38	44.85
064 Ingress	81.1924	128.6728	00:27	45.22
066 Ingress	80.0118	137.8712	00:23	45.53
070 Ingress	76.4651	154.9445	00:06	46.02

**Table 5.3:** Venus Express ingress occultations 2014, NASA-JPL data.

DOY-2014	Latitude	Longitude	Local Solar Time	Sun-Earth-Spacecraft
	[deg]	[deg]	[hh:mm]	angle [deg]
361-1998 Ingress	66.5253	143.8650	03:51	79.41
015-2002 Ingress	63.3277	230.0374	08:07	62.22
364-2002 Ingress	73.2660	183.1851	04:14	50.13
077-2004 Egress	-36.1034	6.3494	03:25	60.44
008-2006 Ingress	63.9895	358.5970	06:28	115.42

**Table 5.4:** Mars Global Surveyour occultations, NASA-JPL data.

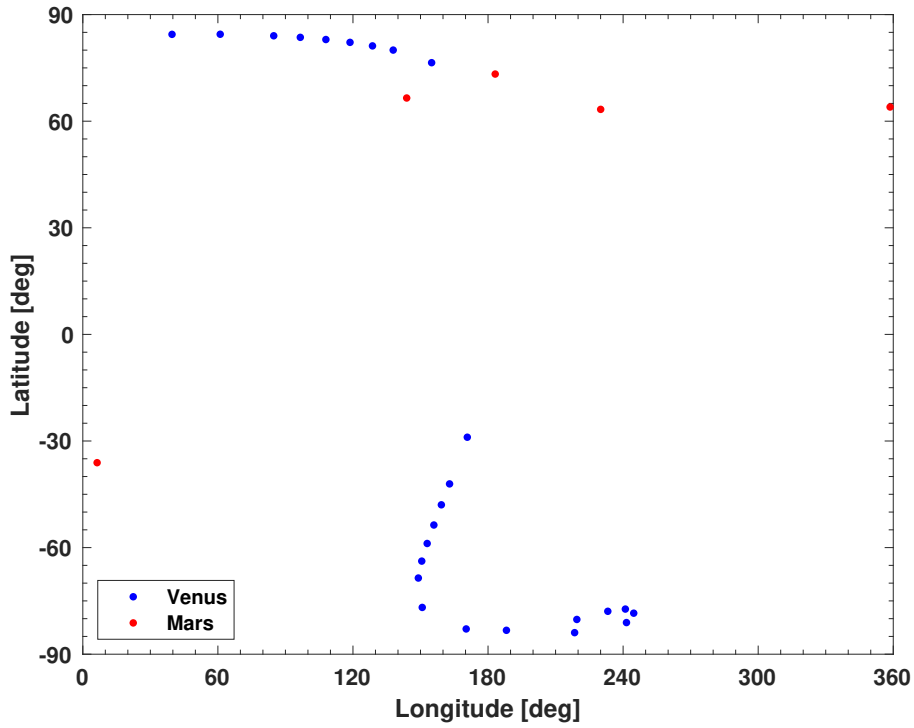


**Figure 5.13:** Spatial distribution of occultations data as a function of latitude and longitude. Points are related to the occultation point at 50 km and 25 km altitude for Venus and Mars, respectively.

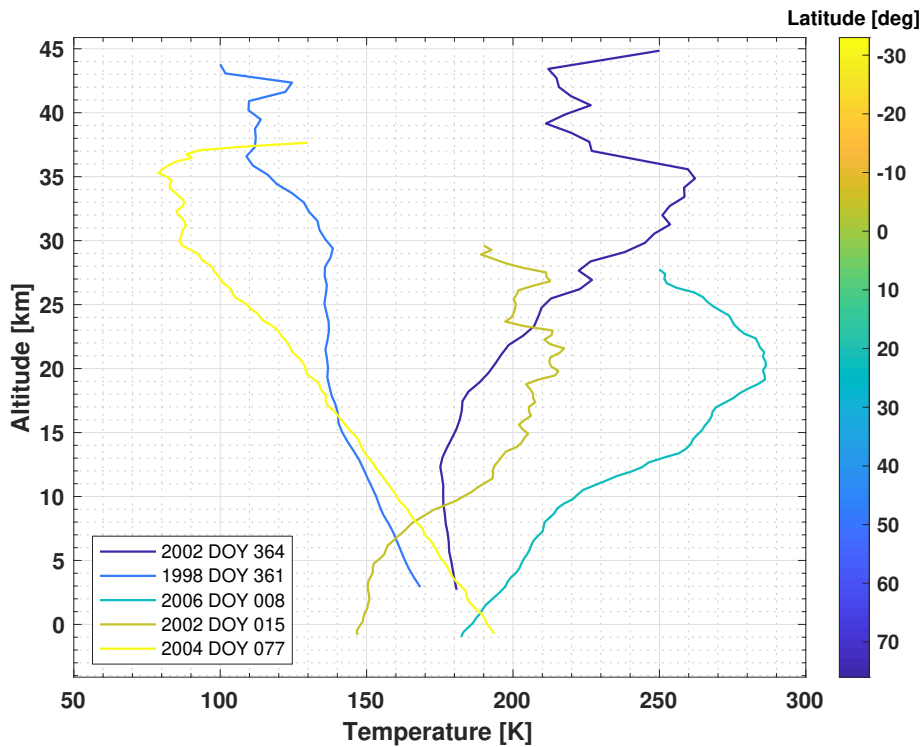


**Figure 5.14:** Temperature profiles of the MGS occultations.

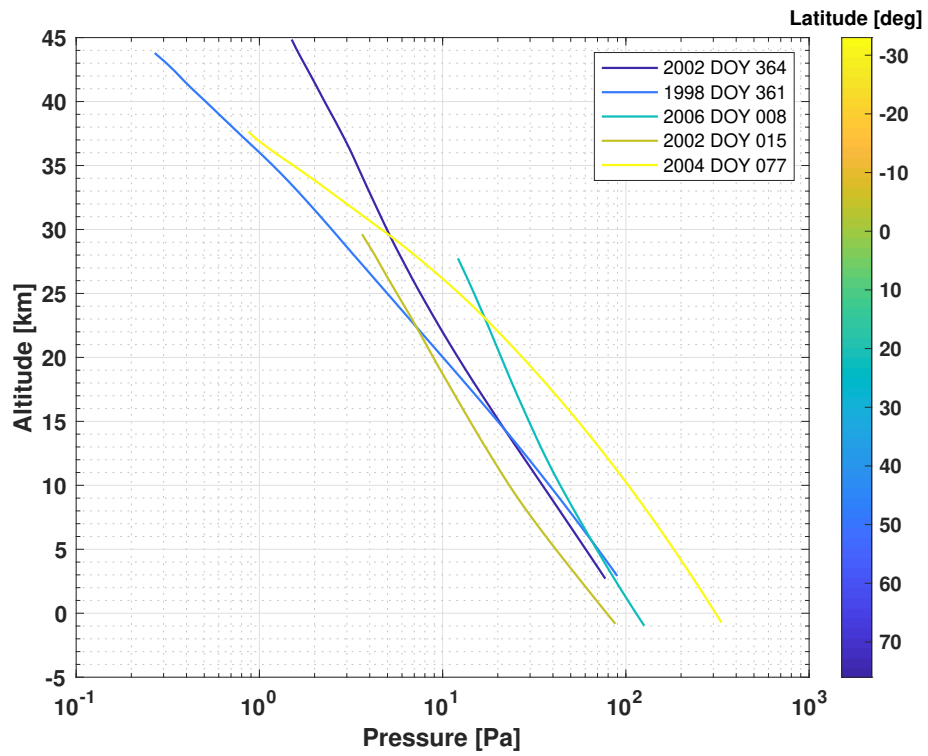


Figure 5.15: Pressure profiles of the MGS occultations.

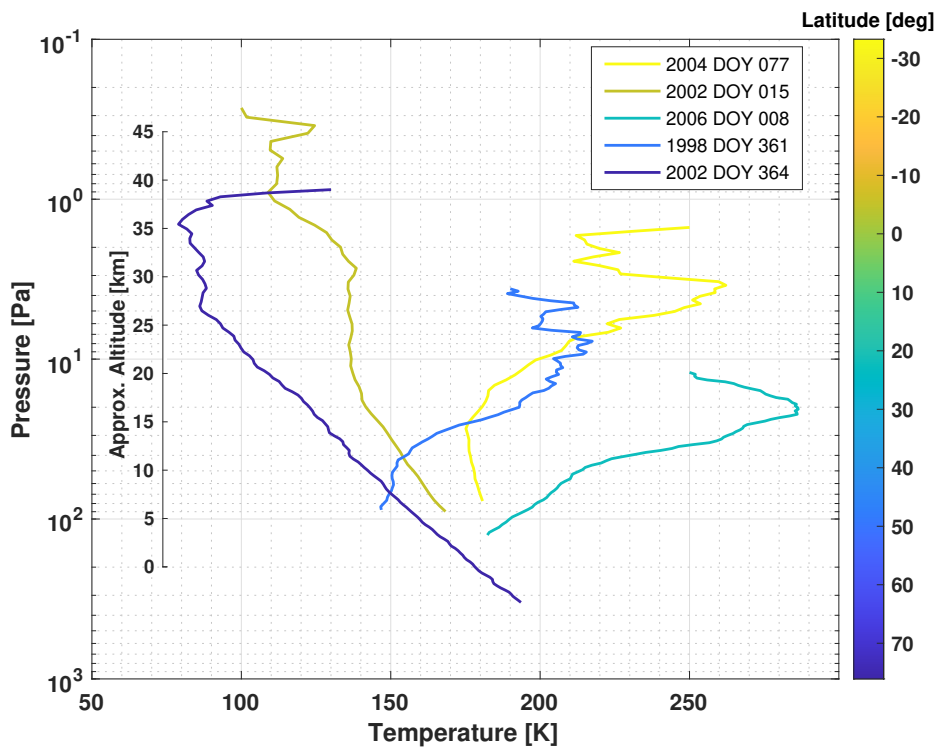


Figure 5.16: Temperature-pressure profiles of the MGS occultations.

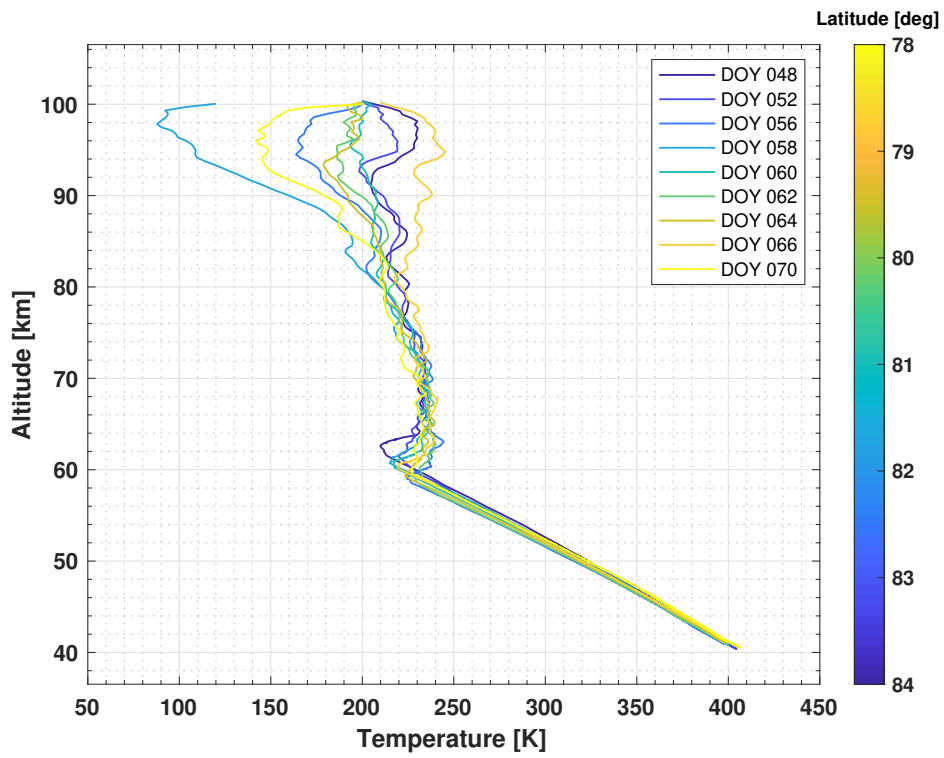


Figure 5.17: Temperature profiles for the **VEX** ingress occultations.

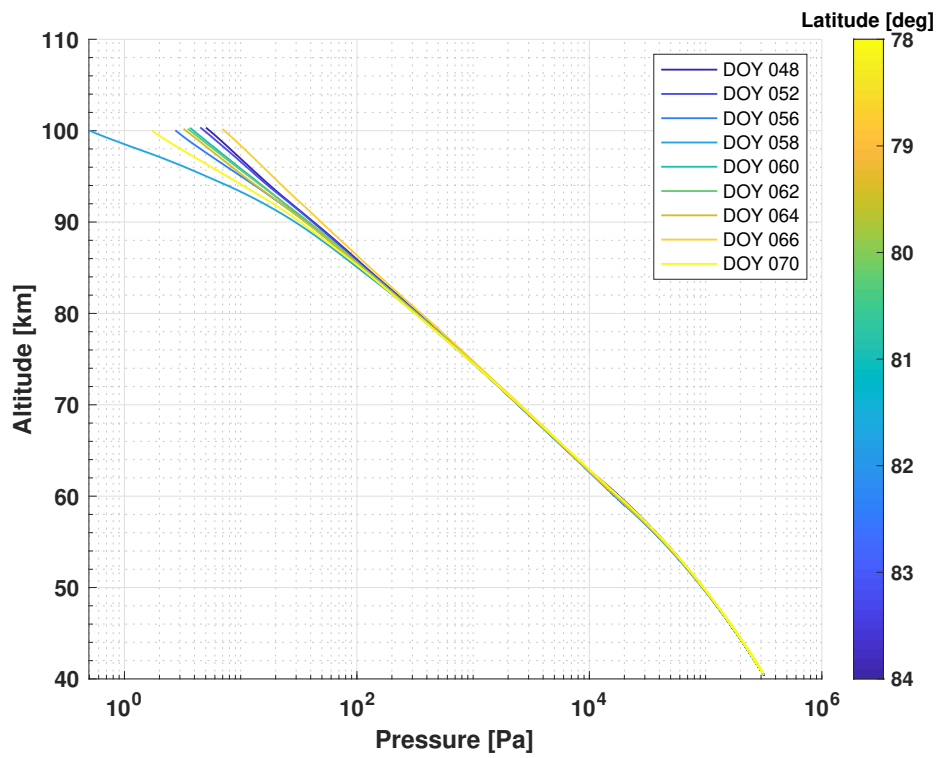


Figure 5.18: Pressure profiles of the **VEX** ingress occultations.

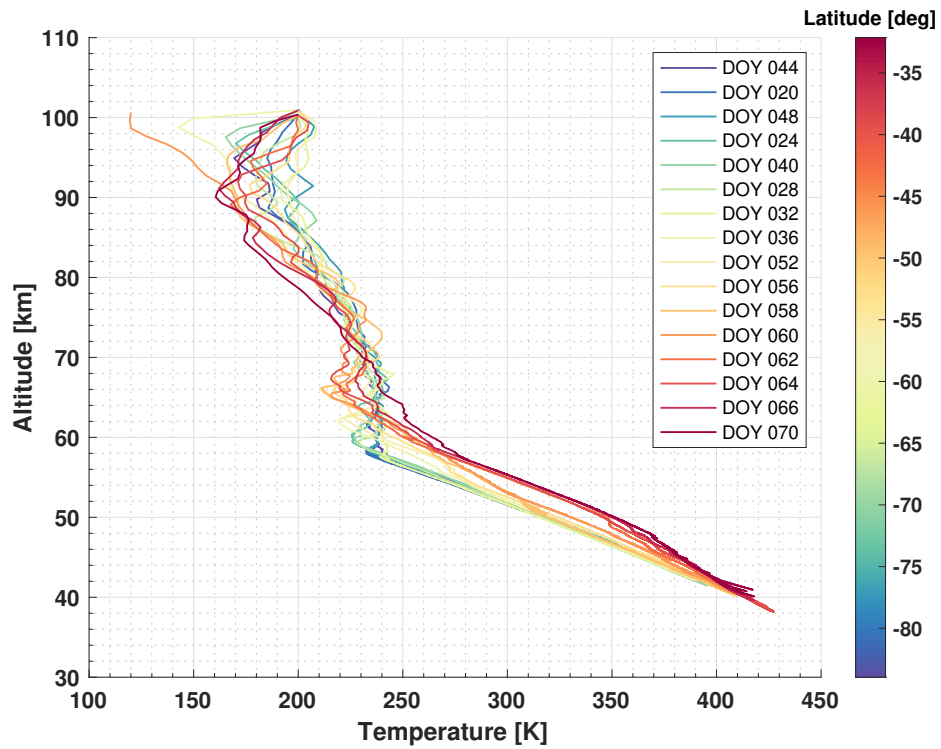


Figure 5.19: Temperature profiles of the **VEX** egress occultations.

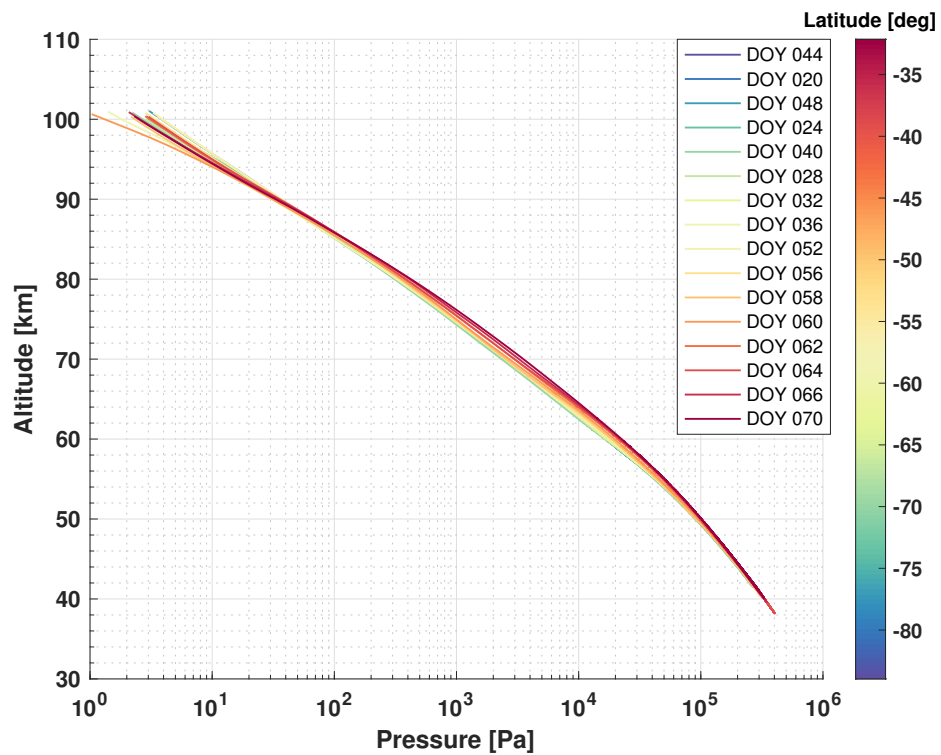


Figure 5.20: Pressure profiles of the **VEX** egress occultations.

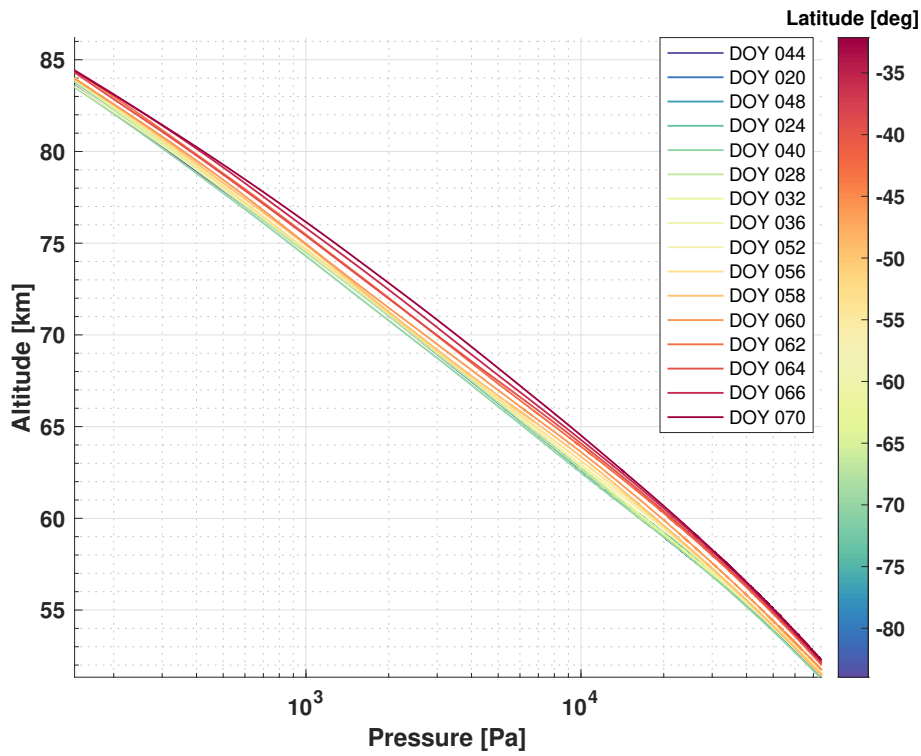


Figure 5.21: Closer look on Figure 5.20.

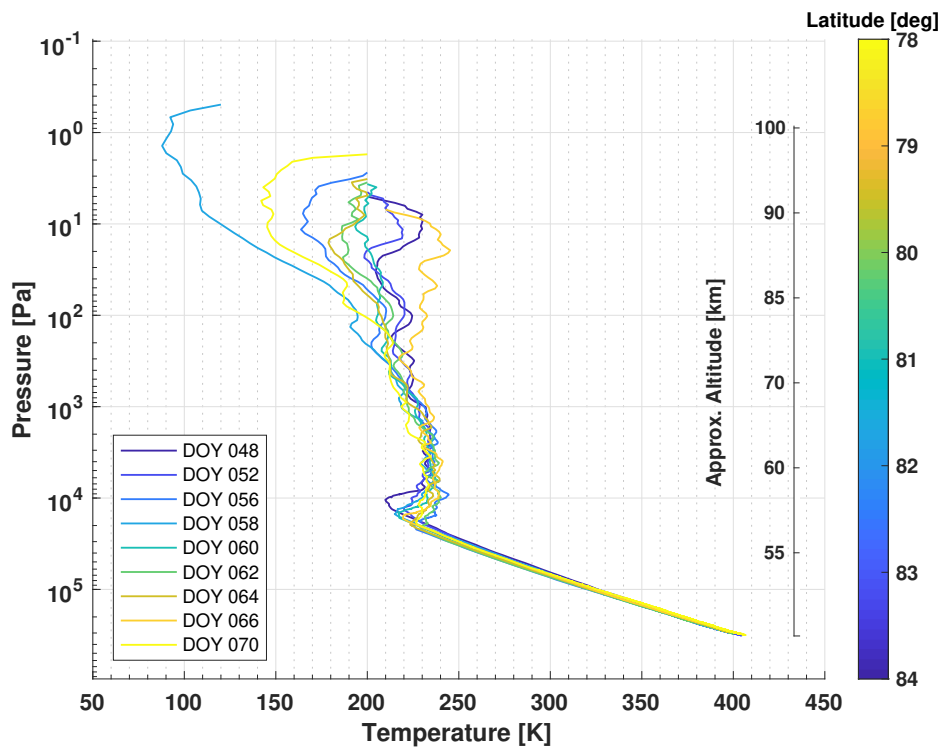
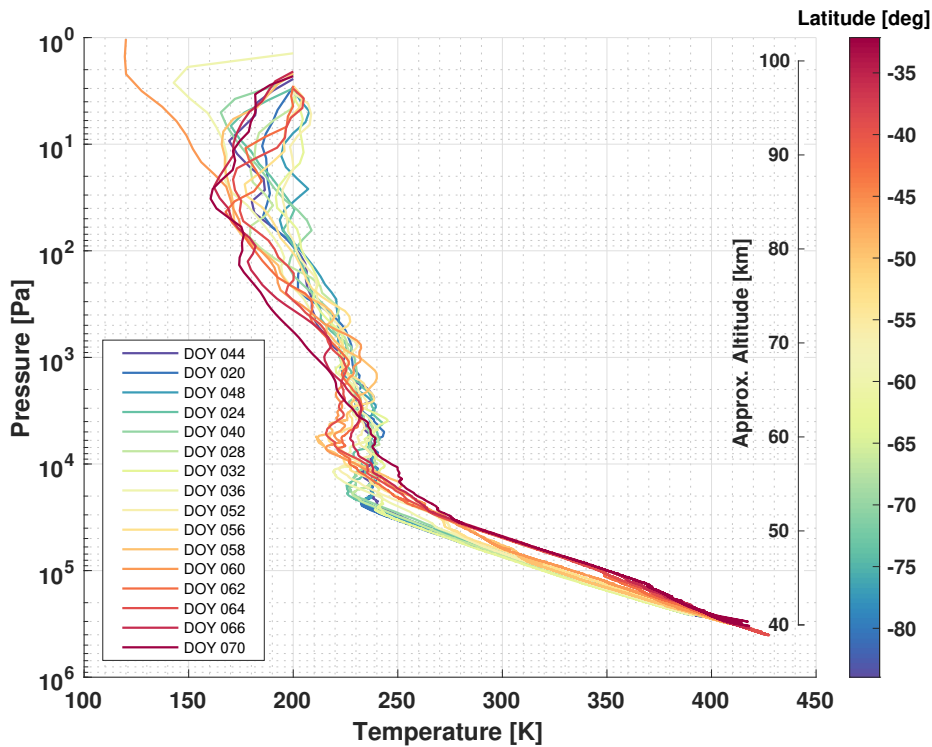


Figure 5.22: Temperature-pressure profiles of the VEX ingress occultations.



**Figure 5.23:** Temperature-pressure profiles of the **VEX** egress occultations.

From the general point of view, the results of MGS shows that on Mars the temperature and pressure strongly depend on the mutual position between the Sun and Mars, the day of the year, the local solar time and obviously the latitude. In fact, depending on the occultation analyzed, the temperature profile can be characterized by a completely different trend and values along the profile itself. Mars shows temperature which both increases and decreases with the altitude, depending on the analyzed occultation. On the other hand, this does not happen for Venus, which through the years always showed similar trend in the temperature and pressure profiles (the results of the VEX occultations from 2006, analyzed by Tellmann, Pätzold etc. showed the same trend observed in these occultations of 2014, see [21] - [17]). In particular, the temperature of Venus after the tropopause (which is the inversion layer after which the temperature decreases linearly, about 50 km altitude) always increases when the altitude decreases. This could be related to different factors: for example, one of these are the zonal winds present in the atmosphere of Venus, which are characterized by extremely high speeds. These

generate a high and fast mixing of the atmosphere so that the effects of the mutual position between Venus and the Sun, the Local Solar Time and the day of the year do not affect the general trend of the profiles in the neutral atmosphere. In addition, another factor is the high thermal inertia of Venus, caused by the greenhouse effect of its thick clouds. As a consequence, this effect does not permit to the heat present in the low-middle altitudes regions to escape. The temperatures and pressures found from Venus Express confirm the extreme and hostile environment on Venus, with its atmosphere characterized by temperature as high as 430 K and pressure of 4 bar at 38 km altitude. These values would continue to increase as the altitude decreases, reaching values at the surface of over 700 K and pressures of nearly 92-93 bar. However, radio occultation experiments are not capable to study the dense and thick atmosphere of Venus so close to its surface, due to the level of super refraction described above. The Mars' occultations analyzed, instead, show a completely different environment, with temperatures in the average of 100-300 K and also low pressures 0.001-0.003 bar near the surface.

Studying the details of these results, a dependence of the atmosphere of Venus on the latitude has been found. In particular, Figure 5.19 and Figure 5.21 highlight that the temperatures and pressures at the equator (red colors) are higher with respect to the ones at the poles (blue colors), with differences in the order of 30 K at 54 km altitude. In addition, the profiles at the equator are in night condition, while the ones at high latitudes are in day condition. This highlight that the day/night condition does not affect significantly the temperature profile at the equator, which are always higher with respect to the polar regions (even if these are in day time). Also this aspect is linked to the two main effects mentioned before: the first one is the presence of *zonal winds* in the mid latitudes at medium-low altitudes, which are responsible for the atmosphere superrotation of Venus. The atmosphere of Venus is well-known for being much faster than the rotation of the planet itself (the atmosphere takes 3-5 Earth's days to complete a Venus rotation, while one Venusian day is 243 Earth days) and this superrotation generates a strong and efficient heat transfer in the mid-latitudes, all over the planet. The second aspect is the *high thermal inertia* of Venus, due to its greenhouse effect of its thick clouds which traps the heat. So in the end, these are the reason why the points at the equator in night condition are still characterized by higher temperature and pressures. This effect is more visible in the VEX egress cases, because they covered

a wider range of latitudes than the ingress cases, which were limited to the north polar region.

### 5.3 Venus scientific results

Within this investigation, the VEX egress cases have been considered mainly, since they cover a wider range of latitudes and permit to highlight possible patterns in the Venus' atmosphere. As discussed in the previous section, one of the first results observed is that the temperatures in the Venus' atmosphere are characterized by a latitude dependence, as on Earth. So, at the equator the temperature is higher with respect to at the poles, and this does not depend on day/night condition, as can be seen from Figure [5.19](#).

In addition the Venus' tropopause has been analyzed, in particular for each occultation the tropopause temperature and the tropopause altitude has been recorded, see Figures [5.25](#) - [5.26](#). The tropopause of Venus has been studied with a first order analysis. In particular the tropopause level can be defined as the altitude at which the temperature lapse rate shows a significant decrease. In practice, it could be detected by studying the static stability of the temperature along the vertical profile. However for time constraints, a first order analysis has been conducted to detect the tropopause by visually looking at the profiles, in order to detect the position of this inversion layer, clearly visible in most of the Venus occultations, see Figure [5.24](#). The trend observed within these analysis is similar to the one presented by Tellmann (2009) [\[21\]](#), see Figures [5.25](#) - [5.26](#). In particular a latitude dependence can be found, with the region at the poles which is characterized by fluctuations in the temperature and altitude, probably linked to the polar vortex structures of Venus.

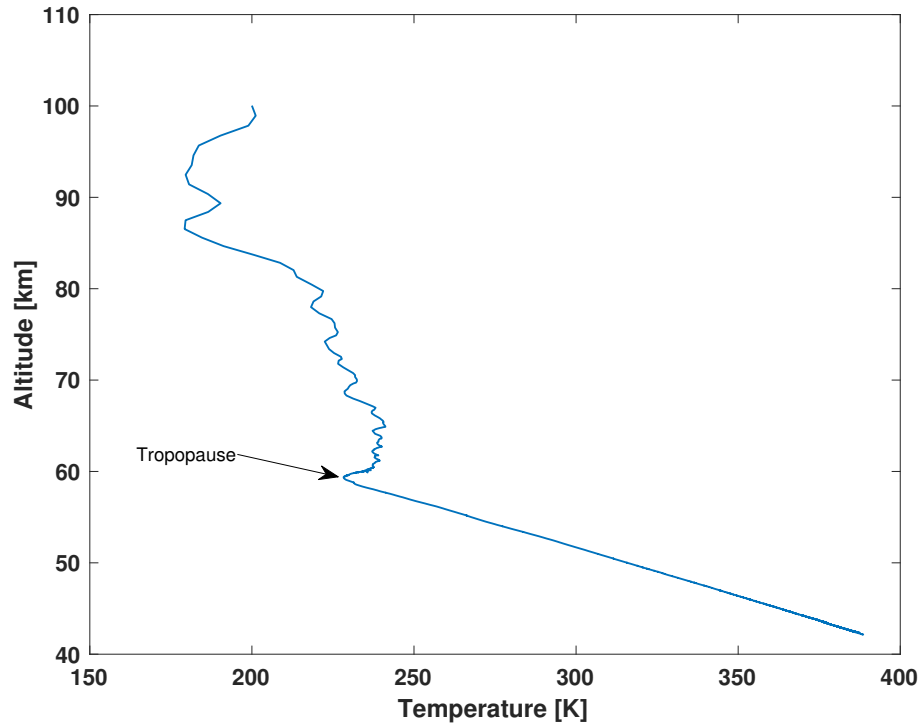


**Figure 5.24:** Tropopause of Venus (example to detect it graphically).

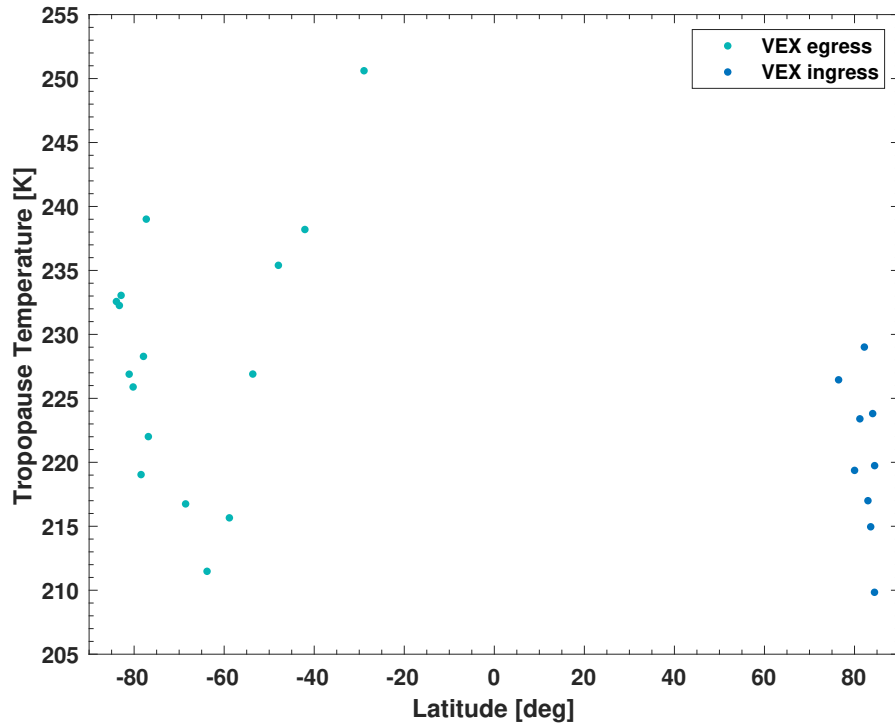


Figure 5.25: Venus' tropopause temperature vs latitude.

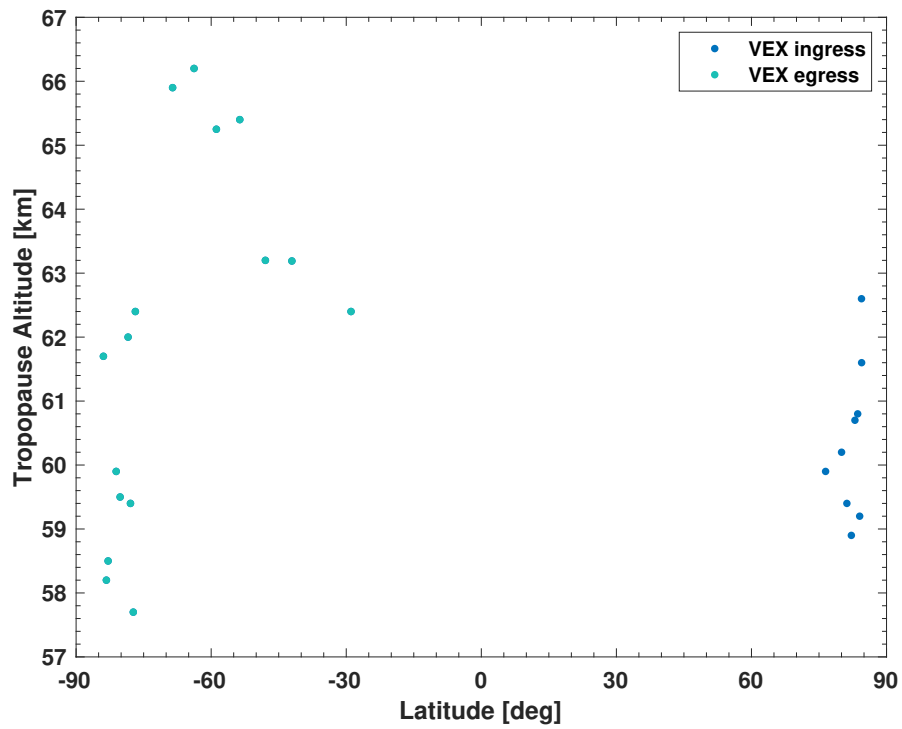
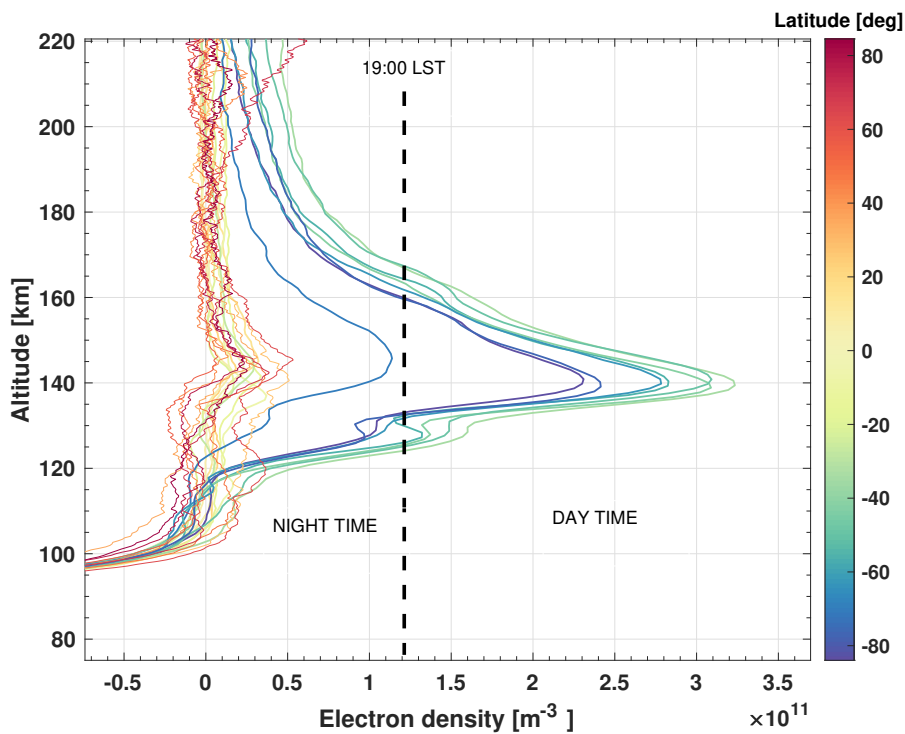


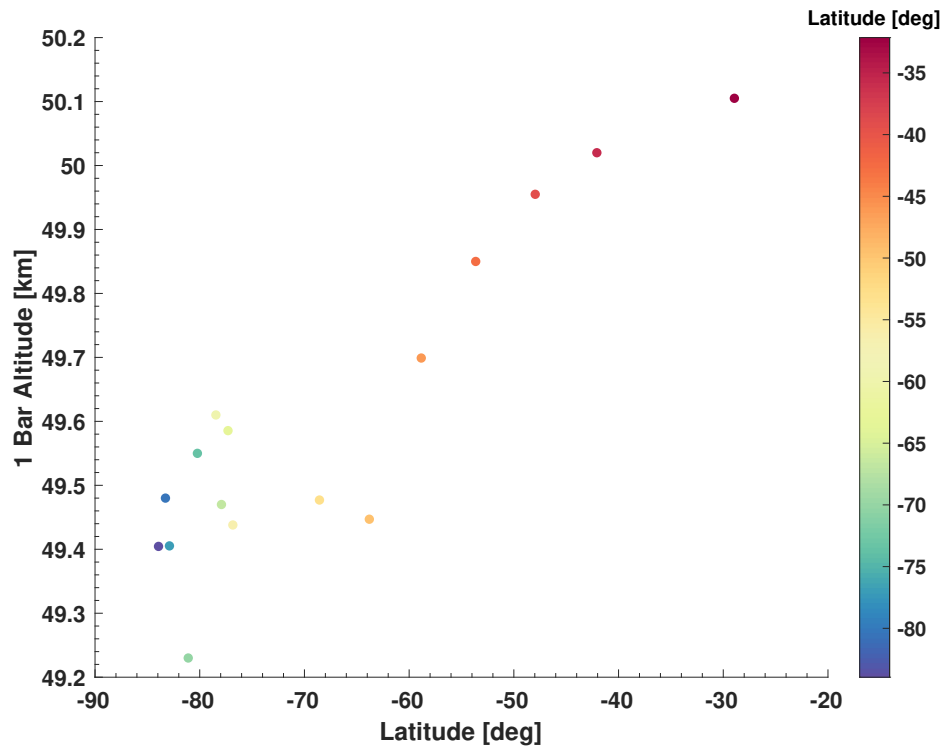
Figure 5.26: Venus' tropopause altitude vs latitude.

In addition a study has been conducted to analyze the behavior of the ionosphere altitude. From Figure 5.27 is possible to see that the ionosphere is confined between 137 and 145 km. An interesting feature, which has been found, is that there is a link between the electron density and the Local Solar Time. In fact, the high peaks of the electron density in the Venus' ionosphere have been found at high latitudes in the South pole, which were characterized by a local day time. On the other hand, the equator occultations were characterized by night local time, so there was not a direct sunlight able to ionize the upper atmosphere, as a consequence the electron density has been found lower. To conclude, this is valid also with respect to the occultations at the North pole which were characterized by a night time condition, and as a results the electron density is lower than the South polar regions in day time.

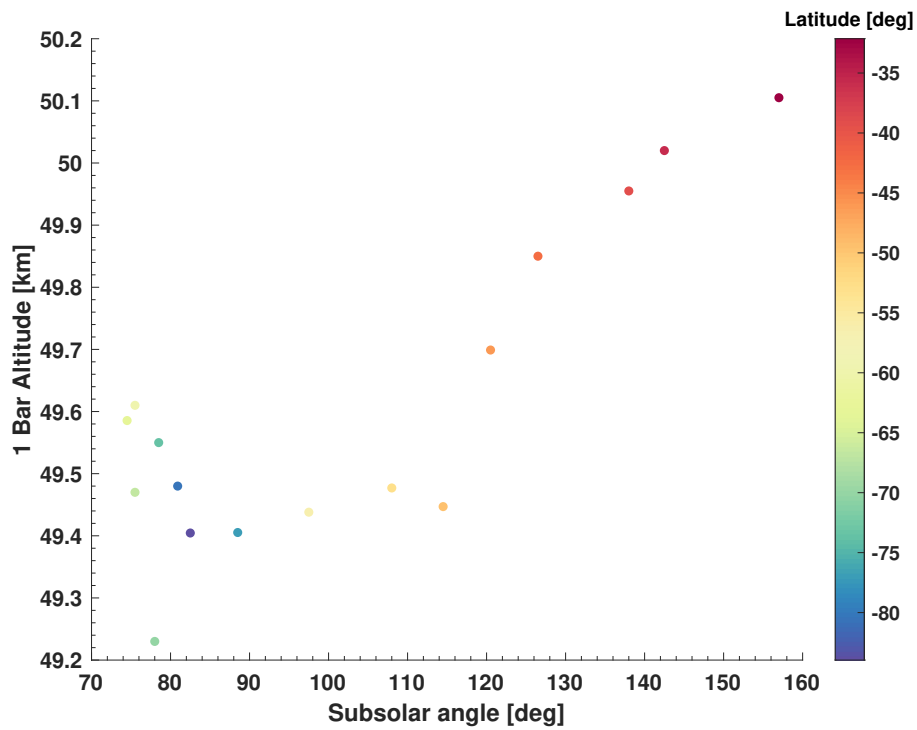


**Figure 5.27:** Electron density vs altitude, latitude and local solar time (LST).

To conclude, a study has been conducted regarding the altitude at which the pressure reaches the 1-bar level and the results are presented in Figure 5.28.



(a)



(b)

**Figure 5.28:** Variation of the 1 bar altitude with respect to:  
a) Latitude ; b) Subsolar angle.

The last result of this thesis has been found in the 1-bar altitude. In particular, the first plot of Figure 5.28a, shows the dependence of the 1 bar altitude with respect to the latitude. As expected, at low latitudes near the equator, the temperature is higher, so that the pressure is higher and as a consequence the 1-bar surface is found at a higher altitude. Then, the same plot has been made with respect to the subsolar angle, which takes into account the day or night condition at the occultation point, see Figure 5.28b.

To be precise, the subsolar angle is defined so that a low value means *day condition*, while angles around 150 - 180 degrees for example are in the *night condition*. The subsolar plot shows high latitudes, near the poles, which are in day time condition, while the points at low latitudes (near the equator) are in the night time condition. So, the plot tells that the points at the equator in night time are characterized by higher 1-bar altitudes, with respect to the points at higher latitudes in day time. The reasons behind this phenomena, as described before, are due to the *zonal winds* present at Venus, and to the Venus' *high thermal inertia* caused by the greenhouse effect of its thick clouds, so that they are more influent than the day or night condition. The zonal winds are winds characterized at extremely high speeds (140-150 m/s), especially near the equator, while these speeds decrease steadily to zero at the poles [10] - [14]. In particular these zonal winds generate the so called atmospheric superrotation of Venus, which allows the atmosphere to complete one rotation around Venus in 3-4 Earth days (note that one day at Venus takes 243 Earth days, so one Venus day is longer than one Venus year 225 Earth days). The atmospheric superrotation, particularly concentrated at the equator, as well as the high thermal inertia of Venus, explain the feature discovered in this study: during the day the equator is the region which heats up the most thanks to the direct sunlight of the Sun and due to the fact that Venus axis of tilt is 177.3 degrees (so Venus does not experience seasons) and this explains the first consideration, so the reason why it is expected that at the equator the 1-bar surface is higher. In addition, the warming of Venus is caused by the sum of the equator heating, the greenhouse effect and the zonal heat transfer (Westward direction mainly, the meridional heat transfer N-S or S-N is low or null), and due to the superrotation the heat is transferred to the night region in a very fast and efficient way, but also the heat in the night region is trapped by the greenhouse effect: the combination of these effects explain why at the equator, even if at night, the 1-bar

surface is higher with respect to the day time at the polar regions.

To conclude, it is interesting to point out, that this day/night effect does not affect the neutral atmosphere of Venus, but it affects the ionosphere, since a dependence of the electron density to the day/night condition has been found. This because the thick clouds of Venus, responsible for its high thermal inertia and the greenhouse effect, as well as the zonal winds, are present at altitudes below the Venus' ionosphere. So the upper atmosphere is influenced by the day/night condition, while the neutral atmosphere is not.





## Chapter 6

# Conclusions and Discussion

This thesis demonstrates mainly the strong differences instead of similarities between Venus and Mars atmospheres. In particular, from the scientific point of view it has been found, as expected, that the two atmospheres are completely different and the dense and thick Venus' atmosphere is responsible for the extremely high temperatures, pressures, bending angles and refractivity. In addition, from the general point of view Venus shows always the same general trend in the temperature and pressures (a trend which always sees the pressure and temperature increase with the decreasing altitude), while on Mars different behaviors can be found throughout different months.

Furthermore, one of the main challenges from the engineering point of view, has been related to the calibration process of the frequency residuals: in one-way link the stability of the Ultra Stable Oscillator is crucial, as well as the errors of the estimated trajectory should be as low as possible for the success of the occultation experiment. Within this work, it has been pointed out a strong difference in the frequency residuals of Venus Express in the Ingress occultations with respect to the Egress cases, which is linked to a lower stability of the USO and also to errors in the estimated trajectory given by the navigation team as the spacecraft approaches the planet, which is due to the effect of the dynamics of the planets on the spacecraft. The calibration process has been straightforward for Mars, which showed extremely good frequency residuals from the beginning, while it has been more difficult for Venus due to the reasons related to the USO and the trajectory. Moreover, within this thesis it has been shown that the differences between the

relativistic solutions and the non-relativistic ones are negligible, both for Venus and Mars.

In addition, within this thesis, a set of occultation data from Venus Express mission (2014), recorded by the Deep Space Network of NASA and never studied before, have been analyzed. Interesting results about the Venus' atmosphere and its dependence to the latitude, to the zonal winds and day/night condition have been carried out. In particular, first of all a dependence of the electron density to the day/night condition has been discovered, showing that at high altitudes between 137 - 145 km the day/night condition influence the ionosphere of the planet. In fact, for the ionosphere, the day/night condition is more influent than the latitude position of the occultation point, and the plots clearly shows that the occultation points which were in day condition (which means ionization of the ionosphere due to the Sun radiation), even if at high latitudes, experienced higher electron density than the ones near the equator and the poles in the night. However, it has been interesting to notice that this trend is not true at lower altitudes, where the 1-bar altitude at the equator is not influenced by the night/day condition as the ionosphere. This is due to the atmospheric superrotation caused by zonal winds, which is present in the medium-lower atmosphere (50-70 km altitude) and by the high thermal inertia of Venus, due to its thick clouds in medium-low altitudes and responsible for the high greenhouse effect on the planet. In practice, the mid-latitude zonal winds transfer the heat in a fast and efficient way, and at the same time the greenhouse effect traps the heat, so that the equatorial regions at night time do not suffer strong differences with respect to the day time ones. As a consequence, the night points analyzed at the equator are still characterized by higher 1-bar altitudes than the day time polar points: in fact these zonal winds are not present at the poles, so that the meridional heat transfer is low, and the amount of heat found at the poles at day time is lower than the heat at the equator at night time.

To reach these goals, within this thesis all the steps needed to understand and study a radio occultation experiment have been covered, both from the engineering and scientific point of view. Within this work an atmosphere algorithm in MATLAB environment has been developed and validated. In addition, secondary algorithms which computed the Earth's troposphere and ionosphere corrections

have been developed, too.

Furthermore, it is important to notice that this thesis and the algorithms developed are mainly focused on one-way radio link experiment, single frequency experiment, with a valid spherical symmetry atmosphere assumption at the target planet. Please note also that within this work the plasma noise has not been considered (the single frequency experiments of the available data did not permit to calibrate it), in addition the estimated trajectory found for VEX was not really accurate. To increase the accuracy of this work a correction on the estimated trajectory should be made. Moreover, within this investigation the accuracies and uncertainties of the results have not been computed, an aspect which should be analyzed too for deeper studies.

To conclude, there are still many unanswered scientific questions about Venus, that is why Venus could be selected as one of the main target for future space missions. In particular, *NASA Discovery Program* has selected two Venus space missions proposals, *VERITAS* from *NASA-Jet Propulsion Laboratory* and *DAVINCI+* from *NASA Goddard Space Flight Center*. The radio occultation experiments are extremely useful to probe the atmosphere of the planets, however in case of dense and thick atmospheres, as the one of Venus, this kind of experiment is not capable to study deeply the atmosphere until the surface of the planet, as it is for Mars, so different techniques as radars instruments or in-situ missions should be adopted to increase our knowledge on the planet.



# Bibliography

- [1] S. W. Asmar, J. W. Armstrong, L. Iess, and P. Tortora. Spacecraft Doppler tracking: Noise budget and accuracy achievable in precision radio science observations. *Radio Science*, 40(2):1–9, 2005.
- [2] S. W. Asmar and N. A. Renzetti. The Deep Space Network as an Instrument for Radio Science Research. Technical Report 2, NASA-Jet Propulsion Laboratory, Pasadena, CA 91107, 1993.
- [3] Dustin R. Buccino, Jill A. Seubert, Sami W. Asmar, and Ryan S. Park. Optical ranging measurement with a Lunar Orbiter: Limitations and potential. *Journal of Spacecraft and Rockets*, 53(3):457–463, 2016.
- [4] Deep Space Network (DSN). TRK-2-23 Media Calibration Interface. Technical report, NASA - JPL, 2008.
- [5] Von R. Eshleman. The radio occultation method for the study of planetary atmospheres. *Planetary and Space Science*, 21(9):1521–1531, 1973.
- [6] G. Fjeldbo and V. R. Eshleman. Atmosphere of Venus as Studied with the Mariner 5 Dual Radio-Frequency Occultation Experiment. *Radio Science*, 4(10):879–897, 1969.
- [7] G. Fjeldbo, Arvydas J. Kliore, and Von R. Eshleman. The Neutral Atmosphere of Venus as Studied with the Mariner V Radio Occultation Experiments. *The Astronomical journal*, 225(2):1–21, 1971.
- [8] B. Häusler, M. Pätzold, G. L. Tyler, R. A. Simpson, M. K. Bird, V. Dehant, J. P. Barriot, W. Eidel, R. Mattei, S. Remus, J. Selle, S. Tellmann, and T. Imamura. Radio science investigations by VeRa onboard the Venus Express spacecraft. *Planetary and Space Science*, 54(13-14):1315–1335, 2006.

## BIBLIOGRAPHY

---

- [9] D. P. Hinson, R. A. Simpson, J. D. Twicken, G. L. Tyler, and F. M. Flasar. Initial results from radio occultation measurements with Mars Global Surveyor. *Journal of Geophysical Research E: Planets*, 104(E11):26997–27012, 1999.
- [10] R. Hueso, J. Peralta, and A. Sánchez-Lavega. Assessing the long-term variability of Venus winds at cloud level from VIRTIS-Venus Express. *Icarus*, 217(2):585–598, 2012.
- [11] Arvydas Kliore, Dan L. Cain, Gerald S. Levy, Von R. Eshleman, Gunnar Fjeldbo, and Frank D. Drake. Occultation Experiment: Results of the First Direct Measurement of Mars’s Atmosphere and Ionosphere. *Science*, 149(3689):1243–1248, sep 1965.
- [12] A. S. Konopliv, W. B. Banerdt, and W. L. Sjogren. Venus Gravity: 180th Degree and Order Model. *Icarus*, 139(1):3–18, 1999.
- [13] G. Mariotti and P. Tortora. Experimental validation of a dual uplink multi-frequency dispersive noise calibration scheme for Deep Space tracking. *Radio Science*, 48(2):111–117, mar 2013.
- [14] Matthew Newman, Gerald Schubert, Arvydas J. Kliore, and Indu R. Patel. Zonal Winds in the Middle Atmosphere of Venus From Pioneer Venus Radio Occultation Data., 1984.
- [15] M. Parisi. *La misura delle deformazioni mareali di Ganimede*. Master thesis, Sapienza Università di Roma, 2013.
- [16] M. Parisi. Gravity and geodesy of the Jovian system bodies with the Juno and JUICE missions, 2014.
- [17] M. Pätzold, B. Häusler, M. K. Bird, S. Tellmann, R. Mattei, S. W. Asmar, V. Dehant, W. Eidel, T. Imamura, R. A. Simpson, and G. L. Tyler. The structure of Venus’ middle atmosphere and ionosphere. *Nature*, 450(7170):657–660, 2007.
- [18] R. A. Phinney and D. L. Anderson. On the radio occultation method for studying planetary atmospheres. *Journal of Geophysical Research*, 73(5):1819–1827, 1968.

- [19] Phillip H. Phipps and Paul Withers. Radio occultations of the Io plasma torus by Juno are feasible. *Journal of Geophysical Research: Space Physics*, 122(2):1731–1750, 2017.
- [20] H. Svedhem, D. V. Titov, D. McCoy, J. P. Lebreton, S. Barabash, J. L. Bertaux, P. Drossart, V. Formisano, B. Häusler, O. Korablev, W. J. Markiewicz, D. Nevejans, M. Pätzold, G. Piccioni, T. L. Zhang, F. W. Taylor, E. Lellouch, D. Koschny, O. Witasse, H. Eggel, M. Warhaut, A. Accomazzo, J. Rodriguez-Canabal, J. Fabrega, T. Schirmann, A. Clochet, and M. Coradini. Venus Express-The first European mission to Venus. *Planetary and Space Science*, 55(12):1636–1652, 2007.
- [21] Silvia Tellmann, Martin Pätzold, Bernd Häusler, Michael K. Bird, and G. Leonard Tyler. Structure of the Venus neutral atmosphere as observed by the Radio Science experiment VeRa on Venus Express. *Journal of Geophysical Research E: Planets*, 114(4):1–19, 2009.
- [22] D. V. Titov, H. Svedhem, D. Koschny, R. Hoofs, S. Barabash, J. L. Bertaux, P. Drossart, V. Formisano, B. Häusler, O. Korablev, W. J. Markiewicz, D. Nevejans, M. Pätzold, G. Piccioni, T. L. Zhang, D. Merritt, O. Witasse, J. Zender, A. Accomazzo, M. Sweeney, D. Trillard, M. Janvier, and A. Clochet. Venus Express science planning. *Planetary and Space Science*, 54(13-14):1279–1297, 2006.
- [23] Paul Withers. Prediction of uncertainties in atmospheric properties measured by radio occultation experiments. *Advances in Space Research*, 46(1):58–73, 2010.
- [24] Paul Withers, L. Moore, K. Cahoy, and I. Beerer. How to process radio occultation data: 1. From time series of frequency residuals to vertical profiles of atmospheric and ionospheric properties. *Planetary and Space Science*, 101:77–88, oct 2014.
- [25] Paul Withers, M. C. Towner, B. Hathi, and J. C. Zarnecki. Analysis of entry accelerometer data: A case study of Mars Pathfinder. *Planetary and Space Science*, 51(9-10):541–561, 2003.